Novel Transport Behavior in Two-dimensional Semiconducting and Superconducting Transitional Metal Dichalcogenides

by

Yafang Yang

B.S., University of Science and Technology of China (2012)

Submitted to the Department of Physics
in partial fulfillment of the requirements for the degree of

Doctor of Philosophy

at the

MASSACHUSETTS INSTITUTE OF TECHNOLOGY

June 2019

Signature redacted

Author .....
Department of Physics
May 5th, 2019

Signature redacted

Certified by .....
Pablo Jarillo-Herrero
Cecil and Ida Green Professor of Physics
Thesis Supervisor

Signature redacted

Accepted by .....
Nergis Mavalvala
Associate Department Head

Novel Transport Behavior in Two-dimensional Semiconducting and Superconducting Transitional Metal Dichalcogenides

by

Yafang Yang

Submitted to the Department of Physics
on May 5th, 2019, in partial fulfillment of the
requirements for the degree of
Doctor of Philosophy

Abstract

Atomically layered transitional metal dichalcogenides (TMDs) manifest many fascinating properties such as atomic-scale thickness, favorable mechanical, electronic and optoelectronic properties and strong spin-orbit coupling. In terms of electronic properties, the TMDs range from insulating or semiconducting to metallic or semi-metallic. Some of them also exhibit exotic electronic phases such as charge density waves and superconductivity. Recent advances in nano-materials characterization and device fabrication, in particular, fabrication of high quality van der Waals heterostructures, have boosted studies on two-dimensional layers of thin TMDs for purpose of both fundamental research and industrial applications.

In this thesis, I present a series of experiments investigating electronic and optoelectronic properties of semiconducting TMDs MoS_2 and WSe_2. I also demonstrate technical advances in fabrication of van der Waals heterostructures, which enables high-quality encapsulated thin TMDs devices with ionic liquid introduced as electrolyte. I further show that phase transitions in superconducting TMDs such as 2H-TaS_2 can be greatly impacted by dimensionality reduction. A substantial enhancement of superconducting T_c and a suppression of the CDW transition are observed in 2H-TaS_2 in the 2D limit. At last, I present a machine learning algorithm to realize pixel-wise classification on laboratory acquired images of various 2D materials, which might open up new opportunities for full automation of nano-material search and device fabrication.

Thesis Supervisor: Pablo Jarillo-Herrero
Title: Cecil and Ida Green Professor of Physics

Acknowledgments

The completion of this thesis would not have been possible by the ever-present guidance and help of my family, friends and colleagues. I would like to thank my advisor, Pablo Jarillo-Herrero, for providing me the great opportunity to work on the exciting field with a group of extraordinary people, as well as his consistent guidance and support, on both my research, course work and life. I also would like to thank my thesis committee for their stewardship of my thesis, and Ray Ashoori, my academic adviser, for his consistent positive support.

In addition, I would like thank the whole group for all of their insight and assistance. I have had the good fortune to work closely with a number of brilliant colleagues and post-doctoral scholars, Hugh, Britt, Efren, Sanfeng and Valla, who have always been excellent partners on projects through my PhD life. All of them shaped me and my research methodology in one way or another, and played an indispensable role in my life. Here I would like to express my special thankfulness to Hugh, who is always so passionate, patient and caring. He guided me, motivated me through the early years of research, taught me all sorts of experimental skills and spent hours with me inside the cleanroom.

I also would like to thank Javier, for his passion towards research and almost 'contagious' joyfulness, as well as Qiong, who means more than a friend or a colleague to me, for all the helpful discussions and advices. They made me feel at home even though I am thousands of miles away from my hometown. The warmth also comes from all the Chinese and dine-out friends in building 13, including Yuan, Yaqing, Cosmi, Suyang, Linda, Alfred, Xi Ling, Jiarui, Xirui, Zhiren, Edbert and many other friends from Jing Kong's group upstairs. Besides, the great atmosphere within the group is not possible without so many great members and former members of the group, including Dani, Joel, Jason, Dahlia, Melis, David, Kenji, Landry, Hadar and a few excellent UROPs, Kamphol, Yu-An Chen, Andres and Francisco. We had so many valuable time and precious moments together. I also received a lot of selfless help on experiments from them, especially from Yuan and Jason, when we are at

Maglab at Florida, and I learnt a lot from them. There are also four people outside my group whom I would like to express great thankfulness to, Shiang and Jonathan, for their helpful discussions, their hard work and their direct contributions to this thesis. I would like to thank Yuxuan (Cosmi), who teamed up with me during course 6.867 machine learning. Without his enthusiasm, the project of deep learning assisted image classification won't proceed that well. I also thank Bingnan who contributed a lot to this project for all the interesting analysis and consultation with us during the early stage of this project.

Here I would like to acknowledge my collaborators at MIT, including Jiarui and Qian from Comin's group for conducting Raman experiments, Takehito from Checkelsky's group for growth of high quality 1T'-WTe_2 and Alfred from Gedik's group. Many supports also come from my collaborators outside MIT, including Siyuan Dai from Basov's group at UCSD, Shengqiang Huang from LeRoy's group at University of Arizona and our hBN provider Kenji Watanabe and Takashi Taniguchi.

At last, I would like to thank my husband, Jun, for his untiring love and support. We developed our friendship over our mutual interest in nano-technology and built a family here at Cambridge. He is a great treasure for my journey to pursuing better self. We named our dog as "Nami", an abbreviation for 'Nano-meter'. I also thank all of my family for their love and support, including my grandparents, my aunts, my uncles and my parents for their love and support from the beginning to the end, and particularly for the space to explore my own path in life.

Contents

List of Figures

List of Tables

Chapter 1

Introduction

Two-dimensional (2D) materials have drawn great attention since the discovery of isolation of single-layer graphene [111] in 2004. Since then, the family of accessible 2D materials has expanded to a whole library with versatile material behaviors - insulators, metals, semi-metals and semiconductors. Among them, many 2D materials manifest novel phase ordering at low temperatures, such as superconductivity, charge-density wave, ferromagnetic and antiferromagnetic order, ferroelectricity and etc. They provide promising platforms to study mesoscopic physics in solids. In addition, their flexible, nearly transparent properties and high mechanical strength also made them promising candidates for a broad variety of potential industrial applications.

This chapter describes a brief introduction of 2D materials and creation of van der Waals heterostructures with a variety of properties.

1.1 2D Materials

Graphene, with its gapless band structure and linear dispersion, provides the opportunity to study Dirac fermions in a solid-state system, which manifests various new physics including novel quantum Hall effect, Klein tunneling, and quantum spin Hall effect [111, 173, 69, 167, 168, 110]. Strong intra-layer covalent bonds lead to high mechanical strength in plane, while weak van der Waals bonds between layers allow

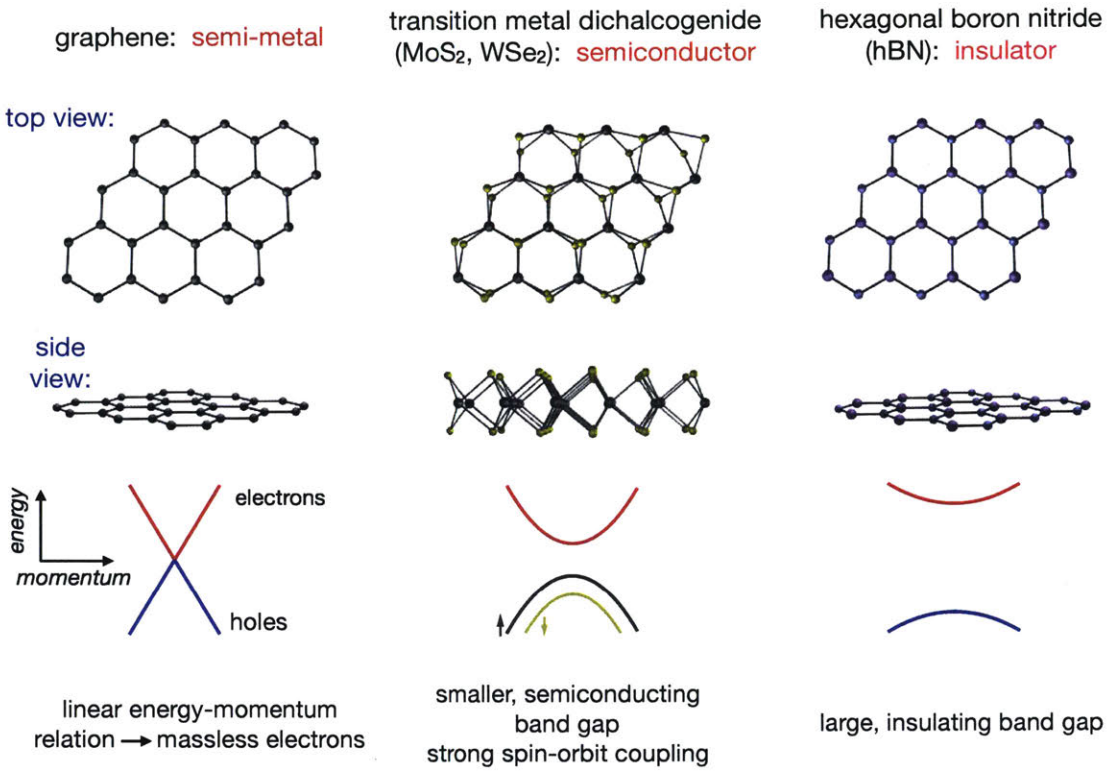

Figure 1-1: Family of 2D materials with diverse electronic and optoelectronic properties. Left: graphene, a semi-metal, can serve as a high-mobility conductor and transparent gate electrode. Middle: Transition metal dichalcogenides are semiconductors with a direct band gap in their monolayer forms. They also posses a valley degeneracy and a spin-split valence band. Right: hexagonal boron nitride is an ultra-flat insulator useful as a gate dielectric with high breakdown voltage.

individual layers to be isolated and studied. However, it is a semi-metal and limited in the scope of electronic device applications that can be realized. The good news is that the study of graphene by mechanical exfoliation has also incubated ever-increasing number of techniques, compatible with existing nanofabrication technology that can be readily applied to other 2D van der Waals materials [51].

Later, more 2D materials with interesting properties are found to be isolatable from their bulk crystals, which greatly complement graphene and broaden the capabilities of 2D materials into a fuller range of electronic devices, as shown in Fig. 1-1. One example is the transition metal dichalcogenides (TMDs) MX_2, where M = Mo, W, Ti, Nb, Ta etc. and X = S, Se, which are known since 1960s [152]. It is comprised

W, Ti, Nb, Ta etc. and X = S, Se, which are known since 1960s [152]. It is comprised of a stack of atomic trilayers composed of a single atomic layer of transitional metal atoms between two layers of chalcogen atoms. These TMDs offer a broad range of electronic properties, from insulating or semiconducting (e.g., Ti, Hf, Zr, Mo, and W dichalcogenides) to metallic or semimetallic (V, Nb, and Ta dichalcogenides).

Among them, MoS_2 and WSe_2 are atomically layered semiconductors [149]. Monolayer MoS_2 and WSe_2 are of particular interest as a large direct-gap semiconductor (e.g. 1.8 eV for MoS_2) [93], as opposed to an indirect band-gap of its bulk and bilayer counterparts, with strong spin-orbit interactions, which result in a spin- and valley-split valence band [41, 152]. These qualities could lead to novel physics such as an unconventional quantum Hall effect, combined spin Hall and valley Hall effects, [158] and new devices such as high-performance, ultra-low power transistors [145] and devices integrating spin- and valley-tronics [146], attracting great attention for potential applications in next-generation nanoelectronic devices. Besides, the direct band gap is in the visible frequency range, making it favorable for optoelectronic applications.

In addition to semiconducting TMDs, another group of metallic 2H-MX_2 (where M = Nb, Ta and X = S, Se) have also attracted considerable attention as novel 2D crystalline superconductors [125]. In these materials, superconductivity (SC) occurs in an environment of pre-existing charge-density wave (CDW) order [106, 71], making them an ideal platform to study many-body ground states and competing phases in the 2D limit. The density of state (DOS) of these metallic TMDs has two main properties: (i) The Fermi level of the undoped material is crossing a band with d-orbital character, implying that the electrons move mostly in the metal layers, and (ii) the DOS at the Fermi level is usually quite high. It is worth to note that electric field induced superconductivity is also observed in ionic liquid gated semiconducting TMDs such as MoS_2 [91, 124].

In addition to graphene and TMDs, hexagonal boron nitride (hBN), with a large band gap of 5.5 eV, is widely used as an ideal substrate and gate dielectric for high quality graphene devices because of its atomically flat surface and nearly defect free single crystal structure [36].

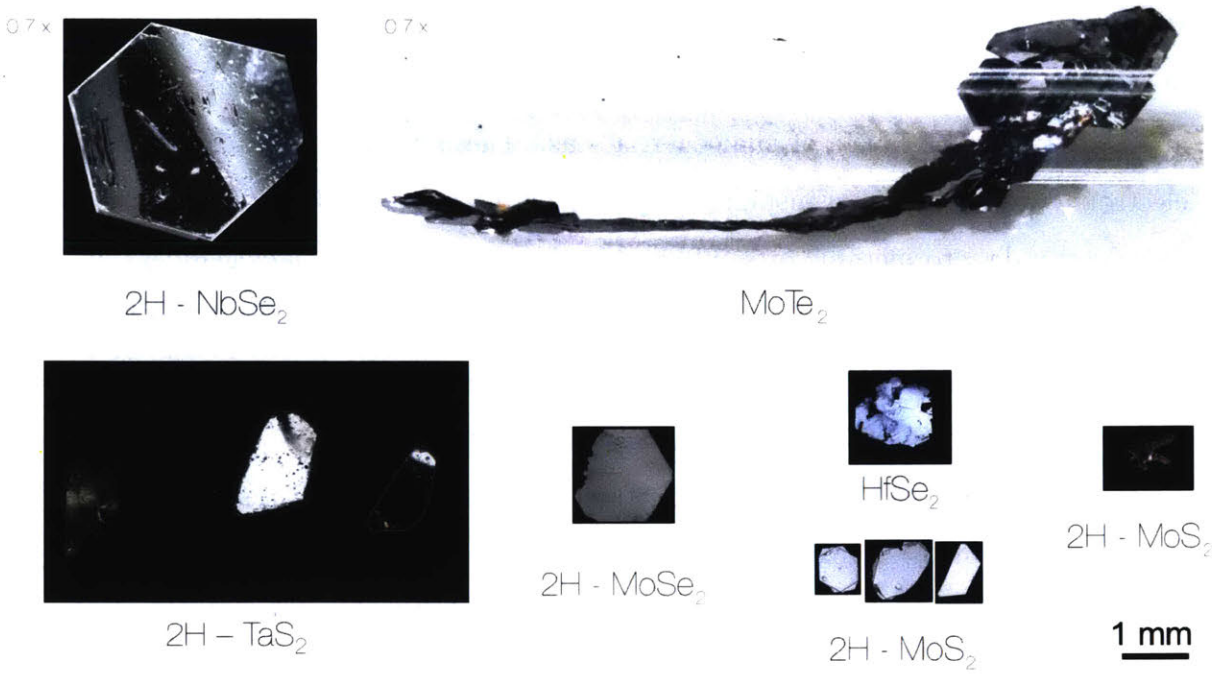

Figure 1-2: Pictures of various laboratory synthesized 2D crystals.

1.2 van der Waals heterostructures

Two-dimensional crystals can be assembled into heterostructures [51, 109], where the 2D materials are held together by van der Waals interactions between adjacent layers. The resulting vertical stack can be seen as an artificial material assembled in a chosen sequence and a chosen stacking order, similar to building with Lego (shown in Fig. 1-3), with blocks of atomically thin materials with atomic precision. Since there are a wide variety of 2D materials that are currently available, the heterostructures that can be created from these 2D materials are substantial. This allows a plethora of combinations that is not possible with any traditional growth method.

When stacking different 2D materials together, several effects need to be considered. First, charge redistribution might occur between the neighboring , or even more distant layers in the stack. Second, neighboring materials can also induce structural changes in each other. Furthermore, such changes can be controlled by adjusting the relative orientation between the individual layers.

1.2.1 Design

Considering the numerous exciting physical phenomena arise from various 2D materials and the even richer variety of physics coming from combining them, the design of heterostructures is worthy of attention.

For example, heterostructures as simple as graphene-on-hBN [36] and, shortly after, encapsulating graphene in between few-layer hBN were shown to significantly boost the electronic quality of graphene. Additionally, encapsulation of graphene between two hBN films also leads to high quality graphene devices in which micrometer-scale ballistic transport persists up to room temperature [98, 134]. The atomically flat surfaces and small lattice mismatch between both crystals facilitate strong adhesion between graphene and hBN, so that the graphene is securely sealed against contaminants derived from nanofabrication. This advantage extends to TMDs such as MoS_2 and WSe_2 [32, 155, 42], which reveals ultra-high low temperature mobility up to $34,000\ cm^2/(V \cdot s)$ for 6-layer MoS_2. It is due to the atomically smooth surface that is relatively free of dangling bonds and charge puddles that are common in SiO_2 substrate. With few-layer or monolayer hBN, it is readily applicable to use it as gate dielectrics and tunnel barriers, which enables capacitance and tunneling measurements. Other heterostructures involving graphene and hBN includes two graphene monolayers separated by a thin hBN spacer to realize Coulomb drag [54], tunneling in graphene/hBN/graphene tunnel transistors [80] and plasmonic devices by sandwiching several graphene layers separated by hBN spacers [172].

In addition, isolation and encapsulation by hBN not only boost the electronic quality of the encapsulated material, but also provide a path towards a perfectly sealed, inert atmosphere. As widely known, graphene is stable in air and decomposition is not a top concern. In general, insulating and semiconducting 2D crystals are more likely to be chemically inert in air. However, for many other metallic TMDs as well as phosphorene, degradation in ambient atmosphere can be a big issue for device fabrication. This is the case for materials like TaS_2 and $NbSe_2$, which is found to degrade and become insulating if device thickness decreases to a few layers.

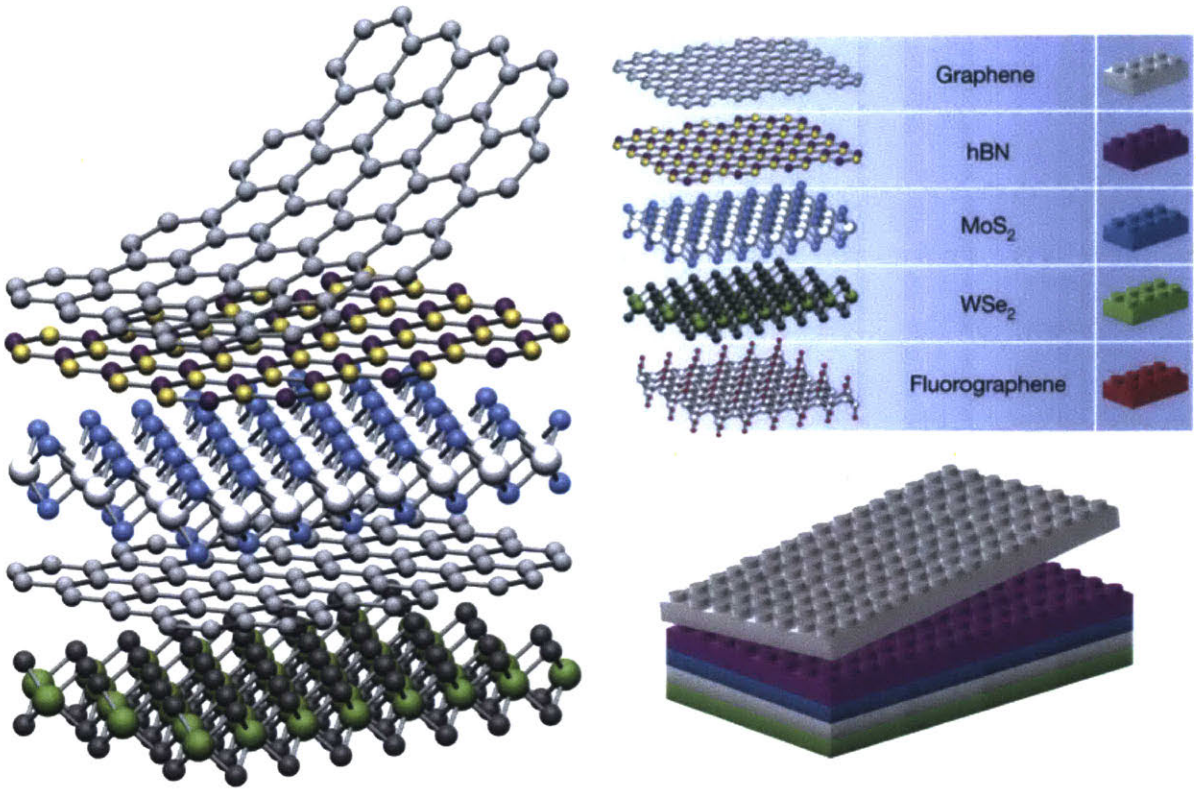

Figure 1-3: Building van der Waals heterostructures from Ref. [51].

The protective cover by hBN is proven to be one of the best methods to reduce the exposure to air and maintain pristine qualities of these materials. For example, previous work on hBN-encapsulated MoS_2 reveals ultra-high low temperature mobility up to $34,000\ \mathrm{cm}^2/(\mathrm{V}\cdot\mathrm{s})$ for 6-layer and $1,000\ \mathrm{cm}^2/(\mathrm{V}\cdot\mathrm{s})$ for CVD grown monolayer MoS_2 [32]. It is also seen that semiconducting/metallic 2D materials is combined with monolayer or few-layer graphene as transparent electrodes.

Furthermore, it is interesting to discover that the relative orientation between the individual layers can also make a difference. A moiré structure for graphene on hBN can lead to the formation of secondary Dirac points, Hofstadter butterfly effect and topological currents in such a system which has been reported by several groups [163, 35, 117, 62, 169]. Recently a heterostructure consisting of two graphene layers, in which the neighboring graphene are twisted relative to each other by a certain angle, is found to incubate exciting physics. At small twisting angles, the band structure of twisted bilayer graphene can be tailored to generate bandgaps and band curvatures

[17, 24], while at some particular 'magic' angles, the electronic band structure near zero Fermi energy becomes flat, where correlated insulator state and unconventional superconductivity is discovered [22, 23]. This is enabled by the the state-of-art pick-up techniques to control crystallographic alignment with an accuracy of less than 0.1°. In principle, these 'magic' angles which leads to a flat band is not limited to graphene and can be studied in many other 2D materials. A recent discovery of moiré excitons in van der Waals heterostructures [139, 128, 64, 4] also greatly advances research in this field. It is conceivable that more twisted 2D materials and novel physics can be added to the dreamscape of 2D heterostructures.

Other novel heterostructure devices such as MoS_2/WSe_2 p-n diodes, hybrid graphene-superconductor devices, van der Waals Josephson junctions, topological insulator-superconductor heterostructures, magnetic tunnel junctions [79, 38, 161, 160, 72, 133], to name a few, also emerges utilizing expanding 2D library. The pursuit of exploring more novel designs of heterostructures never stops.

1.2.2 Technique

It has been concerted efforts towards assembly of high quality van der Waals heterostructures. So far, manual assembly still remains the most favorite approach. In this method, micrometer-sized 2D crystals is obtained by mechanical exfoliation, or the Scotch-tape technique, which has so far proven unmatched quality. After exfoliation, these crystals can be sitting on top of a thin transparent film such as a polymer, or a substrate such as Si/SiO_2 wafer. The flake of interest is chosen after inspecting the substrate under an optical microscope.

For crystals exfoliated on top of transparent films, we can put the supporting film face down onto a chosen target followed by removing or dissolving the film. The alignment of the desired flake and the target position is carefully implemented using fine motorized stage under microscope with sub-micrometer accuracy. A picture of such a transfer stage is illustrated in Fig. 1-4. This process can be repeated again and again, until the whole heterostructure is completed. One concern of this approach is interfacial contamination. Adsorbates such as water, hydrocarbons and polymer

residues on top of the transferred crystals can be easily trapped in the interfaces of the heterostructure. Even after careful cleaning procedures such as thermal annealing in an inert atmosphere or under vacuum, or tip cleaning by atomic force microscope (AFM), these adsorbates cannot be completely removed. Sometimes it is difficult to find 'clean' area in the stack several nanometers in size that are free from contamination or bubble. To minimize contamination, it is desirable to ensure that no liquid or polymer is in direct contact with cleaved surfaces.

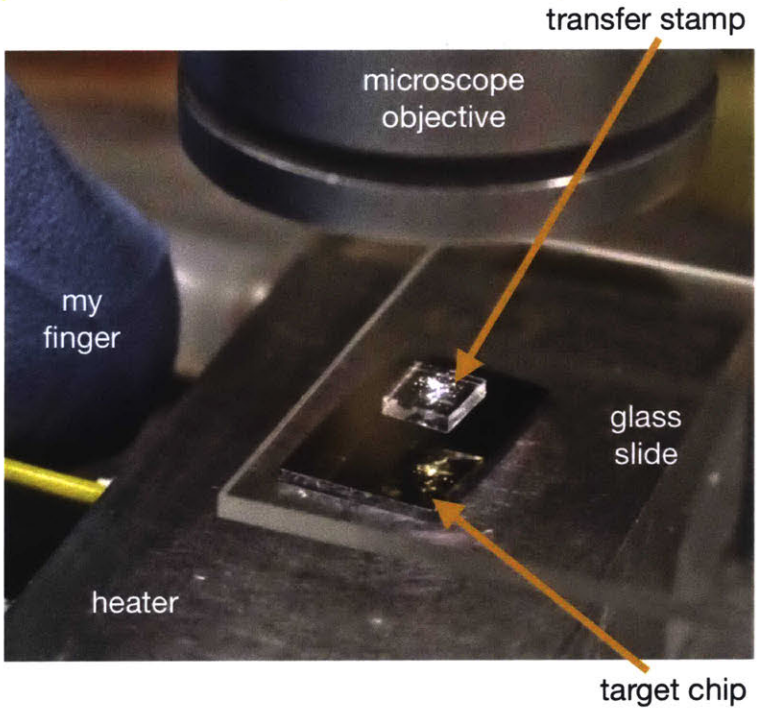

Figure 1-4: Picture of a transfer setup. At bottom is a motorized stage with a metal surface. A heater is installed inside the metal piece. Vacuum is initiated to hold the wafer piece and a glass slide with the polymer transfer stamp can be lowered and brought in touch with the wafer to allow crystal transfer. This process is inspected by an optical microscope.

Not long after the polymer transfer approach, a more efficient and substantially cleaner "pick-and-lift" method is invented. It utilizes strong van der Waals interactions that exist between the crystals. The crystals are no longer required to exfoliated on top of a special transparent film. Micrometer-sized 2D crystals can be picked up from their original substrate utilizing a polymer film - this film can be the same or a

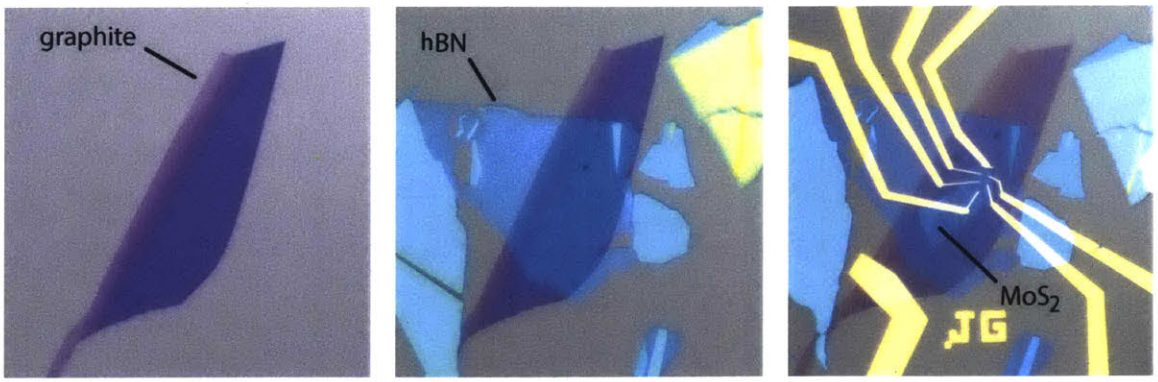

Figure 1-5: Heterostructures are built layer by layer from bottom to up. First, we exfoliated and identified a graphite flake on a Si/SiO_2 substrate, as shown in the first picture. Second, hBN is exfoliated on PDMS supported MMA thin film. We then put the MMA face down onto the substrate and heat the film, so that the MMA and the hBN on the film surface together will get transferred onto the substrate. The second picture shows the optical image after dissolving the MMA using acetone. We repeat this process and transfer another MoS_2 flake on top. At last, metal contacts are evaporated.

different type of polymer as what is mentioned in the previous paragraph. When the film with a 2D crystal on it is brought into contact with another 2D crystal, the second crystal tends to stick to the first and will be lifted together with it. The advantage of this "pick-and-lift" technique is that a stack can be produced by using the same film to pick up different flakes in sequence. Then the whole stack is transferred onto the final substrate. It is more time-efficient and leads to cleaner interface compared with the previous method, given that the film removal step is omitted and the 2D crystals never have direct contact with the polymer or any solvent. Moreover, this whole process can be done inside a glovebox with an inert atmosphere. More details about this technique can be found in the next chapter.

In the process of device assembly, contamination and bubble formation at interfaces are two of the most import factors that impact the device quality.

1.2.3 Contacts

Another problem that needs to be solved is how to probe individual layers after they are assembled into a stack. In order to dope or probe the electrical properties of

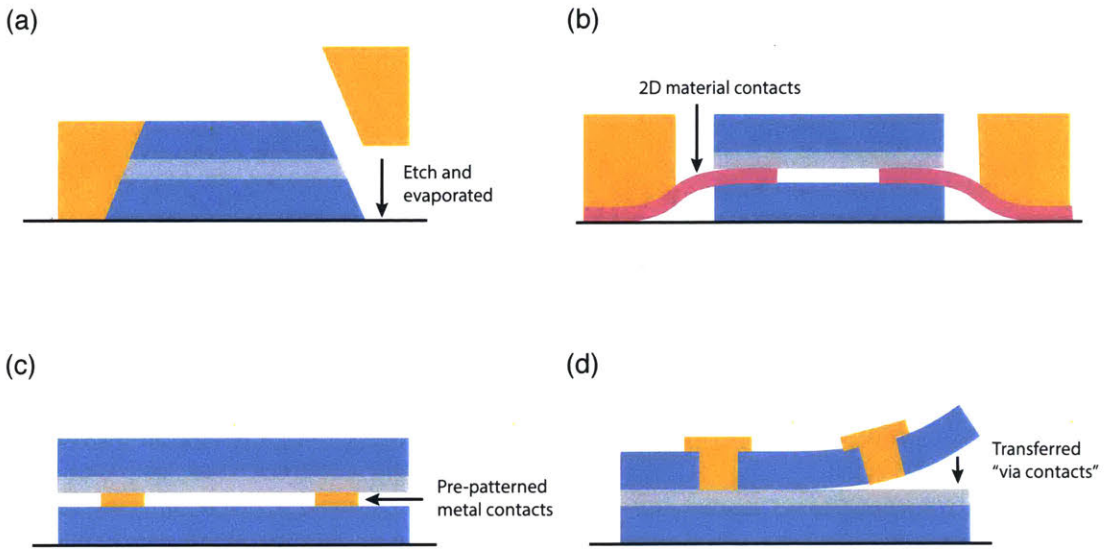

Figure 1-6: Methods to make contacts to the inner layer of a fully assembled van der Waals heterostructures. (a) 1D edge contacts. (b) Contacts made of van der Waals materials. (c) Pre-patterned metallic contacts. (d) Via contacts.

individual layers, contacts are needed. Several approaches have been discovered to make contacts to the inner layer of a fully assembled stack.

1D contacts is found to be excellent contacts for encapsulated graphene [148]. One can etch the edge of the stack into a desired shape in such a way that the inner layer is exposed and then contacted by metal evaporation. The contact resistance for graphene can be as low as 35 $\Omega \cdot \mu$m. It can be done after the whole stack is completed, thus all the layers in the stack remain flat and perfectly sealed, which ensures optimal device quality. Unfortunately, not all 2D materials can achieve such low contact resistance using this method.

It has been demonstrated that contacts made of 2D crystals such as graphene and TMDs exhibit exceptional mechanical and electrical performance. Their 2D nature make it compatible with the "pick-and-lift" concept and easily incorporated into heterostructure assembly. However, to shape the 2D crystals into contacts usually requires reactive plasma etching (otherwise, one can try to find search a particular shape such as a gap in between two crystals to allow for two-terminal contacts, but

the geometries that can be realized will be limited). It is found that the crystal contacts can become more fragile and harder to pick up after etching. This add extra complexity to device fabrication.

Metallic contact still remains one of the most popular choice in many heterostructure design. To comply with stack assembly, one can evaporate an ultra-thin layer of metal (thickness $\leq$ 5 nm) or make it embedded in supporting 2D materials. The 2D crystals of interest then can be transferred on top of the pre-patterned contact. This method works for most 2D materials and metals. The flatness and cleanness of the top surface of the contacts is crucial when aiming for low contact resistance. However, the metal surface in general has $\sim$1-2 nm roughness and it is difficult for the pre-patterned metal contacts to be perfectly flat and contamination free. It is likely that local strains and nonuniform contact to the material, imperfect seal around the protruding metal contact can impact the overall quality of the electronic contact. Recently, a new technique called "via method" is reported, where metal via contacts are integrated into flakes of insulating hBN, and then placed onto the desired 2D crystals, avoiding direct lithographic patterning [135]. In this process, the evaporated metal contacts are picked up together with the top hBN, which ensures flatness of the bottom surface of the contacts.

It is worth to mention that all the above approaches can be implemented in a glovebox or even under vacuum, which ensures minimum exposure to air and degradation.

Chapter 2

Semiconducting group-VI Dichalcogenides

2.1 Overview

Semiconducting group-VI dichalcogenides MX_2 (M = Mo, W, X = S, Se) manifest many interesting properties. Take MoS_2 as example, bulk MoS_2 has been studied since several decades ago [152], and is widely used as a dry lubricant due to its layered structure. As shown in crystal structure in Fig. 2-1 (b) and (c), the Mo atoms are sandwiched between two sheets of S atoms which form a trigonal prismatic geometry.

Multi-layer MoS_2 has an indirect band gap at Q points. However, when it is thinned down to a monolayer, it transits to a direct band gap. Similar to graphene, the conduction and valence band edge of monolayer MoS_2 is located at K points of its Brillouin zone (BZ). However, MoS_2 has a few important distinctions from graphene. First, the difference of sublattice potential leads to opening of a band gap at K points. Second, inversion symmetry is broken in 1H-MoS_2. Third, spin-orbit coupling (SOC) leads to opposite spin splitting of valence band at K, K' point, which is imposed by the time-reversal and inversion symmetries. This leads to possible ways to differentiate the two valleys and address them individually.

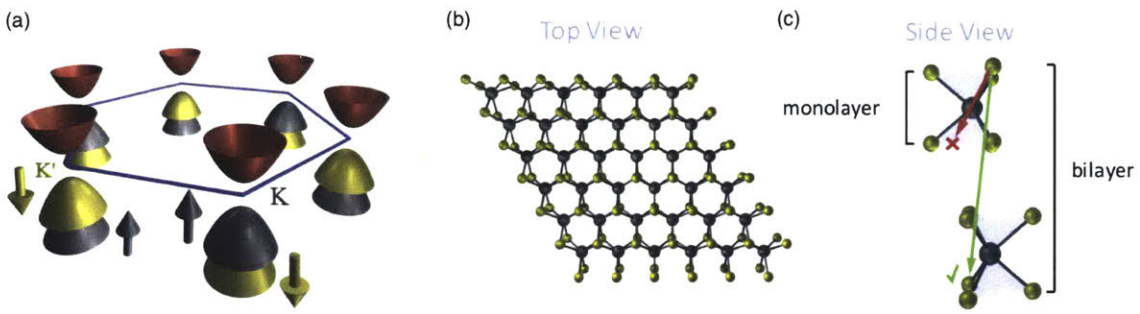

Figure 2-1: Overview of a semiconducting TMD crystal structure and band structure. (a) Schematic band structure of MoS_2 near the K valleys. The hexagonal lattice geometry of Mo and S atoms gives rise to K and K' valleys as similar to graphene. However, due to the lack of inversion symmetry in monolayer TMD and different mass of Mo and S atoms, a band gap and spin-orbit coupling develops. (b) The top view of the structure of a bulk TMD, consists of layered trigonal prismatic geometry of a transition metal atoms (grey) sandwiched between layers of chalcogen atoms (yellow). (c) The side view of a monolayer and bilayer TMD.

2.1.1 Band structure

Near the BZ inequivalent corners K and K′, the conduction and valence band states are approximately from $|\phi_c\rangle = |d_{z^2}\rangle$, $|\phi_v^{\tau_z}\rangle = (|d_{x^2-y^2}\rangle + i\tau_z |d_{xy}\rangle)/\sqrt{2}$ orbitals. Here $\tau_z = \pm 1$ labels the K and K' valley. To first order in momentum, the two-band $k \cdot p$ Hamiltonian of group-VI dichalcogenides can be expressed as [158]:

$$\hat{H}_0 = at(\tau_z k_x \hat{\sigma}_x + k_y \hat{\sigma}_y) + \Delta \hat{\sigma}_z \tag{2.1}$$

where $\hat{\sigma}$ is the Pauli matrices for the two basis functions of conduction/valence band, a is the lattice constant, t is the effective hopping integral, and 2Δ is the gap energy. When SOC is considered, the valence band will further split, whereas the conduction band remains spin degenerate. The total Hamiltonian takes the form:

$$\hat{H} = at(\tau_z k_x \hat{\sigma}_x + k_y \hat{\sigma}_y) + \Delta \hat{\sigma}_z - \lambda \tau_z (\hat{\sigma}_z - 1)\hat{s}_z \tag{2.2}$$

where 4λ is the spin splitting at the valence band top due to the SOC and $\hat{s}_z$ is the Pauli matrix for spin. This result in a splitting of spin up and spin down components.

In addition, such Hamiltonian can result in a none-zero Berry curvature centered

at the K valleys. For conduction band, the Berry curvature is given by:

$$\mathbf{\Omega}_c(\mathbf{k}) = -\tau_z \frac{2a^2t^2\Delta'}{(\Delta'^2 + 4a^2t^2k^2)^{3/2}} \tag{2.3}$$

where $\Delta' = 2(\Delta - \tau_z s_z \lambda)$ is the spin-dependent band gap. For valence band, $\mathbf{\Omega}_v = -\mathbf{\Omega}_c$. Note that the Berry curvatures have opposite sign in K and K' valleys. This can lead to novel transport behavior such as valley Hall effect [94].

For optical interband transitions near K points, the coupling strength with optical fields of $\sigma_\pm$ circular polarization is given by:

$$|\ \mathbf{P}_\pm(\mathbf{k})\ |^2 = \frac{a^2t^2m_0^2}{\hbar^2}(1 \pm \frac{\tau_z\Delta'}{(\Delta'^2 + 4a^2t^2k^2)^{1/2}})^2 \tag{2.4}$$

Here $\Delta' \gg atk$, thus the interband transitions are coupled exclusively with $\sigma_+(\sigma_-)$ circularly polarized light at the K(K') valley. Since the spin up and spin down components at top valence band is split and spin is conserved in optical transitions, the valley optical selection rule will be spin dependent. It has been demonstrated that the excitonic valley polarization and coherence in 2D TMDs can be generated by pumping with circularly polarized light and linearly polarized light, respectively [171, 92, 154, 21, 65].

2.2 Transport properties of MoS_2

2.2.1 Device fabrication

In this section, we briefly introduce the intrinsic electronic transport properties of high quality monolayer and bilayer MoS_2.[1] The device geometry is shown in Fig. 2-2. Micro-sized MoS_2 crystals (from SPI) are exfoliated on standard Si/SiO_2 wafers (highly doped silicon with 285 nm SiO_2 on top). Ti/Au contacts are then patterned with e-beam lithography and evaporated. After transferred into the measurement probe and pumped down in vacuum (10^{-6} mbar), the device is annealed *in situ*

[1] This work is done with Britton Baugher, Hugh Churchill and Pablo Jarillo-Herrero, and appeared in the journal Nano Letters [13].

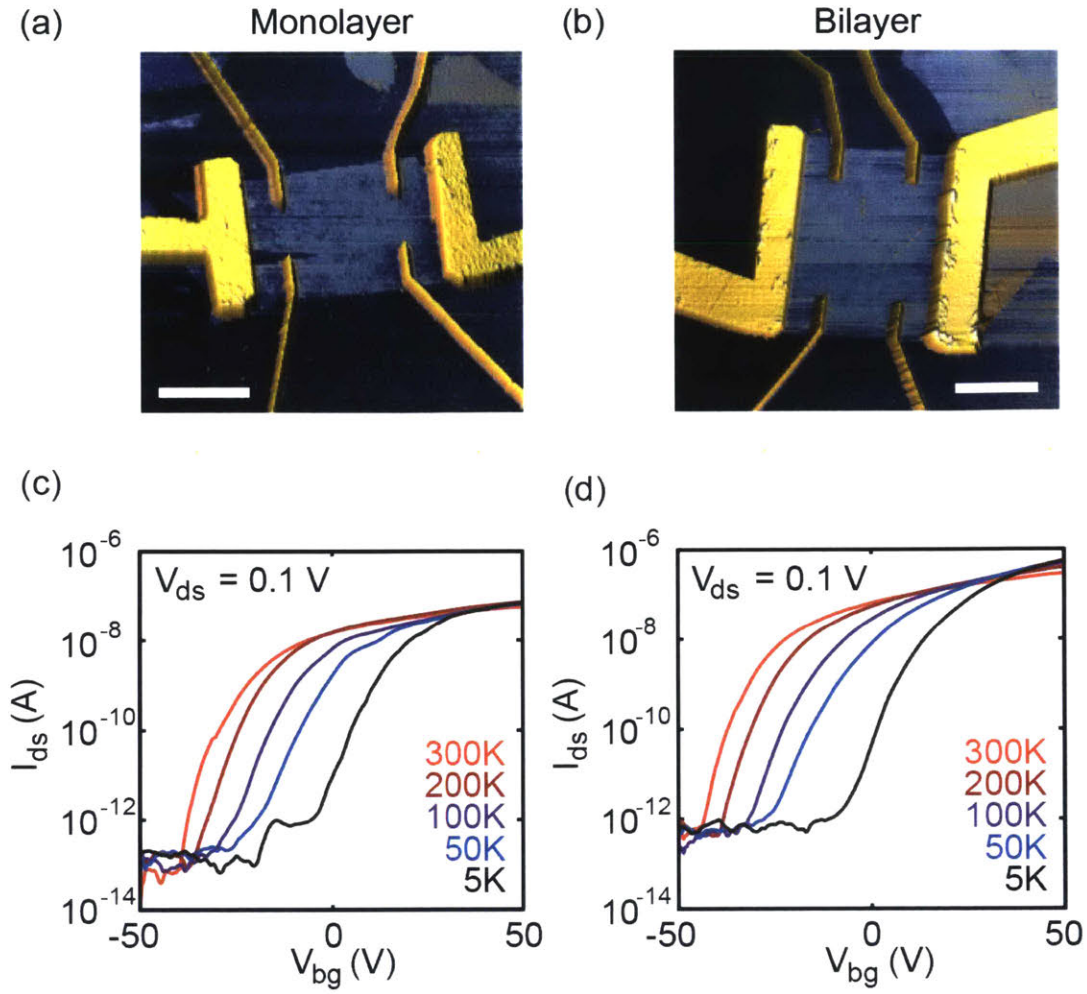

Figure 2-2: Device geometry: Color-enhanced AFM height image of (a) monolayer and (b) bilayer MoS_2 devices. Scale bars are 2 μm. Two-terminal transport measurements: drain-source current, I_{ds}, of (c) monolayer and (d) bilayer MoS_2 as a function of back-gate voltage, V_{bg} at temperature from 300 K to 5 K are denoted with colors from red to black.

at $\sim$ 120 °C for up to 20 hours. After such annealing, the contact quality gets significantly improved and two-terminal $I - V$ achieves nearly ohmic behavior. It is also found that the annealing process tends to n-dope the sample.

2.2.2 Transport result

With the device shown in Fig. 2-2, a voltage, V_{ds}, is applied to the source lead, while current, I_{ds}, is collected at the drain lead. The voltage drop between two inner contacts is measured as V_{xx}. Fig. 2-3 shows the contact resistance and resistivity of

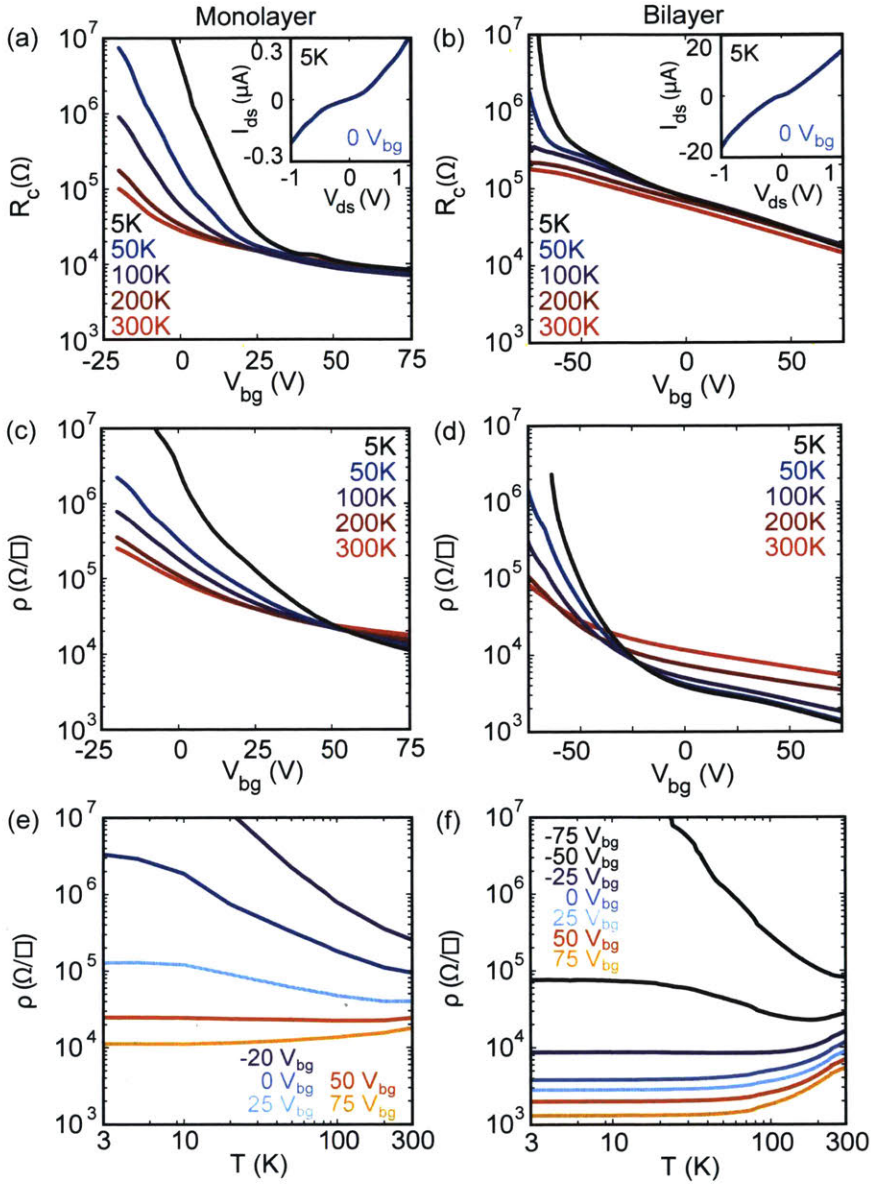

Figure 2-3: Contact resistance and four-terminal resistivity of monolayer and bilayer MoS_2. First row: contact resistance, R_c, of (a) monolayer and (b) bilayer MoS_2 as a function of V_{bg}. Colors from red to black indicate measurement temperatures of 300, 200, 100, 50, and 5 K, respectively. Inset of (a) and (b): two-terminal I_{ds} vs. V_{ds} at 5 K and $V_{bg} = 0$ V for the device. Second row: four-terminal resistivity of a (c) monolayer and (d) bilayer device as a function of V_{bg}. Third row: temperature depedent resistivity of a (e) monolayer and (f) bilayer device. Different colors correspond to different V_{bg}.

monolayer and bilayer MoS_2 devices measured at various temperatures and back-gate voltages. The contact resistance is given by:

$$R_c = V_{ds}/I_{ds} - \rho \cdot l/w$$

where l and w are the length and width of our devices. The resistivity of our 2D sample is then expressed as:

$$\rho = (V_{xx}/I_{ds}) \cdot (w/l_{in})$$

where l_{in} is the length between the two inner contacts.

Contact resistance is a few 10^4 to 10^5 Ω for highly n-doped monolayer and bilayer samples at a wide range of temperatures, and increases as temperature decreases. It is not optimal, indicating the presence of Schottky barriers between contacts and the sample, but it is small enough to allow characterization of its transport behavior using a 4-probe geometry. From Fig. 2-3 (e)(f), we clearly observe a metal-insulator transition (MIT) in both monolayer and bilayer samples as the device becomes less n-doped. It is worth noting that the critical resistivity of MIT of all of our monolayer and bilayer samples are of order h/e^2.

Mobility is an important parameter that characterizes the quality of a device. One method is to calculate the field-effect mobility, μ_{FE}, which can be deduced from the field-effect transistor curve as shown in Fig. 2-2 (c)(d) with the formula below:

$$\mu_{FE} = \frac{1}{c}\frac{\mathrm{d}\sigma}{\mathrm{d}V_{bg}} \tag{2.5}$$

where $c = \epsilon_r\epsilon_0/d$ is the gate capacitance per unit area, which is 12 nF/cm^2 derived for 285 nm of SiO_2. The yellow traces in Fig. 2-4 (a)(b) show the extracted μ_{FE} as a function of V_{bg} for monolayer and bilayer samples. We can see that μ_{FE} reaches as high as $\sim$ 1000 cm^2/Vs. Another method to measure the mobility is Hall effect measurement.

We therefore conducted Hall measurement, from which carrier density as a func-

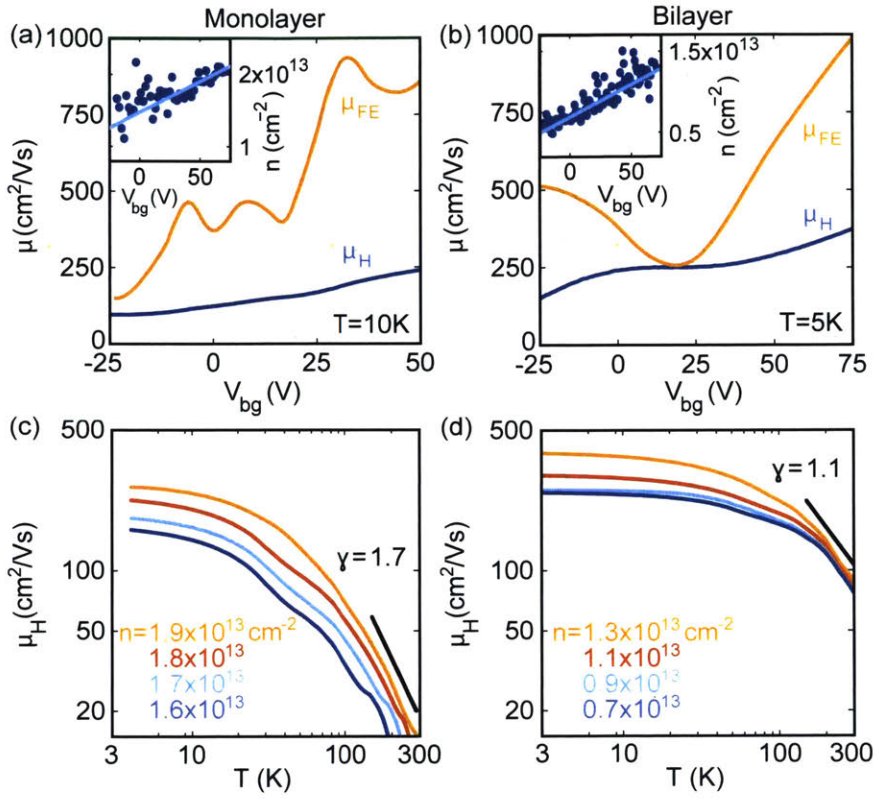

Figure 2-4: Field-effect mobility and Hall mobilities as a function of V_{bg} and temperature for monolayer and bilayer MoS_2. (a) Field-effect mobility, μ_{FE} (yellow), and Hall mobility, μ_H (blue), of a monolayer device as a function of back-gate voltage, V_{bg}, at 10 K. Inset: Density of a monolayer device as a function of V_{bg} at 10 K. Solid lines in the insets to (a) and (b) are fits to $n = mV_{bg} + b$, where the slope, m, and the intercept, b, are free parameters. (b) μ_{FE} (yellow) and μ_H (blue) of a bilayer device as a function of V_{bg} at 5 K. Inset: Density of a bilayer device as a function of V_{bg} at 5 K. (c) μ_H as a function of temperature for a monolayer device. The curves, from blue to yellow, correspond to $n = 1.6$, 1.7, 1.8, and $1.9 \cdot 10^{13}$ cm^{-2}. The black line is a power law fit, $\mu_H \propto T^{-\gamma}$, with $\gamma = 1.7$ for the high density data from 150-300 K. (d) μ_H as a function of temperature for a bilayer device. The curves, from blue to yellow, correspond to $n = 0.7$, 0.9, 1.1, and $1.3 \cdot 10^{13}$ cm^{-2}. The black line is a power law fit, $\mu_H \propto T^{-\gamma}$, with $\gamma = 1.1$ for the high density data from 150-300 K.

tion of back-gate voltage can be determined. A perpendicular magnetic field up to 1 T is applied and longitudinal/transverse resistance, R_{xx} and R_{xy}, is measured. By fitting the slope of R_{xy} vs. magnetic field, we can extract the Hall coefficient $R_H = 1/ne$, as well as carrier density, n, as a function of V_{bg} and temperature. With knowledge of both ρ and n deduced from R_{xx} and R_{xy}, Hall mobility is extracted as $\mu_H = \sigma/ne$, where $\sigma = 1/\rho$ is the conductivity and e is the electron charge.

In Fig. 2-4 (a)(b) we plot μ_H as a function of V_{bg} for monolayer and bilayer samples. The Hall mobilities reaches 250 cm^2/Vs for the monolayer and 375 cm^2/Vs for the bilayer when samples are more n-doped, and generally increases with doping. The inset is the carrier density vs. V_{bg} measured by Hall effect and the slope agrees reasonably well with a parallel plate geometry with a layer of 285 nm of SiO_2 as dielectric. However, there is a clear discrepancy between $\mu_F E$ and μ_H. To explain such discrepancy, let's take a closer look of how μ_{FE} is derived. It assumes $\sigma = ne\mu$ and $ne = cV_{bg}$, where $\mu = \mu_H$, given that Hall effect extracts the 'true' mobility. Based on field-effect mobility formula in Eq. 2.5:

$$\mu_{FE} = \frac{\mathrm{d}}{\mathrm{d}n}(\mu_H n) = \mu_H + n\frac{\mathrm{d}\mu_H}{\mathrm{d}n} \tag{2.6}$$

Eq. 2.6 reveals interesting relationship between μ_H and μ_{FE}. When mobility is not dependent on carrier density, μ_H and μ_{FE} should more or less match each other. However, discrepancy can occur if the term $\frac{\mathrm{d}\mu_H}{\mathrm{d}n}$ is not negligible. This is in agreement with our observation that in the back-gate range where μ_H is nearly independent of density, μ_{FE} approaches μ_H. Since the mobility increases with carrier density at most back-gate voltages, μ_{FE} tends to overestimate sample mobility.

At last, we plot Hall mobility as a function of temperature and study its trend. We constrain our study in the metallic regime, where samples are highly n-doped. It is seen in in Fig. 2-4 (c)(d) that Hall mobility for both monolayer and bilayer samples increase monotonically from 300 K to 5 K, following a power law $\mu_H \propto T^{-\gamma}$, and saturate below $\sim$ 100 K. It is likely that our sample crossovers from optical phonon limited mobility at high temperatures to defect limited mobility at low temperatures.

In this section, we demonstrate transport properties of high-quality, ultra-thin MoS_2 devices. However, considerable experimental efforts are still needed to investigate novel quantum transport phenomena at low temperature. First, Schottky barriers are not eliminated and contact resistance is still large at low temperature and low doping regimes. Second, Hall mobility of our device is only a few hundred, insufficient to allow for quantum transport phenomena at low temperatures under a laboratory-scale magnetic field.

2.3 Optoelectronic devices based on WSe_2

In this section, we report optoelectronic devices based on electrically tunable p–n diodes in a monolayer WSe_2.[2]

As mentioned in Chapter 1, TMDs are promising candidates for ultrathin, flexible, high-strength and nearly transparent optoelectronic and electronic devices. Among a variety of devices, p-n junctions are probably the most fundamental and widely studied building blocks of modern optoelectronic and electronic devices. Motivated by previous studies on carbon nanotubes [81], we propose that a lateral p-n junction can be realized in TMDs defined and controlled by electrostatic gates. We choose monolayer WSe_2 as the host material, since it has a direct band gap of $\sim$ 1.65 eV and its natural crystals are nearly intrinsic and ambipolar [149]. Conversely, natural MoS_2 is usually n-dope and unipolar [119].

The device schematics (side view) is shown in Fig. 2-5. At the bottom, two local back-gate separated by a gap of 100 nm is patterned using e-beam lithography. It is made of 20 nm thick Au deposited by e-beam evaporation. A uniform layer of HfO_2 (20 nm thickness) is grown on top by atomic layer deposition and serve as a dielectric. WSe_2 crystals are exfoliated directly onto a transfer slide composed of a stack of glass, a transparent polymer support (polydimethylsiloxane, PDMS) and a polymer film (methyl methacrylate, MMA) [36]. The slide is then inspected under microscope

[2]This work is done with Britton Baugher, Hugh Churchill and Pablo Jarillo-Herrero, and appeared in the journal Nature Nanotechnology [14].

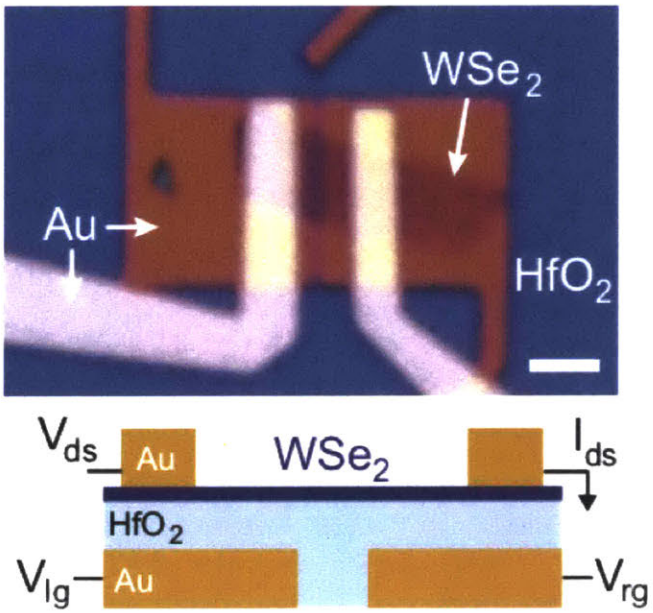

Figure 2-5: Device image and schematics. Top: optical image of a monolayer WSe_2 device controlled by two local gates. The WSe_2 is contacted with gold electrodes. The flake and contacts are insulated from the gates by 20 nm of HfO_2. Scale bar is 2 μm. Bottom: schematic side view of the device including electrical connections.

and monolayer WSe_2 can be identified by optical contrast and later confirmed by AFM or photoluminescence. The identified monolayer WSe_2 is then transferred onto the prepared split-gate, followed by removing the MMA film covering on top. The WSe_2 is then contacted by two electrodes (Cr/Au 0.3/25 nm), each $\sim$1 μm wide. Finally, the device is transported to a scanning photocurrent microscopy set-up for measurement.

By applying voltage to the two back-gates, we can achieve independent control of the carrier density in the left/right side of the device. Depending on the voltages applied to each gate, the device can be electrostatically doped into different configurations. When both sides are n-doped or p-doped ($V_{lg} = V_{rg} = \pm 10$ V), we call it NN or PP, whereas when two sides are oppositely doped ($V_{lg} = -V_{rg} = \pm 10$ V), we call it NP or PN configuration. The maximum voltage than can be applied to the back-gate is determined by the the dielectric strength of HfO_2 dielectric, which is approximately 0.5 V/nm.

It is observed that the device manifests a nearly linear current–voltage relationship

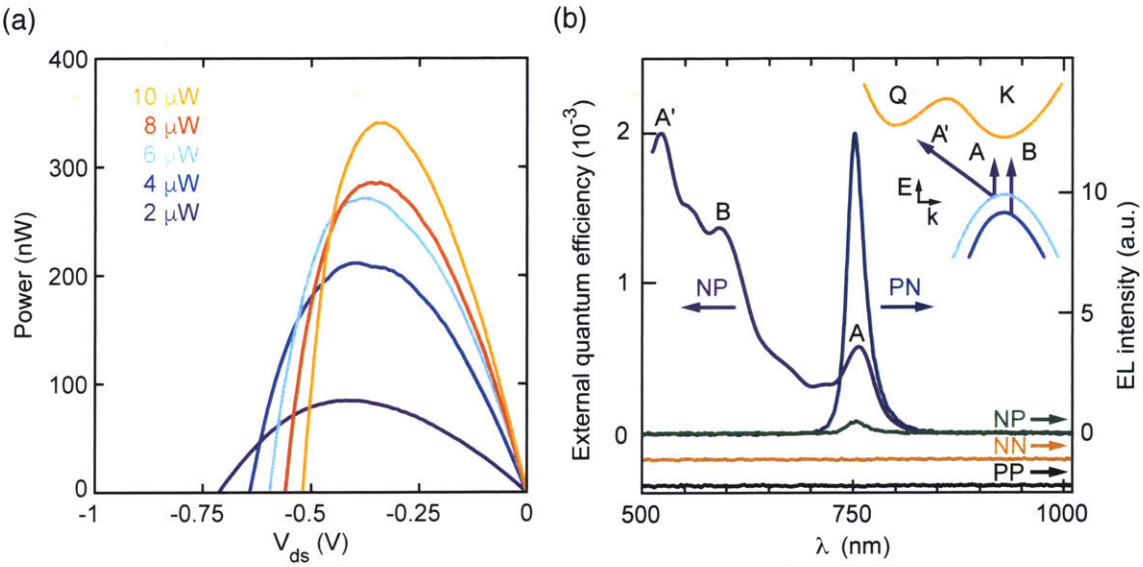

Figure 2-6: Photovoltaic response of p-n diodes in a second monolayer WSe_2. (a) Power, $P = I_{ds} \cdot V_{ds}$, produced by the device as a function of V_{ds} for different incident laser powers ranging from $2-10$ μW with wavelength 700 nm. It is calculated from the $I_{ds} - V_{ds}$ curves in the NP configuration. (b) Left axis: External quantum efficiency as a function of wavelength at a constant laser power of 2 μW. Peaks in the external quantum efficiency correspond to exciton transitions A, B, and A', as labeled. Right axis: EL intensity from the monolayer WSe_2 device shown in Fig. 2-7 with different electrical configurations. $V_{ds} = 2$ V in the PN, NN, and PP configurations, and $V_{ds} = -2$ V in the NP configuration. NN and PP traces are offset vertically for clarity. Inset: Diagram of the band structure around the K and Q points, with arrows indicating the lowest energy exciton transitions for monolayer WSe_2.

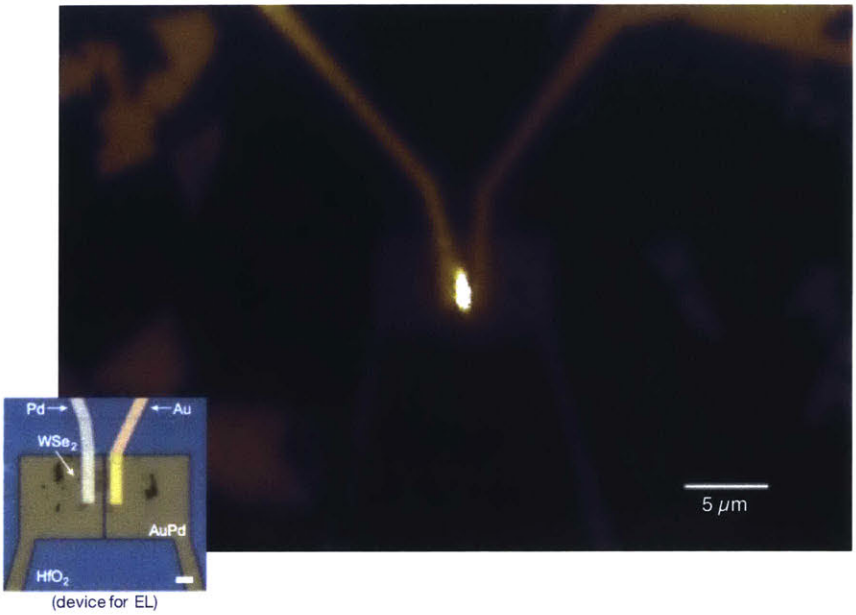

Figure 2-7: Color-enhanced reflected image of an electrically defined p-n junction in a monolayer WSe_2 that emits light as a micro-LED. Inset: optical image of the device with one Au and one Pd contact, optimized for PN configuration. Scale bar is 1 μm.

in NN and PP configurations, although the device is much more conductive in NN configuration. We later found that Au is better for n-type contact while Pd is better for p-type contact of WSe_2. In NP and PN configuration, the device can work as current-rectifying diodes, a light-emitting diode and a solar cell. In Fig. 2-6 we demonstrate that this device is capable of photovoltaic power generation. With the device in the NP configuration, current, I_{ds}, is measured as a function of source-drain voltage, V_{ds}, for different laser powers (wavelength fixed at 700 nm). We then convert it to power generation of the photovoltaic device, given by $P = I_{ds} \cdot V_{ds}$. It is shown in In Fig. 2-6 (a) for various laser powers $0 - 10$ μW.

An important variable that measures the efficiency of photocurrent generation at a particular wavelength is external quantum efficiency, or EQE, which is given by

$$\text{EQE} = (I_{sc}/P_{laser})(hc/e\lambda) \tag{2.7}$$

where I_{sc} is the short-circuit current, which is the zero-bias current through the illuminated device, λ is excitation wavelength, P_{laser} is the laser power and h, c, and

e, are Planck's constant, speed of light, and electron charge, respectively. To obtain spectrally resolved EQE in our device, we tune the device into NP configuration and measure I_{sc} as a function of excitation wavelength. EQE is extracted using Eq. 2.7 as a function of excitation wavelength and plotted in Fig. 2-6 (b). We observe three peaks located at wavelength 755, 591, and 522 nm, corresponding to energies of 1.64, 2.10, and 2.38 eV, respectively. These match well with previous experimental observations [174] for the A, B, and A′ optical transitions of monolayer WSe_2, as illustrated in the inset of Fig. 2-6 (b). For green light at 522 nm, the EQE has a peak of 0.2%. This is comparable with commercially available silicon photodetectors from green light. Considering the fact that the light absorption rate of monolayer WSe_2 is only 5-10% and the cross-section of the PN junction is much smaller than the size of the laser beam, the actual EQE of our device can be at least an order of magnitude larger than the reported value here.

In order to improve p-type contacts on one side, we intentionally replace one Au contact with Pd contact to enhance the current injection in PN configuration. The device image is shown in the inset of Fig. 2-7. This improvement allows us to measure the light emission of the diode. The reflected image is shown in Fig. 2-7. Here $V_{ds} = 2$ V, and $I_{ds} = 100$ nA. The spectrum resolved light emission is shown in Fig. 2-6 (b) with a peak located at 752 nm, corresponding to the A transition depicted in the inset. It also matches well with the peak of photocurrent generation. The light emission in other configuration (NP, PP, NN) is also shown in Fig. 2-6 (b). For NP, the light emission is much weaker due to the small current injection, $I_{ds} = 4$ nA $\ll 200$ nA with $V_{ds} = -2$ V. No light emission is observed in NN and PP configurations, verifying that the electroluminescence is generated by the gate defined p-n junctions.

This work highlights the world's thinest solar cell and LED that is made of a single layer of atomically layered TMDs.

Chapter 3

Towards Quantum Transport in Semiconducting Dichalcogenides

Electrons in monolayer transition metal dichalcogenides are characterized by valley and spin quantum degrees of freedom. It has been theoretically proposed that Berry curvature effects, together with strong spin–orbit interactions, can generate unconventional Landau levels (LLs) under a perpendicular magnetic field [85, 19]. In particular, these would support valley- and spin-polarized chiral edge states in the quantum Hall regime. However, it is very challenging to observe LLs structure in monolayer TMDs, mainly due to the sample quality and contact problem. In this chapter, we will describe the theoretical scenarios and experimental approaches towards quantum transport in TMDs.

3.1 Unconventional quantum Hall effect in TMDs

3.1.1 Quantum Hall effect

Let's briefly review the quantum Hall effect [34]. It is first discovered by K. v. Klitzing, G. Dorda, and M. Pepper in 1980 [73].

The dynamics of electronic conduction in semiconductors can be described by a

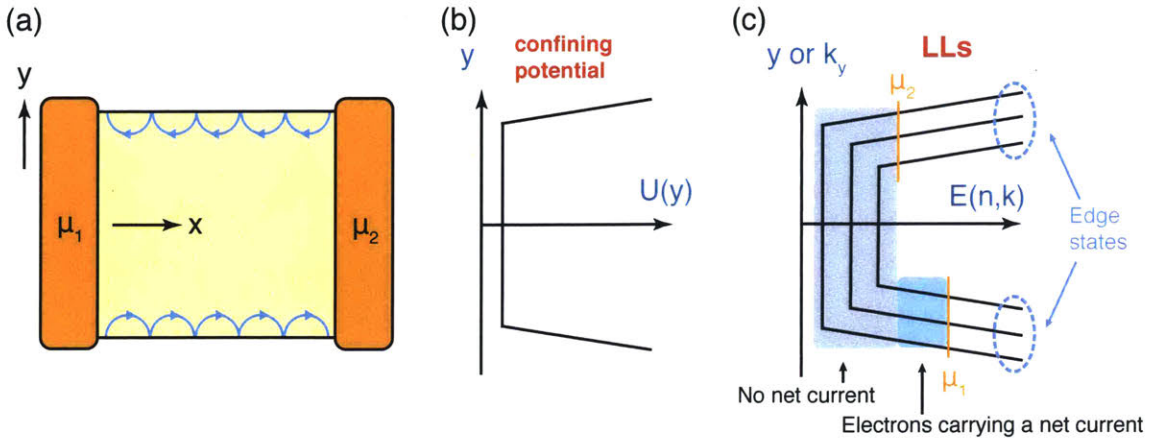

Figure 3-1: Quantum Hall effect. (a) A two-dimensional conductor assumed to be uniform in x direction in the quantum Hall regime. The edge states are in equilibrium of with the source contacts. (b) Sketch of confining potential $U(y)$ versus y. (c) Sketch of the approximate dispersion relationship of energy versus y or k_y assuming that the confining potential varies slowly over a cyclotron radius.

single-band effective mass equation:

$$\left[E_c + \frac{(i\hbar\nabla + e\mathbf{A})^2}{2m} + U(\mathbf{r})\right]\Psi(\mathbf{r}) = E\Psi(\mathbf{r}) \tag{3.1}$$

where $U(\mathbf{r})$ is the potential energy, $\mathbf{A}$ is the vector potential and m is effective mass. In a 2D conductor we assume a parabolic confining potential in y direction (transverse direction)

$$U(y) = \frac{1}{2}m\omega_0^2 y^2 \tag{3.2}$$

By substituting Eq. 3.2 into Eq. 3.1, we obtain

$$\left[E_c + \frac{(i\hbar\nabla + e\mathbf{A})^2}{2m} + U(y)\right]\Psi(x,y) = E\Psi(x,y) \tag{3.3}$$

Without confining potential ($U(y) = 0$), the solution to Eq. 3.3 would be

$$\begin{aligned} \Psi_{n,k}(x,y) &= \frac{1}{L}\exp[ikx]u_n(q+q_k) \equiv |\, n,k\,\rangle \\ E_{n,k} &= E_s + (n+1/2)\hbar\omega_c, \quad n = 0,1,2,... \end{aligned} \tag{3.4}$$

where

$$u_n(q) = \exp\left[-q^2/2\right] H_n(q)$$

$$q = \sqrt{m\omega_c/\hbar}y \text{ and } q_k = \sqrt{m\omega_c/\hbar}y_k$$

$$y_k \equiv \frac{\hbar k}{eB} \text{ and } \omega_c \equiv \frac{|e|B}{m}$$

$H_n(q)$ is the nth Hermite polynomial.

We can use the lowest order perturbation theory to take into account the confining potetial $U(y)$:

$$E_{n,k} = E_s + (n + 1/2)\hbar\omega_c + \langle\, n, k \,|\, U(y) \,|\, n, k \,\rangle$$

Note that the center of each state $|\, n, k \,\rangle$ is around a different location $y = y_k$ in the transverse direction and spread over of $\sim \sqrt{\hbar/m\omega_c}$. Within such spatial extent, $U(y)$ can be treated as a constant, so that

$$E_{n,k} = E_s + (n + 1/2)\hbar\omega_c + U(y_k), \text{ where } y_k = \hbar k/eB \tag{3.5}$$

The velocity of edge states can be calculated as follows:

$$v(n,k) = \frac{1}{\hbar}\frac{\partial E(n,k)}{\partial k} = \frac{1}{\hbar}\frac{\partial U(y_k)}{\partial k} = \frac{1}{\hbar}\frac{\partial U(y)}{\partial y}\frac{\partial y_k}{\partial k} = \frac{1}{eB}\frac{\partial U(y)}{\partial y}$$

The current carried by the edge states is given by

$$I = \frac{2e}{h}M(\mu_1 - \mu_2) \tag{3.6}$$

where M is the number of edge states.

3.1.2 Single particle model: Landau levels in TMDs

As shown in Sec. 2.1.1, the two-band $k \cdot p$ Hamiltonian of group-VI dichalcogenides can be expressed as Eq. 2.2, and we rewrite as follows:

$$\hat{H} = v(\tau_z p_x \hat{\sigma}_x + p_y \hat{\sigma}_y) + \Delta\hat{\sigma}_z - \lambda\tau_z(\hat{\sigma}_z - 1)\hat{s}_z \tag{3.7}$$

where $v = at/\hbar \sim 0.53 \times 10^6$ m/s.

By expanding the momentum close to the K point, the Hamiltonian reads

$$\mathcal{H}_K = \begin{pmatrix} \Delta & 0 & v(p_x - ip_y) & 0 \\ 0 & \Delta & 0 & v(p_x - ip_y) \\ v(p_x + ip_y) & 0 & -\Delta + 2\lambda & 0 \\ 0 & v(p_x + ip_y) & 0 & -\Delta - 2\lambda \end{pmatrix} \tag{3.8}$$

while close to the K′ point, the Hamiltonian reads

$$\mathcal{H}_{K'} = \begin{pmatrix} \Delta & 0 & v(-p_x - ip_y) & 0 \\ 0 & \Delta & 0 & v(-p_x - ip_y) \\ v(-p_x + ip_y) & 0 & -\Delta - 2\lambda & 0 \\ 0 & v(-p_x + ip_y) & 0 & -\Delta + 2\lambda \end{pmatrix} \tag{3.9}$$

The base wave-functions are $|\Psi_{c,\uparrow}\rangle$, $|\Psi_{c,\downarrow}\rangle$, $|\Psi_{v,\uparrow}\rangle$, $|\Psi_{v,\downarrow}\rangle$, where c and v denote the conduction band and valence band respectively. As a combined effect of broken inversion symmetry and strong SOC, the valence band is split with opposite shift for the $\tau_z s_z = \pm 1$ bands, adjusting the energy gaps to $2(\Delta - \lambda)$ for $\tau_z s_z = 1$ bands and to $2(\Delta + \lambda)$ for $\tau_z s_z = -1$ bands. From DFT calculations [158], $\Delta = 830$ meV and $\lambda = 37.5$ meV.

In the presence of a uniform perpendicular magnetic field, the 2D kinetic momentum p in Eq. 3.7 is replaced $\pi = \mathbf{p} + e\mathbf{A}/c$. In the Landau gauge $\mathbf{A} = (0, Bx)$, the operator $\pi = \pi_x + i\pi_y$ coincide with the lowering operators satisfying $\pi\phi_n = -i\sqrt{2n}(\hbar/\ell_B)\phi_{n-1}$ and $\pi\phi_0 = 0$, where ϕ_n $(n = 0, 1, 2, ...)$ are the Landau level eigenstates for a conventional 2D electron gas.

Assuming $\hbar v/\ell_B$ is smaller than the band width and the effects of Zeeman couplings, disorders and Coulomb interactions are relatively small, the flavor-dependent LL spectrum is given by [85]

$$E_{n,\pm} = \lambda\tau_z s_z \pm \sqrt{n\hbar^2\omega_c^2 + (\Delta - \lambda\tau_z s_z)^2} \tag{3.10}$$

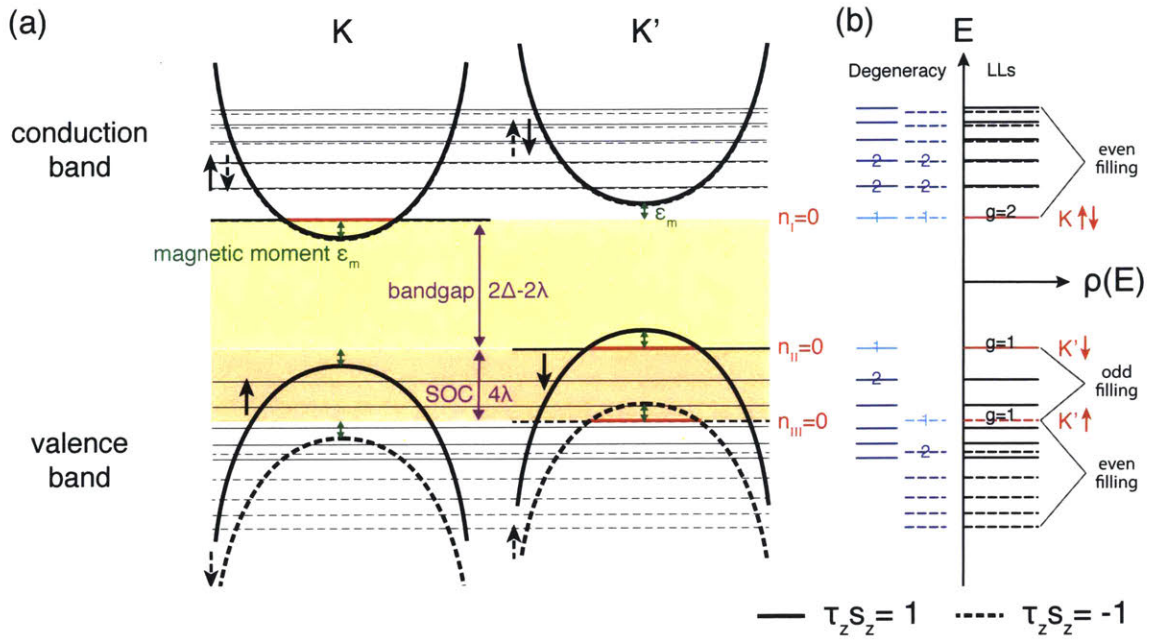

Figure 3-2: Band structure and LLs of group-VI TMDs. (a) Sketch: the solid (dashed) curves represent $\tau_z s_z = 1$ (-1) bands and the parallel lines denote their LLs. The original band has a band-gap of 2Δ and SOC induced splitting at valence band. The band dispersion is shifted by the Zeeman-like coupling between magnetic moment $\mathbf{m}(\mathbf{k})$ and the magnetic field by $\epsilon_m = -\mathbf{m} \cdot \mathbf{B}$. $n = 0$ LLs that are depicted by red lines and are located at original conduction band and valence band edges. (b) Single particle LL spectrum and degeneracy of each LL. SOC breaks LLs into two groups with $\tau_z s_z = \pm 1$, which have different slopes in B. The $n_{\mathrm{I}} = 0$ LL is spin degenerate (degeneracy $g = 2$) and only appears at K valley. The $n_{\mathrm{II,III}} = 0$ LLs are spin filtered (degeneracy $g = 1$) and appear only at K′ valley. All other LLs have degeneracy $g = 2$.

where $\ell_B = \sqrt{\hbar/(eB)} = 25.6/\sqrt{B[T]}$ nm is the magnetic length and $\omega_c = \sqrt{2}v/\ell_b$ is the cyclotron frequency. The calculated LL spectrum is depicted in Fig. 3-1 (b). We observe that the Landau level spacing is not uniform. The corresponding eigenstates with $n > 0$ can be written as

$$\text{for K valley:} \quad \begin{pmatrix} \phi_n \\ a^{\pm}_{n,s_z}\phi_{n-1} \end{pmatrix} \tag{3.11}$$

$$\text{for K}' \text{ valley:} \quad \begin{pmatrix} b^{\pm}_{n,s_z}\phi_{n-1} \\ \phi_n \end{pmatrix} \tag{3.12}$$

For $n = 0$ LLs, the eigenstates are $\begin{pmatrix} 0 \\ \phi_0 \end{pmatrix}$ for conduction band with energy Δ, and $\begin{pmatrix} \phi_0 \\ 0 \end{pmatrix}$ for valence band with energy $-\Delta - 2\lambda s_z$.

The eigenstates for $n = 0$ LLs indicate that the 0_+ LLs are only at K valley and 0_- LLs are only at K′ valley. We further note that $n_+ = 0$ Landau level at the K valley is at the same energy of the original conduction-band bottom at zero field, while for K′ valley there is no Landau level at this energy. This peculiar asymmetric behavior [19] can be traced to the chirality difference between the two valleys and the intrinsic orbital magnetic moments arising from none-zero Berry curvatures as shown in Eq. 2.3. The general expression is given by

$$\mathbf{m}(\mathbf{k}) = -i\frac{e}{2\hbar} \langle \nabla_{\mathbf{k}} u | \times [H(\mathbf{k}) - \epsilon(\mathbf{k})] | \nabla_{\mathbf{k}} u \rangle \tag{3.13}$$

where $| u \rangle$ is the periodic part of the Bloch eigenstate, $H(\mathbf{k})$ is the Bloch Hamiltonian, and $\epsilon_{\mathbf{k}}$ is the band energy. For our case

$$\mathbf{m}(\mathbf{k}) = \tau_z \frac{e\hbar v^2 \Delta'}{(\Delta'^2 + 4\hbar^2 v^2 k^2)} \hat{z} \tag{3.14}$$

The moment is largest at the band edges and opposite for different valleys ($\tau_z = \pm 1$). In the presence of an external magnetic field $\mathbf{B}$, the wave-packet energy would be shifted by $\epsilon_m = -\mathbf{m} \cdot \mathbf{B}$. The bands at the two valleys are thus shifted to opposite directions. This is shown in Fig. 3-2 that the band dispersion is shifted by the Zeeman-like coupling between magnetic moment $\mathbf{m}(\mathbf{k})$ and the magnetic field. The $n = 0$ LLs are depicted by red lines and are located at the original conduction band and valence band edges.

We divide the LLs into three groups, group I for $\tau_z s_z = \pm 1$ conduction band, group II and III for $\tau_z s_z = 1$ and $\tau_z s_z = -1$ valence band, respectively, as denoted in Fig. 3-3. A detailed LL spectrum can be found in Ref. [85]. $n_{\mathrm{I}} = 0$ LLs at conduction band are two-fold spin-degenerate ($\tau_z = 1, s_z = \pm 1$) at K valley, while $n_{\mathrm{II,III}} = 0$ LLs at valence band are spin-split and none-degenerate ($\tau_z = -1, s_z = -1$ for group II,

and $\tau_z = -1, s_z = +1$ for group III) at K′ valley. $n = 0$ LLs that are depicted by red lines in Fig. 3-2 (a). $n \neq 0$ LLs are still doubly degenerate in each group, consisting of one spin $\uparrow$ state from one valley and one spin $\downarrow$ state from the other valley. This leads to filling factor $\nu = 0, 2, -1$ but not $\nu = 1$, where ν corresponds to $\sigma_{xy} = \nu e^2/h$ measured in quantum Hall effect.

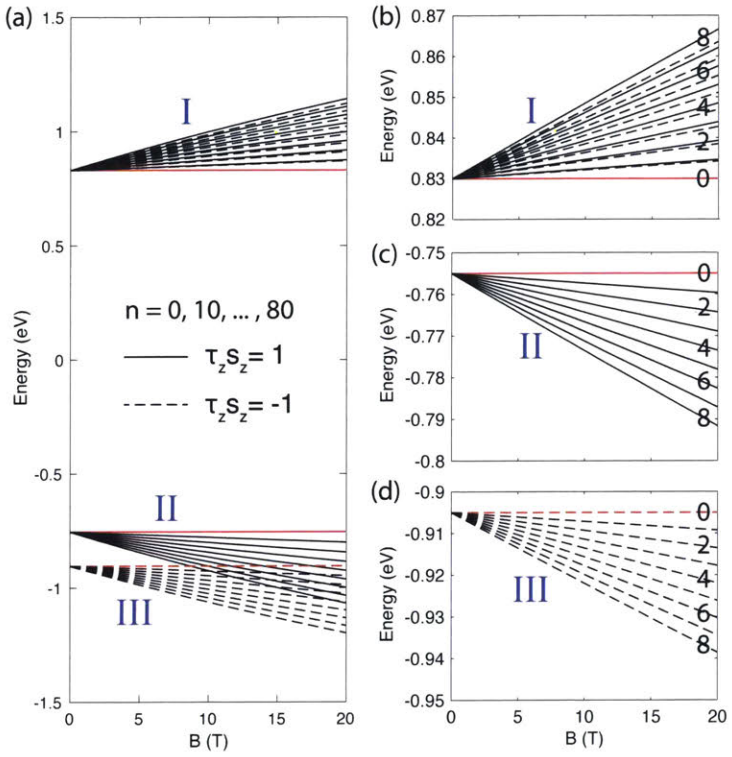

Figure 3-3: (a) Flavor-dependent LL spectrum from Eq. 3.10 with $n = 0, 10, ..., 80$ orbitals. Solid and dashed lines denote the $\tau_z s_z = 1$ and $\tau_z s_z = -1$ cases, respectively. (b)-(d) Enlarged view of the LLs in group I, II, and III in (a). The numbers denote the Landau level n. Red color in all plots denote the $n = 0$ LLs.

From Fig. 3-3 we can see that LL energies grow linearly with B, rather than $\sqrt{B}$. Besides, for $\tau_z s_z = \pm 1$, the LLs have different slopes with B. Given the fact that group II and group III LLs are shifted at $B = 0$, we expect LL crossing effects at

$$B_{cross} = \frac{4\lambda(\lambda + \Delta)}{e\hbar v^2(n_{\rm II} - n_{\rm III})} + \frac{8\lambda^2 n_{\rm III}}{e\hbar v^2(n_{\rm II} - n_{\rm III})^2} \tag{3.15}$$

Such crossings can lead to the following observations. (i) The crossing point at the $n_{\rm III} = 0$ LL has degeneracy $g = 3$, while others all have $g = 4$. (ii) LL switches from

an odd filling factor $\nu = -2(n_{\rm II} + n_{\rm III}) - 1$ to an even filling factor $\nu = -2(n_{\rm II} + n_{\rm III})$ when energy goes across $n_{\rm III} = 0$ LL. (iii) The crossing of two LLs results in increased degeneracies and lead to pronounced peaks in the measurement of longitudinal magnetoresistance. (iv) The Hall plateaus follow an unconventional sequence $\nu = ..., -2\widetilde{n}_{\rm II} - 6, -2\widetilde{n}_{\rm II} - 4, -2\widetilde{n}_{\rm II} - 2, -2\widetilde{n}_{\rm II} - 1, ..., -5, -3, -1, 0, 2, 4, ...,$ where $\widetilde{n}_{\rm II} = 4\lambda(\lambda + \Delta)/(e\hbar v^2 B)$ are solutions to $B_{cross} = B$ with $n_{\rm III} = 0$ in Eq. 3.15.

At even higher magnetic field, Zeeman splitting arising from magnetic coupling to the electron spin cannot be neglected. The LL spin degeneracy can be lifted through a Zeeman splitting $E_z = g^* \mu_B B$, with μ_B the Bohr magneton. If it is comparable to the cyclotron energy $E_c = \hbar\omega_c$, the quantum Hall state sequence changes accordingly. Several experimental studies of LLs of WSe_2 in the quantum Hall regime reveal a full lifting of the two-fold LL degeneracy at high magnetic field, and it tunes significantly with doping [102, 151, 59]. This implies strong many-body interactions, and suggests that monolayer TMDs can serve as a host for new correlated-electron phenomena.

3.2 Device fabrication

As shown in the previous section, the LLs in monolayer TMDs are predicted to be distinct from the case of two-dimensional electron gas (2DEG) in semiconductor quantum wells [130, 58] and graphene [110, 173, 107]. Due to the broken sublattice symmetry, the $n = 0$ LLs at both K and K′ valleys are split by the material's bandgap. In addition, valley-contrasting Berry curvatures associated with the conduction and valence bands in monolayer TMDs result in valley-polarized $n = 0$ LLs fixed to the conduction band minimum of the K valley and the valence band maximum of the K′ valley, if Zeeman splitting is not considered. Furthermore, strong spin–orbit interactions, which is not present in graphene, act to spin-polarize the LLs at each valley. In order to observe the unique LL spectrum in monolayer TMDs, sample quality is very important. In general, TMDs with mobilities of around $1,000$ cm^2/(V·s) or higher are required to observe the LLs at low temperature under a laboratory-scale magnetic field. Encapsulation of TMDs in between two sheets of hBN is found to achieve

highest device quality [32].

Another great challenge lies in the contact quality. Schottky barrier formed at the interface between metal and TMDs remains a persisting problem that forbids observation of quantum transport phenomena in TMD devices. Several methods have been explored to reduce contact resistance, including different choices of metal [33, 89, 31], chemical doping of the contact region [43], and graphene contacts [30, 32].

As we show below, combination of encapsulation with patterned hBN and ionic liquid gating provides the opportunity to improve device performance by independently tuning carrier density in the channel as well as in the contact region [1].

3.2.1 Ionic liquids

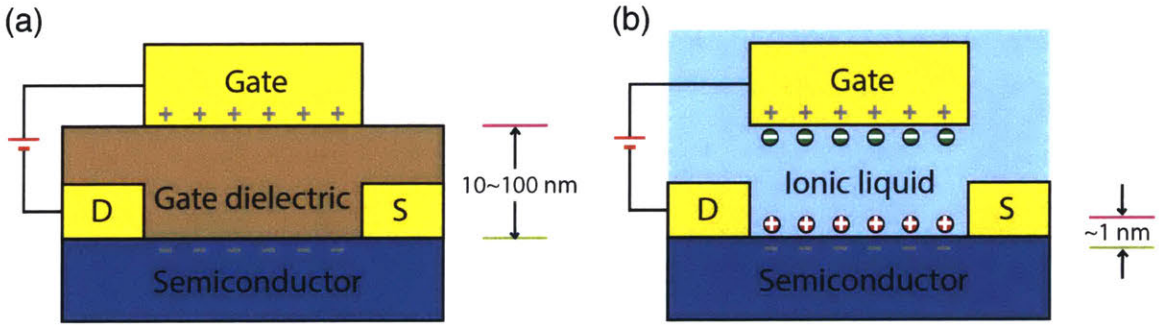

Figure 3-4: Working principle of using (a) a solid dielectric material and (b) ionic liquid or electrolyte as gate medium in a field-effect transistor (FET).

Ionic liquids (ILs) are highly polar low-melting-temperature binary salts typically comprising nitrogen-containing organic cations and inorganic anions. Because ionic liquids are composed of only ions, they show very high ionic conductivity, nonvolatility, and nonflammability. It has been demonstrated in experiments as a superior gate medium in an electric-double-layer transistor (EDLT) configuration [101, 129, 115]. The principle behind carrier doping in EDLT using ionic liquid or electrolyte compared with a solid dielectric material is illustrated in Fig. 3-4. By replacing the gate

[1] This work is done with Joel I.J. Wang, Yu-An Chen and Pablo Jarillo-Herrero, and appeared in the journal Nano Letters [147].

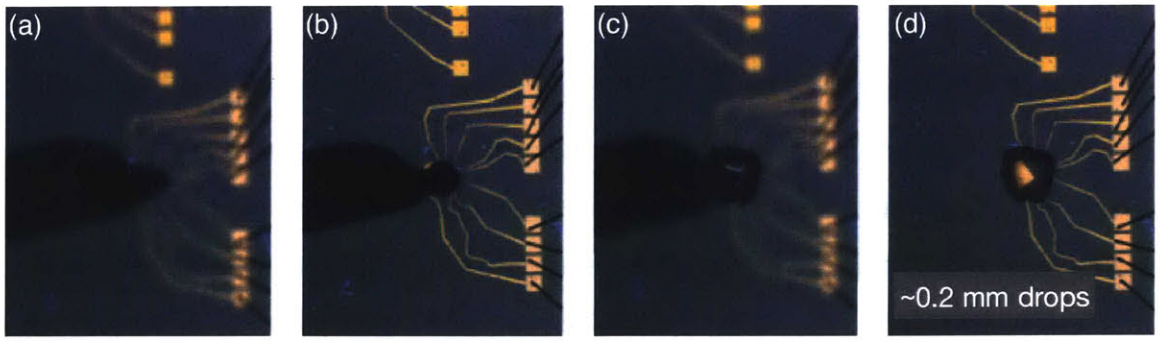

Figure 3-5: Manipulation of ionic liquids and EDLT device design. (a)-(d) A droplet of ionic liquid (DEME-TFSI) is dropped onto a patterned device using a small needle. The diameter of the droplet is ~ 0.2 mm.

dielectric material with ionic liquid or electrolyte, EDLTs enable the production of large electric fields (over 10 MV/cm) and the accumulation of extremely high carrier densities (over 10^{14} cm^{-2}). This is due to the fact that an electric double layer allow a spacing $d \sim 1$ nm formed at the surface of the EDLT and can be regarded as a parallel-plate capacitor with a nanometer-sized gap. In contrast, the conventional solid dielectric usually has thickness of about a few tens of nanometers which limits the capacitance and the capability of electrostatic carrier doping before dielectric breakdown. The ions and induced carriers right beneath form an equivalent capacitance of $\sim$10 μF/cm^2, as opposed to $\sim$12 nF/cm^2 for 285 nm SiO_2 that has been used in our previous experiments. Even with this high-κ dielectric such as HfO_2, the carrier density that could be tuned is within the order of 10^{13} cm^{-2}.

The manipulation of ionic liquid is also not so trivial. For all of the liquid gating measurements, we used the ionic liquid *N*,*N*-diethyl-*N*-(2-methoxyethyl)-*N*-methylammonium bis(trifluoromethylsulphonyl-imide) (DEME-TFSI). In Fig. 3-5 we illustrate the process of dropping a droplet ionic liquid onto the patterned gate electrode. The gate electrode is patterned with standard e-beam lithography and placed very close to the flake under study. The area of the gate electrode is usually at least 100 times larger than the flake to enable uniform electrostatic doping across the whole device. In the droplet transfer process, a small needle is attached to a controller which allows accurate control of the height of the needle under a long working distance objective. Focal plane is adjusted between the needle tip and the substrate

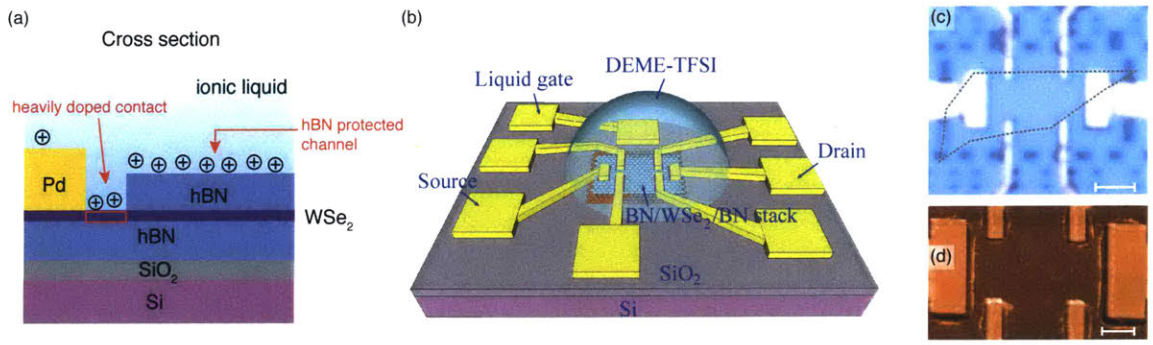

Figure 3-6: Device structures, optical and AFM images. (a) Schematic drawing of cross section view of our device. A WSe_2 flake is encapsulated between two sheets of hBN and placed on Si/SiO_2 substrate. The top hBN has windows to allow ionic liquid access to a narrow gap region where WSe_2 is exposed. Other device region is protect by hBN. (b) 3D version of schematic of device structure. (c) Optical and (d) AFM image of sample *A* reported in Sec. 3.3. The top hBN is etched with Hall bar patterns. The contact leads (Cr/Pd) are slightly smaller than the holes in the top hBN to allow ionic liquid tuning of the contact region. The scale bar of (c),(d) is 2 μm and 1 μm respectively, and the outline of the shape of WSe_2 in (c) is drawn by superposition with the optical image of $WSe2_2$ flake before pick-up.

surface alternatively to determine the distance between the two. In this way, we avoid scratching the substrate surface by the tip and raise the tip as soon as the droplet is transferred onto the substrate. In the best cases, the droplet will form a nice hemisphere sufficient to cover the whole gate electrode and our device.

Another thing that we need to be careful with is possible chemical reaction during the operation of ionic liquid gating. It is well-known that the performance of ionic liquids is very sensitive to the presence of moisture [170], which prevents the reversible and reliable operation of the devices. In order to prevent chemical reaction induced by residual water molecules, we carefully degased the ionic liquid in vacuum at 80 °C for >24 hours before dropping it onto the device and made sure all the measurements are performed under high vacuum ($< 10^{-6}$ mbar).

Although ionic liquid manifests many desirable properties compared to conventional solid-state gating, it has certain drawbacks. First, the freezing of the ion motion occurs at temperature ~200 K, which forbids modulation of carrier density under the freezing temperature. This problem can be partly overcome by introducing a conventional back-gate, which remains effective after ion freezes. However, the tuning

range will be at least an order of magnitude smaller. Second, the charged ions that accumulate above the device channel inevitably results in Coulomb scattering, which limits the carrier mobility in otherwise clean systems.

In brief, to achieve ohmic contact and low contact resistance, we would prefer that the WSe_2 near the metal contact can be heavily doped to eliminate the Schottky barrier formed between metal and TMDs. Meanwhile, in order to achieve high carrier mobility we need to protect the main device channel from undesirable Coulomb scattering due to the charged ions in ionic liquid. We also need to make sure that we are able to modulate the carrier density at low temperatures so that we can study magnetotransport in the quantum Hall regime as a function of carrier density. To fulfill all the above requirements, we designed the device structure as follows (Fig. 3-6). A WSe_2 flake is encapsulated between two sheets of hBN and placed on Si/SiO_2 substrate. The top hBN has windows to allow ionic liquid access to a narrow gap region where WSe_2 is exposed. Other device region is protected by hBN except these narrow exposed areas. Technically, this is achieved by etching the top hBN with Hall bar patterns (and we usually made an array of them with different sizes to accommodate different flake geometries, as shown in Fig. 3-7 (b)). After using it to pick up a WSe_2 and placed onto a bottom hBN, contact leads (Cr/Pd) that are slightly smaller than the holes in the top hBN is patterned to allow selective tuning of the contact region by ionic liquid. We will elaborate on the fabrication details in the next section.

3.2.2 Technique: "pick-up"

In the past, van der Waals heterostructures are built by layer-by-layer transfer technique. An illustration of this process is shown in Fig. 1-5. Crystals are exfoliated on top of transparent films such as MMA, get transferred onto a chosen target followed by removing or dissolving the film. It is repeated again and again, until the whole heterostructure is completed.

Here we report a scheme to make encapsulated devices by picking up and transferring a pre-patterned hBN 'mask'. Compared with previous method, the stack can be completed with sequential pick-up and no solvent wash is required until the whole

stack is transferred onto the final substrate. Besides, the heterostructure interface is never in direct touch with polymers, which ensures minimal residue contamination.

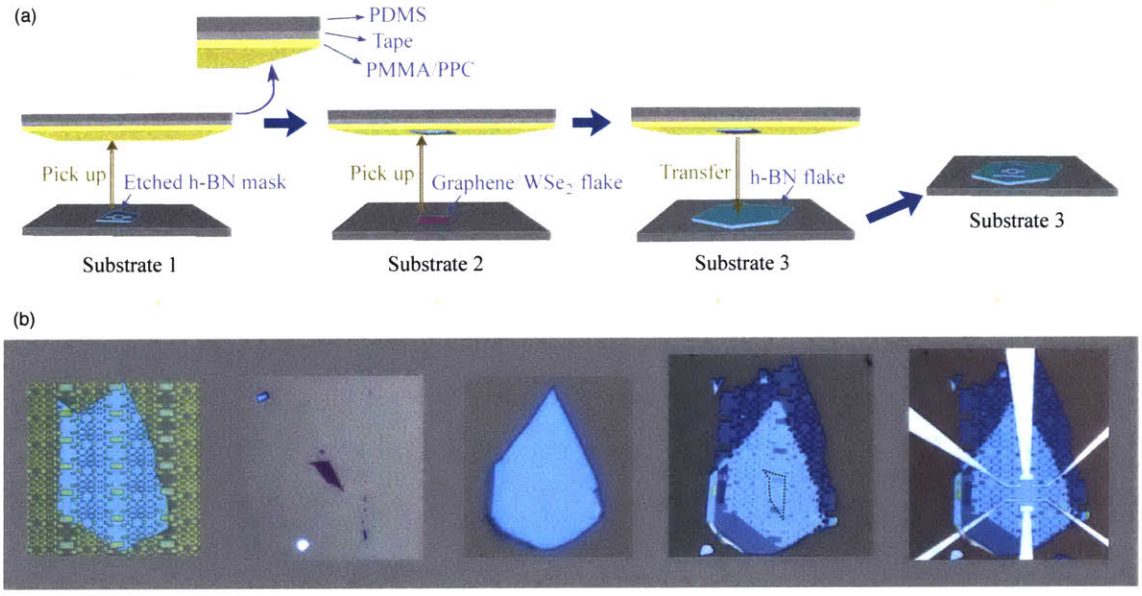

Figure 3-7: (a) Schematics of the pick-up process. (b) Optical images of the sample *A* and each separate layer components. The flakes from left to right are top hBN, a trilayer WSe_2, bottom hBN, completed stack and stack with metal contacts.

First, for the hBN mask preparation, we start with hBN exfoliation on Piranha-cleaned SiO_2 surface. Wafer with hBN flakes are then annealed in Ar/H_2 (15 sccm/15 sccm) atmosphere at 350 °C for 3 hours. Selected hBN flakes, with thickness ranges from 10 to 30 nm, are patterned with e-beam lithography using Poly(methyl methacrylate) (PMMA) thin film ($\sim$ 300 nm thick, prepared from PMMA 950, 5% in anisole, from Microchem) which serves as e-beam resist and etch mask for reactive ion etching (RIE). The hBN mask presented in this paper is etched in Ar (6 sccm), CF_4 (2 sccm), CHF_3 (50 sccm), and H_2 (30 sccm) atmosphere of 15 mtorr, power 70 watt, and the etching rate for hBN is $\sim$ 1.4 nm/s. The chip is then etched by O_2 plasma for 30 seconds in order to break cross-linked PMMA surface in order to reduce residue left on hBN mask after lift-off in acetone. The hBN masks are thus etched into a Hall bar pattern.

Next, WSe_2 (synthetic crystal from Nanosurf, Inc.) is mechanically exfoliated onto Piranha-cleaned Si/SiO_2 wafers. Transparent slides are made by spin coat-

ing polypropylene carbonate (PPC, from Sigma Aldrich, 15% concentration dissolved in anisole) onto a glass slide with PDMS covered in clear packing tape. The role of the tape is to improve the adhesion of spin-coated PPC on the slide. The PDMS/tape/PPC stack is then baked at 100 °C for 15 min, cut into small squares ($\sim$ 2 mm by 2 mm), and placed onto glass microscope slides. The PPC pick-up process is similar to PMMA pick-up, with slight difference in temperature. It requires 30 °C for about 3 min after bringing the polymer into contact with the targeted chip, followed by an abrupt disengage by lowering the stage. When using the same method to pick up the next flake, we make sure the Hall bar pattern of the hBN is well aligned to the WSe_2 flake. For the last transfer step, we press the slide with hBN and WSe_2 stack onto another hBN flake, which is exfoliated onto O_2 plasma cleaned Si/SiO_2 chip (150 W for 120 s). To release the PPC, the substrate is heated to 80 °C and then cooled down to room temperature before slowly raising the glass slide. In this way, the stack of flakes is transferred onto the substrate along with the PPC polymer, which is subsequently dissolved in chloroform (5 min) and acetone (5 min). It is illustrated in Fig. 3-7. In this "pick-up" process, the flake encapsulated does not have direct contact with any polymer films or solvent, which insures minimal contamination.

Finally, device contacts are patterned by standard e-beam lithography techniques in a Hall bar geometry. It is then contacted with Cr/Pd (0.7/100 nm) by e-beam evaporation. Then the ionic liquid (DEME-TFSI) is used to further improve the quality of the contact. When designing contacts to the device, the contact metal is patterned slightly smaller than the patterned openings in the top hBN flake (see AFM image of the device in Fig. 3-6 (d)), so the WSe_2 near the contact region is exposed to allow ionic liquid gating. A side-gate electrode for the ionic liquid is patterned near the flake, with an area at least 100 times larger than the WSe_2 flake. After the device fabrication is completed, a droplet of DEME-TFSI is placed on the center of the device with a needle tip to cover both the flake and liquid gate electrode. Fig. 3-6 (a),(b) shows a schematic image of the device geometry. With this method, the ionic liquid only affects the carrier density of the contact region, while the main channel of the device is sealed by the hBN mask and remains largely unaffected.

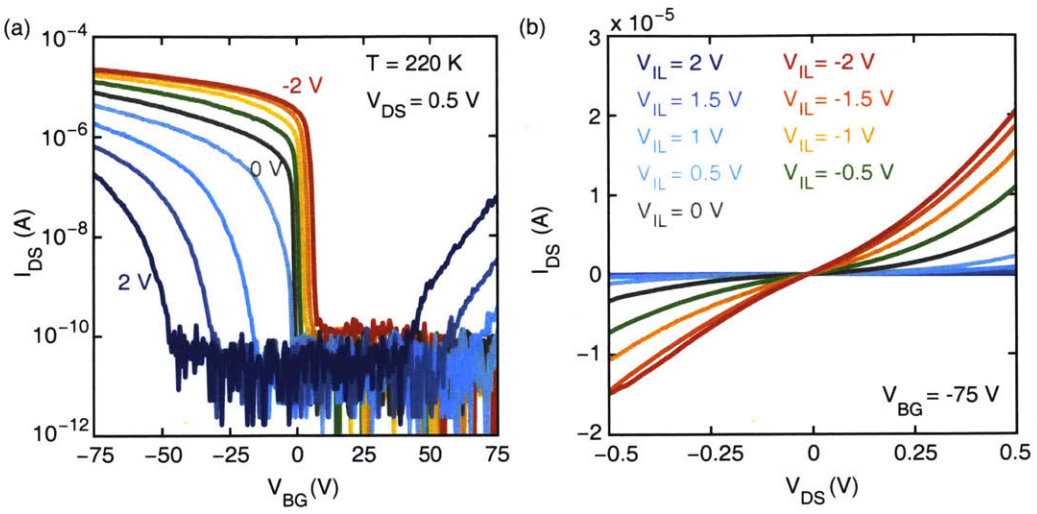

Figure 3-8: I_{DS} as a function of V_{BG} measured at different ionic liquid gate voltages: V_{IL} = 2, 1.5, 1, 0.5, 0, -0.5, -1, -1.5, -2 V. V_{DS} = 0.5 V. (b) I_{DS} as a function of V_{DS} for the same set of V_{IL}, with fixed V_{BG} = -75 V. The temperature for all measurements was 220 K.

3.3 Experimental results

In this section, we show transport properties based on two devices. Sample A is a trilayer WSe_2 and sample B is a 4-layer WSe_2.

3.3.1 Properties above freezing temperature of ionic liquid

Here we fabricated a trilayer WSe_2 device (sample A) encapsulated by two hBN flakes (thickness of top and bottom hBN are 35 nm and 25 nm respectively) using the technique mentioned above. The WSe_2 is contacted with Cr/Pd (0.7/100 nm) by e-beam evaporation. In addition to the hBN encapsulation introduced previously, the ionic liquid (DEME-TFSI) is used to further improve the quality of the contact.

Fig. 3-8 shows the source-drain current through this device for different ionic liquid gate settings. As shown in Fig. 3-8 (a), by changing the ionic liquid gate voltage V_{IL} from 2 V to -2 V, while sweeping the back-gate voltage, the device changes from balanced, ambipolar transistor behavior to strong p-type conduction, which indicates the enhancement of p-type contact when applying a favorable negative ionic liquid

gate voltage. This effect is also shown in the I-V curves with different ionic liquid gate voltages at fixed V_{BG} = -75 V (see Fig. 3-8 (b)). Compared to $V_{IL} = 0$, the linearity of I-V curve at V_{IL} = -2 V is greatly improved. This nearly ohmic contact rendered by high negative V_{IL} enables four-terminal resistivity and Hall measurements to extract contact resistance, intrinsic conductivity, and Hall mobility of this device. We note that all the measurements are done at a temperature $\sim$ 220 K, which is slightly above the freezing temperature of the liquid ($\sim$ 200 K) [164] to minimize chemical reactions between the ionic liquid and contact leads.

Based on four-terminal measurements, the contact resistance, R_c, is extracted from the resistivity as $R_c = V_{ds}/I_{ds} - \rho \cdot l/w$, where l and w are the full sample length and width, respectively, and $\rho = (V_{xx}/I_{ds})/(l_{in}/w)$, with l_{in} the length between the inner contacts, as shown in Fig. 3-9 (a). From V_{IL} = 0 V to -2 V, the contact resistance for V_{BG} = -75 V decreases by nearly a factor of 4, changing from 57 kΩ to 15 kΩ, which demonstrates the tunability of the contact resistance by the ionic liquid. We also plot conductivity as a function of V_{BG}, for different V_{IL}, in Fig. 3-9 (b). The conductivity reaches a maximum of 0.34 mS at V_{BG} = -75 V. Comparing different V_{IL}, the conductivity follows almost the same trace except for a small shift in threshold voltage. This confirms the transparency of the contacts and allows us to extract the intrinsic transport properties of the device.

The small change in conductivity for different V_{IL} also demonstrates that the device geometry introduced here allows independent tunability of the channel conductance and contact resistance. The ionic liquid gate only significantly influences the contact region, while the back gate controls the intrinsic conductivity of the device channel. When the ionic liquid is directly in contact with the semiconductor, the ions in the liquid and the free carriers in the semiconductor beneath the liquid form an equivalent capacitor with c $\sim$ 12 μF/cm^2 [112, 141, 165, 164], which is $\sim$1000 times larger than for conventional dielectric gating with 300 nm thick SiO_2. In contrast, the relatively small shift of intrinsic conductivity corresponds to a capacitance of a top gate through a conventional dielectric. This smaller capacitance additionally rules out the possibility that ionic liquid penetrates below the top hBN mask.

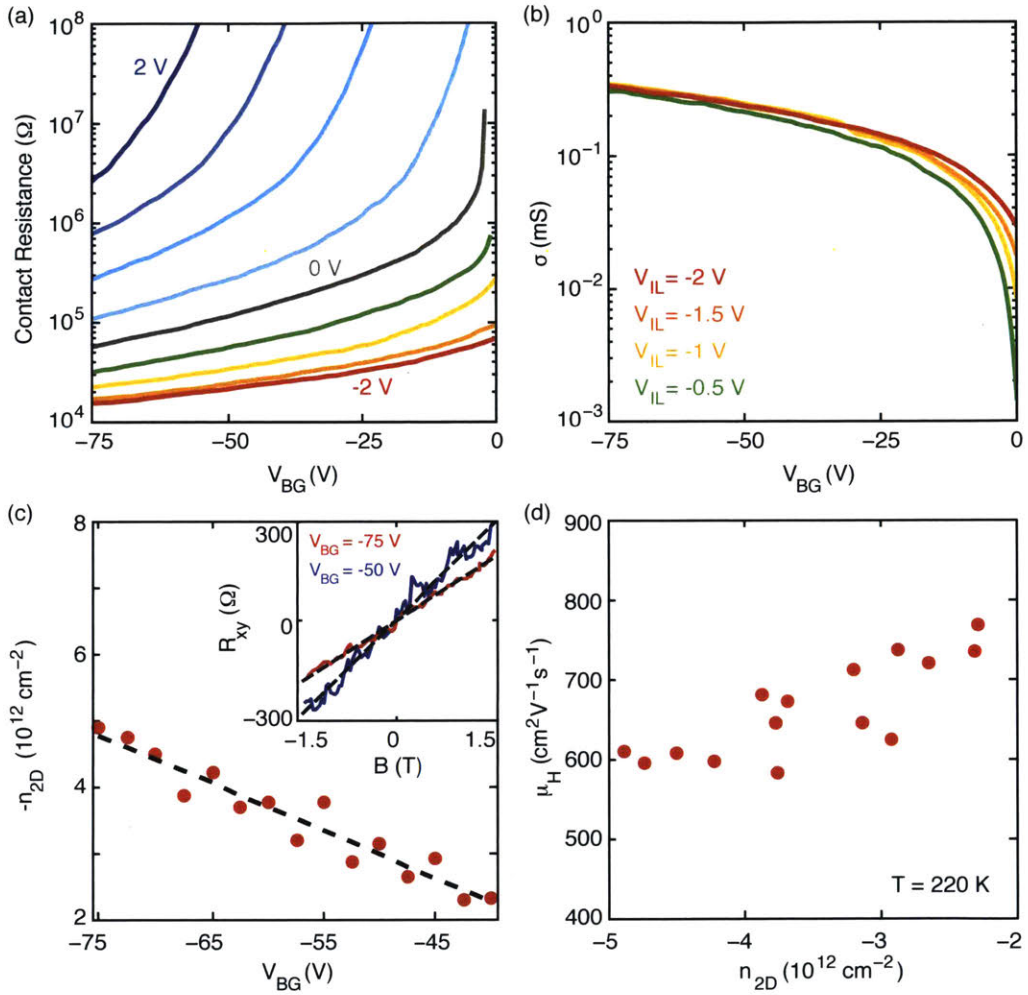

Figure 3-9: (a) Contact resistance as a function of V_{BG} of the WSe_2 device at different V_{IL} (denoted with the same set of colors as Fig. 3-8). (b) Conductivity of the device as a function of V_{BG}, extracted from four-probe measurements with different ionic liquid gate voltage V_{IL} = -2 V to -0.5 V, while V_{DS} = 0.5 V. (c) Carrier density calculated from Hall measurements as a function of V_{BG}. The nearly linear dependence of n_{2D} on V_{BG} corresponds to a capacitance per unit area of $c = 12$ nF/cm^2. Inset: selected Hall resistance vs. magnetic field with V_{BG} = -75 V, - 50 V. (d) Hall mobility calculated by $\mu_H = \sigma/(ne)$ is plotted against carrier density. V_{IL} = -2 V and the temperature is ~220 K.

The Hall effect is used to determine carrier density, n, and mobility, μ_{H} as a function of V_{BG}. At 220 K we simultaneously measure V_{xx}, V_{xy} and I_{DS} with an AC current bias of 0.5 μA. For the Hall measurement, the ionic liquid gate is set to -2 V to ensure the best p-type contact. The inset of Fig. 3-9 (c) shows $R_{xy} = V_{xy}/I_{DS}$ as a function of magnetic field at two selected back-gate voltages. The slope of the linear fit is equal to $1/(n_{2\mathrm{D}}e)$, where $n_{2\mathrm{D}}$ is the carrier density, and e is the elementary charge. We combine measurements of carrier density and conductivity as a function of back-gate voltage to obtain the Hall mobility at different carrier densities. The nearly linear dependence of $n_{2\mathrm{D}}$ on V_{BG} corresponds to a capacitance per unit area $c = 12$ nF/cm^2. This value is in rough agreement with the capacitance expected for a parallel plate geometry with the bottom dielectric, 11.2 nF/cm^2 (25 nm thick hBN on top of 285 nm SiO_2), without taking into account the complexity of the device structure and possible influence from the top hBN and ionic liquid.

The Hall mobility extracted as a function of carrier density is plotted in Fig. 3-9 (d), and $\mu_H > 600$ cm^2/(V $\cdot$ s) is observed over a range of back-gate voltage, -75 to -40 V. For comparison, we also calculate the average field effect mobility from the conductivity in Fig. 3-9 (b), assuming $c = 12$ nF/cm^2 for the same range of back-gate voltages (-75 V to -40 V). We obtain $\mu_{FE} = 600 \pm 80$ cm^2/(V $\cdot$ s), in good agreement with the measured μ_H. For bulk WSe_2, hole mobility as high as ~ 500 cm^2/(V $\cdot$ s) was measured,[116] and recent work on monolayer WSe_2 FETs reported 2-probe field-effect hole mobility up to ~ 250 cm^2/(V $\cdot$ s) at room temperature [43]. In addition, at 77 K ionic liquid-gated graphene contacts to few-layer WSe_2 revealed Hall mobility up to ~ 330 cm^2/(V $\cdot$ s) [30]. For hBN-encapsulated MoS_2, recent work shows mobilities in the range of 100-300 cm^2/(V $\cdot$ s) at 200 K for 1- to 6-layer thick MoS_2 [32]. The relatively high Hall mobility of the devices presented here supports our claim that encapsulation in hBN improves the performance of TMD devices, with the help of ionic liquid gating that significantly improves the contact quality. This result highlights the potential for observing novel quantum transport phenomena in WSe_2 [85]. Another merit of this geometry is that the hBN acts as a barrier to the disordered charges in ionic liquid and possible chemical reactions induced on the device surface

during operation, which may also contribute to the improved mobility, similar to a previous report on hBN covered strontium titanate (STO) samples [49].

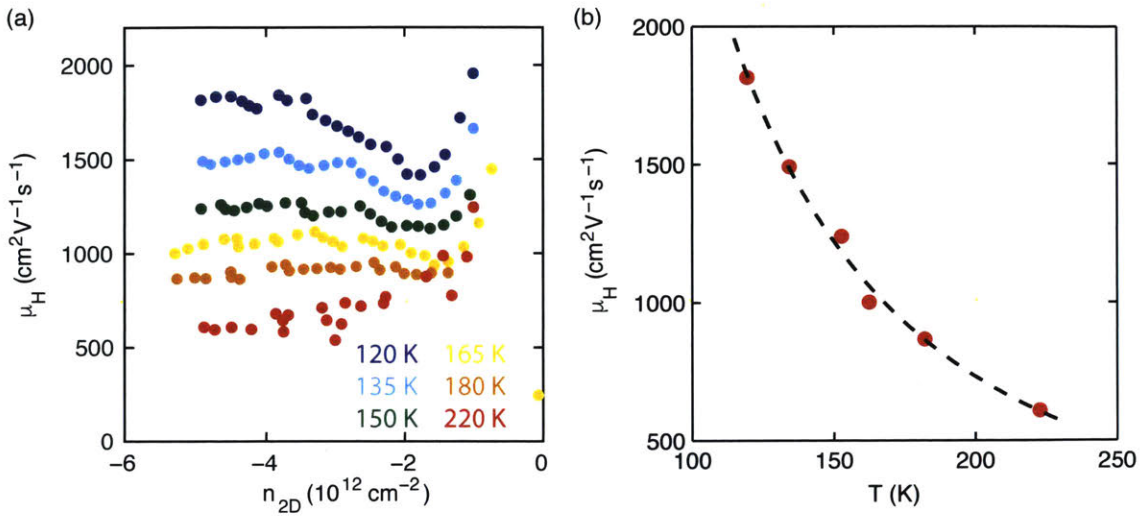

Figure 3-10: Sample A: (a) Hall mobilities as a function of carrier density at different temperatures, as denoted by different colors. (b) Hall mobility as a function of temperature with V_{BG} fixed at -75 V.

3.3.2 Towards higher mobility at low temperatures

We then perform Hall effect measurement when temperature is further lowered below the freezing temperature of ionic liquids. During the cooling process, the ionic liquid gate is fixed at $V_{IL} = -3$ V. We observe that both conductivity σ and Hall mobility μ_H increases as temperature decreases. We plot Hall mobility as a function carrier density and temperature in Fig. 3-10. In the observed temperature range, Hall mobility approximately follows a power law in temperature, $\mu_H \propto T^{-\gamma}$, with $\gamma = 1.78$. It is expected that MoS_2 devices with mobilities limited by homopolar, optical phonons should follow this form in this temperature range, with $\gamma = 1.69$ for monolayer and $\gamma = 2.6$ for bulk MoS_2 [66, 46]. The value of γ agrees well with the prediction, though we note that the fit was obtained over a limited temperature range. Hall mobility reaches ~ 1800 $cm^2/(V \cdot s)$ at 120 K.

We also did the same type of measurement on a 4-layer sample (sample B). A 4-layer WSe_2 is encapsulated in between two sheets of hBN (thickness of top and

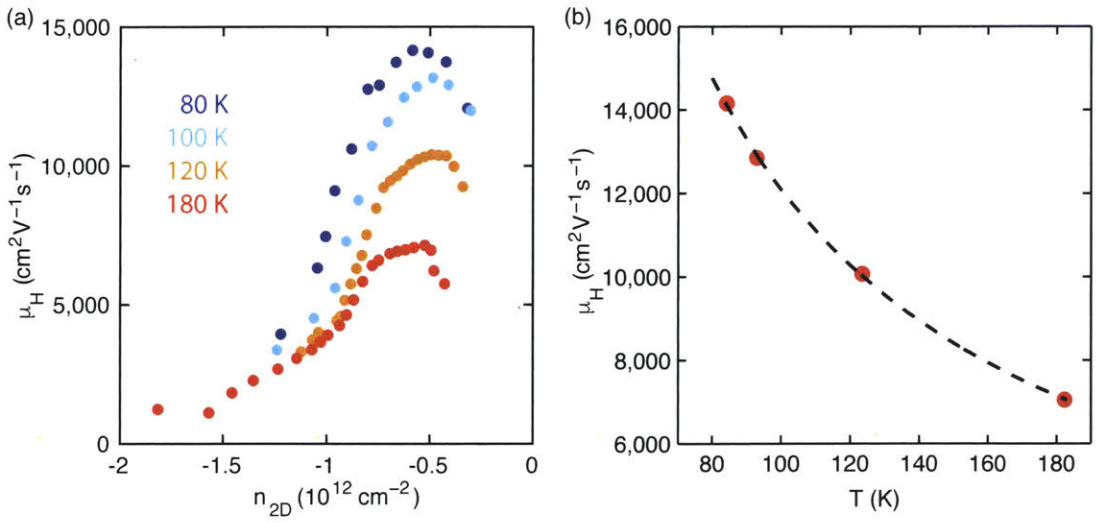

Figure 3-11: Sample B: (a) Hall mobilities as a function of carrier density at different temperatures, as denoted by different colors. (b) Hall mobility as a function of temperature with V_{BG} fixed at -35 V, at which the Hall mobility reaches maximum value.

bottom hBN are 16 nm and 20 nm respectively). We also add a layer of e-beam resist (ZEP) mask covering the metal contact region to protect it from chemical reactions with ionic liquid. The result is shown in Fig. 3-11. The device is cooled down with $V_{IL} = -3$ V. The mobility is highly dependent on carrier density and reaches as high as $\sim 14,000$ cm^2/(V $\cdot$ s) at 80 K. At fixed back-gate voltage ($V_{BG} = -35$ V), Hall mobility approximately follows a power law in temperature, $\mu_H \propto T^{-0.9}$. This is much smaller than the predicted values for TMDs, whose origin still remains elusive.

The high mobility and low contact resistance achieved in our samples manifest tremendous potentials for studying novel transport phenomena in quantum Hall regime. However, neither devices survived below 80 K. We suspect that ionic liquid moves or cracks during the cooling process, which destroyed our samples. A slower cool down or extra protective layer between contacts and ionic liquid might be helpful to eliminate such problem.

3.3.3 Conclusion

We have presented a fabrication scheme to pick-up and transfer pre-patterned hBN mask as a core technique to create 2D van der Waals heterostructures. The hBN can be patterned into arbitrary shapes to fit the needs of various experiments at the mesoscopic scale, and the robustness of this method allows multiple pick-ups and transfers required to fabrication complex heterostructures. The dry fabrication procedure maintains pristine 2D materials in multiple stacks without thermal annealing, so it can be applied to thermally sensitive materials while greatly reducing the amount of time to fabricate heterostructures. Both devices presented here demonstrate a high level of cleanliness and high mobility. Independent gating of the contact region by ionic liquid demonstrated here also provides a solution to the persistent contact difficulty of TMD devices. Enabled by this technique, we also report the highest Hall mobility to date in a few-layer WSe_2 device.

Chapter 4

Enhanced Superconductivity in 2H-TaS_2 in the 2D Limit

Layered transition metal dichalcogenides 2H-MX_2 (where M = Nb, Ta and X = S, Se) that host coexisting charge-density wave (CDW) and superconducting orders provide ideal systems for exploring effects of dimensionality on correlated electronic phases. Dimensionality has profound effects on both superconductivity and CDW instabilities. On one hand, reduced dimensionality induces localization of Cooper pairs by disorder, typically suppressing superconductivity; while Peierls instabilities and electron-phonon interactions are strengthened in reduced dimensions, favoring stronger CDW order. On the other hand, stronger fluctuation effects in lower dimensions tend to destroy long-range order in both cases. Here we report two unusual trends, a substantial enhancement of superconducting T_c and a suppression of the CDW transition in 2H-TaS_2 in the 2D limit [1]. Remarkably, in the monolayer limit, T_c increases to 3.4 K compared to 0.8 K in the bulk. To unveil the possible relationship of these trends, we perform electronic structure calculations showing that a reduction of the CDW amplitude results in a substantial increase of the density of states at the Fermi energy, which explains the trend in T_c and captures the correct magnitude of enhancement. Our results establish ultra-thin 2H-TaS_2 as an ideal platform to study

[1] This work is done with Shiang Fang, Valla Fatemi, Jonathan Ruhman, Efrén Navarro-Moratalla, Efthimios Kaxiras and Pablo Jarillo-Herrero, and appeared in the journal Physical Review B [162].

	2H-$TaSe_2$	2H-TaS_2	2H-$NbSe_2$	2H-NbS_2
T_{SC} (K)	0.15	0.8	7.3	6.1
T_{CDW} (K)	120	70	35	<4

Table 4.1: Phase transition temperatures for 2H-MX_2 from Ref. [153]

the competition between CDW order and superconductivity down to the monolayer limit, providing insight towards understanding correlated electronic phases in reduced dimensions. A related work can be found in Ref. [12].

4.1 Phase transitions in group-VII Dichalcogenides

4.1.1 Overview

Transition metal dichalcogenides (TMDs) 2H-MX_2 (where M = Nb, Ta and X = S, Se) have attracted considerable attention as novel 2D crystalline superconductors [125]. In these materials, superconductivity (SC) occurs in an environment of pre-existing charge-density wave (CDW) order [106, 71], making them an ideal platform to study many-body ground states and competing phases in the 2D limit. In bulk crystals, the reported critical temperature of the CDW transition decreases from 120 K in 2H-$TaSe_2$ down to 30 K in 2H-$NbSe_2$. Superconductivity weakens in approximately reverse order, with T_c increasing from around 0.2 K in 2H-$TaSe_2$ to 7.2 K in 2H-$NbSe_2$. The relationship between CDW and superconductivity in such systems is still under debate [20, 50]. It is generally believed that their mutual interaction is competitive, but evidence to the contrary, indicating a cooperative interaction, has also been reported in angle-resolved photoemission spectroscopy (ARPES) studies [71].

In TMDs, superconductivity and CDW instability can be investigated by adjusting the interlayer interactions through pressure [48, 29] or molecule intercalation [136, 153]. Recently, mechanical exfoliation has emerged as a robust method for producing ultra-clean, highly crystalline samples with atomic thickness [52]. This offers a useful way to assess the effect of dimensionality and interlayer interactions on both su-

perconductivity and CDW. A material whose behavior as a function of layer thickness has been recently studied is $NbSe_2$ [25, 156, 140, 70], in which the superconducting state is progressively weakened in samples thinner than 5 layers, with T_c lowered from 7.2 K in bulk crystals to 3 K in the monolayer. The thickness dependence of CDW order is still under debate, with different results from Raman and scanning tunneling microscopy/spectroscopy (STM/STS) studies [157, 142].

Bulk 2H-TaS_2, another member of the 2H-MX_2 family, exhibits a CDW transition at 70 K and a SC transition at 0.8 K [103, 106, 56, 105]. Compared to $NbSe_2$, TaS_2 manifests a stronger signature of the CDW transition in transport in the form of a sharp decrease of resistivity [153], and thus serves as a desirable platform to study the thickness dependence of the CDW instability. STM/STS measurements on monolayer TaS_2 epitaxially grown on Au(111) substrates show suppression of the CDW instability [126]. Regarding superconductivity, an enhanced T_c down to a thickness of 3.5 nm (5L) was recently reported, utilizing TaS_2 flakes directly exfoliated on a Si/SiO_2 substrate [105]. Considering the fact that appreciable decrease of T_c in $NbSe_2$ only occurs in samples thinner than 5 layers, it would be interesting to explore the trend of T_c in TaS_2 towards the exact 2D limit. Prior work found that samples thinner than 5L become insulating, indicative of its particular susceptibility to degradation in ambient atmosphere. Therefore, exfoliation and encapsulation in an inert atmosphere become crucial in order to obtain high quality samples.

This chapter is arranged as follows: in Section 4.2, we report electronic transport studies of the properties of mono- and few-layer 2H-TaS_2 at different temperatures and magnetic fields. We show that superconductivity persists in TaS_2 down to the monolayer limit, with a pronounced increase in T_c from 0.8 K in bulk crystals to 3.4 K in the monolayer. At higher temperatures, two electronic transport signatures of the CDW transition are found to vanish in ultra-thin samples: (1) a kink in the temperature dependence of the resistivity, and (2) a change of sign in the Hall coefficient versus temperature. In Section 4.3, we report calculations on the electronic and vibrational properties to explore the competition between SC and CDW in this material. We found that suppression of the CDW order leads to a substantial increase

in the density of states at the Fermi level, which ultimately enhances T_c. We also revisit the impact of quantum fluctuations of the CDW order on the enhancement of T_c. Our study provides insights into the importance of reduced dimensions on many-body ground states and their interactions.

4.1.2 2D superconductors: from BCS to BKT model

According to the theory of Bardeen, Cooper and Schrieffer (BCS) [11, 10] of superconductivity, the system can be described by a coherent macroscopic wave function

$$|\,\psi_{\rm BCS}\,\rangle = \prod_k (U_k + V_k C^\dagger_{\uparrow,k} C^\dagger_{\downarrow,k}\,|\,0\,\rangle\,)$$

where $C^\dagger_{\uparrow,k}(C^\dagger_{\downarrow,k})$ are the creation operators of electrons with momentum k and spin up(down), and U_k, V_k are the corresponding complex coefficient. The two electrons with opposite spins and the same momentum are paired by phonons and form Cooper pairs, which conduct charges in the superconducting current.

In the 2D limit where phase fluctuations are relevant, a different phase transition mechanism comes to light, which is known as Berezinskii-Kosterlitz-Thouless (BKT) transition [74]. In BKT theory, when the temperature drops below the BCS mean-field transition temperature T_c, a loss of global phase coherence and dissipation due to a finite flux resistance occur with thermally excited vortices. In this regime, a finite supercurrent can flow below the BKT transition temperature $T_{\rm BKT}$, as a consequence of formation of bound vortex-antivortex pairs.

To illustrate what is BKT transition, we start with a 2D XY-model. The model consists of planar rotors of unit length, which can be viewed as superconducting order parameter in the SC model. For simplicity, we assume that it is arranged on a 2D square lattice. The Hamiltonian of the system is given by

$$H = -J \sum_{\langle i,j \rangle} \mathbf{S}_i \cdot \mathbf{S}_j = -J \sum_{\langle i,j \rangle} \cos(\theta_i - \theta_j) \tag{4.1}$$

Here $\langle i,j \rangle$ denotes summation over all nearest neighbor sites in the lattice, and θ_i

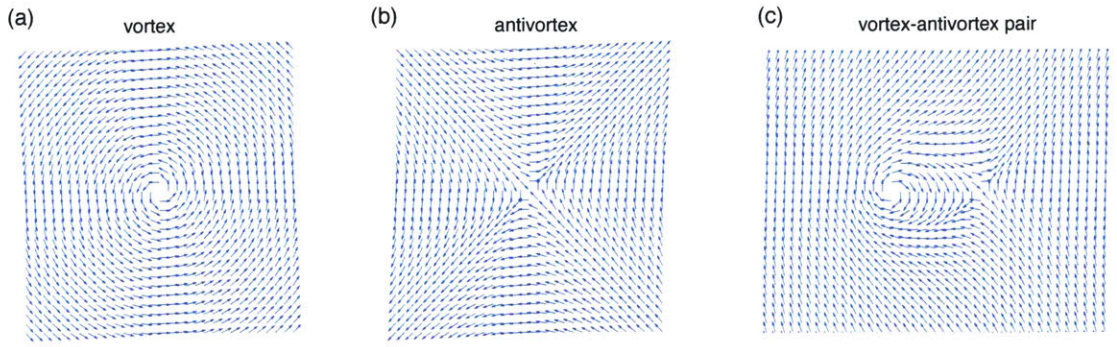

Figure 4-1: Illustration of phase field for (a) a vortex, (b) an antivortex and (c) a vortex-antivortex pair. It is seen that a bound vortex-antivortex pair has net vorticity of zero, which doesn't affect long range correlations. Conversely, unbound vortices screen long range correlations.

denotes the angle of the rotor on site i with respect to some (arbitrary) polar direction. In the continuum regime, the Hamiltonian can be written as

$$H = E_0 + \frac{J}{2}\int \mathrm{d}\mathbf{r}(\nabla\theta)^2 \tag{4.2}$$

Here $E_0 = 2NJ$ is the energy of the completely aligned ground state of N rotors.

The thermodynamics of the system is obtained from the partition function

$$Z = e^{-\beta E_0}\int D[\theta]\exp\left\{-\beta\frac{J}{2}\int \mathrm{d}\mathbf{r}(\nabla\theta)^2\right\} \tag{4.3}$$

a functional integral over all possible configurations of the director field $\theta(\mathbf{r})$. The field configurations corresponding to local minima of H and here are two types of solutions.

$$\frac{\delta H}{\delta\theta(\mathbf{r})} = 0 \Rightarrow \nabla^2\theta(\mathbf{r}) = 0 \tag{4.4}$$

The first consists of the ground state $\theta(\mathbf{r}) =$ constant. The second type of solutions consist of vortices in the director field. For the second type, assuming for all closed path encircling the centre of the vortex r_0 satisfy

$$\oint \nabla\theta(\mathbf{r})\cdot \mathrm{d}\mathbf{l} = 2n\pi \tag{4.5}$$

we can estimate the energy of a vortex E_{vor} assuming $2n\pi = 2\pi r|\nabla\theta|$

$$E_{vor} - E_0 = \frac{J}{2}\int \mathrm{d}\mathbf{r}[\nabla\theta(\mathbf{r})]^2 \tag{4.6}$$

$$= \frac{J}{2}\int_0^{2\pi}\int_a^L (\frac{n}{r})^2 r\mathrm{d}r \tag{4.7}$$

$$= n^2\pi J \ln\left(\frac{L}{a}\right) \tag{4.8}$$

where a is the lattice spacing and L is the finite system size. In a vortex, $|\nabla\theta|$ decays only as $1/r$ leading to a logarithmic divergence of the energy. We can estimate the Helmholtz free energy of a single vortex $F = E - TS$. Here the entropy can be estimated by the number of places where we can position the vortex centre, i.e., $S = k_B \ln(L^2/a^2)$. Then the Helmholtz free energy is given by

$$F = E_0 + (\pi J - 2k_B T)\ln\left(\frac{L}{a}\right) \tag{4.9}$$

At temperatures $T > \pi J/2k_B$ the system can lower its free energy by producing vortices. This simple heuristic argument illustrates that the logarithmic dependence on system size of the vortex energy as well as the entropy produce the vortex unbinding transition at temperature T_{BKT}. The value of T_{BKT} differ from one system to another. In the 2D XY-model $T_{\mathrm{BKT}}/J \simeq 0.893 \pm 0.002$ [113].

In reality it is not single vortices of the same sign that is generated at a certain temperature. Fig. 4-1 (a) and (b) show an example of a vortex and an antivortex. What happens is that the vortex and antivortex are bound together for temperatures below T_{BKT}. If we consider a pair of single charged vortex and an anti-vortex, the energy is given by

$$E_{2vor} = 2E_c + E_1 \ln\left(\frac{R}{a}\right) \tag{4.10}$$

where R is the separation between the vortex and the anti-vortex, E_c is the energy of the vortex cores and E_1 is proportional to J.

When vortex-antivortex pair is bound, long range order is restored due to net vorticity of zero, as shown in Fig. 4-1. Experimentally, T_{BKT} can be determined by

analyzing the I-V characteristic curves at various temperatures, expected to manifest a universal relation $V \propto I^3$ when vortex-antivortex pairs dissociate.

4.1.3 McMillan's formalism

In theory of strong-coupling superconductors, the Cooper pairs and quasiparticles have a finite lifetime due to strong e-ph coupling. According to the BCS theory of weak-coupling superconductivity, one has a relation between the transition temperature T_c, a typical phonon energy called Debye frequency ω_D, and the interaction strength $N(0)V$

$$T_c = \hbar\omega_D \exp[-1/N(0)V] \tag{4.11}$$

where $N(0) = \mathrm{DOS}(E_F)$ the density of states at the Fermi surface and V is the pairing potential arising from the electron-phonon interaction.

According to McMillan's theory [100], which incorporates empirical values of the coupling constants and the "band-structure" density of states for a number of metals and alloys, in the strong-coupling regime, the critical temperature is expressed by

$$T_c = \frac{\Theta_D}{1.45} \exp\left[-\frac{1.04(1+\lambda)}{\lambda - \mu^*(1+0.62\lambda)}\right], \tag{4.12}$$

where μ^* is the Coulomb pseudopotential of Morel and Anderson given by

$$\mu^* = \frac{\mathrm{DOS}(E_F)\langle V_c\rangle}{1 + \mathrm{DOS}(E_F)\langle V_c\rangle \ln\left(\frac{E_B}{\omega_0}\right)}, \tag{4.13}$$

and λ is the electron-phonon coupling constant

$$\lambda = \mathrm{DOS}(E_F)\langle I^2\rangle / M\langle\omega^2\rangle. \tag{4.14}$$

with $\mathrm{DOS}(E_F)$ the density of states, V_c the matrix element of the screened Coulomb interaction, E_B the electronic band width, ω (ω_0) the (maximum) phonon frequency, I the electron-phonon matrix elements, M the atom mass, and $\langle \ldots \rangle$ the average over the Fermi surface. As one can see, when $\lambda \ll 1$, which indicates a weak-coupling

regime, the critical temperature reduces to a BCS expression

$$T_c = \hbar\omega_D \exp[-1/(\lambda - \mu^*)] \tag{4.15}$$

with $\lambda - \mu^* = N(0)V$.

In 2H-TaS_2, assuming $\mu^* = 0.15$ as suggested by McMillan, one can evaluate the inverted form of the above equation and obtain $\lambda = 0.482$ for TaS_2 by assuming $\Theta_D = 250$ K [127] and $T_c = 0.8$ K [105], indicating that TaS_2 lies in the intermediate coupling regime. In this regime, the McMillan's formalism can be applied to estimate the critical transition temperature of the material.

4.2 Experimental results

4.2.1 Device fabrication

We exfoliate and fabricate samples with a transfer set-up built inside a glove box filled with Argon gas, and encapsulate the TaS_2 flake between two sheets of hexagonal boron nitride (hBN). We build our devices utilizing a improved version of polymer pick-up technique [147] as illustrated in Fig. 4-2(a), taking advantage of the van der Waals adhesion between 2D layers. Using this technique, hBN and TaS_2 flakes are picked up in sequence and transferred onto pre-evaporated bottom contacts embedded in another hBN flake. The details are as follows.

The sample fabrication process takes place in a glove box filled with Argon gas. TaS_2 crystals (from HQgraphene) are exfoliated onto Si/SiO_2 wafers inside the glove-box. hBN flakes that support bottom contacts are exfoliated onto Si/SiO_2 wafers. Wafers with hBN flakes are then annealed in Ar/H_2 atmosphere at 350 °C for 3-5 hours. Selected hBN flakes, with thickness ranging from 20 to 30 nm, are patterned with e-beam lithography using MMA/ZEP followed by XeF_2 gas etch for 20 s $\times$ 5 cycles. Then Cr/Pd 2/25 nm is evaporated by thermal or e-beam deposition. In this way, bottom contacts that are embeded in hBN are fabricated. Using a slide consisting of a Poly(Bisphenol A carbonate) film held on top of a piece of polydimethylsiloxane

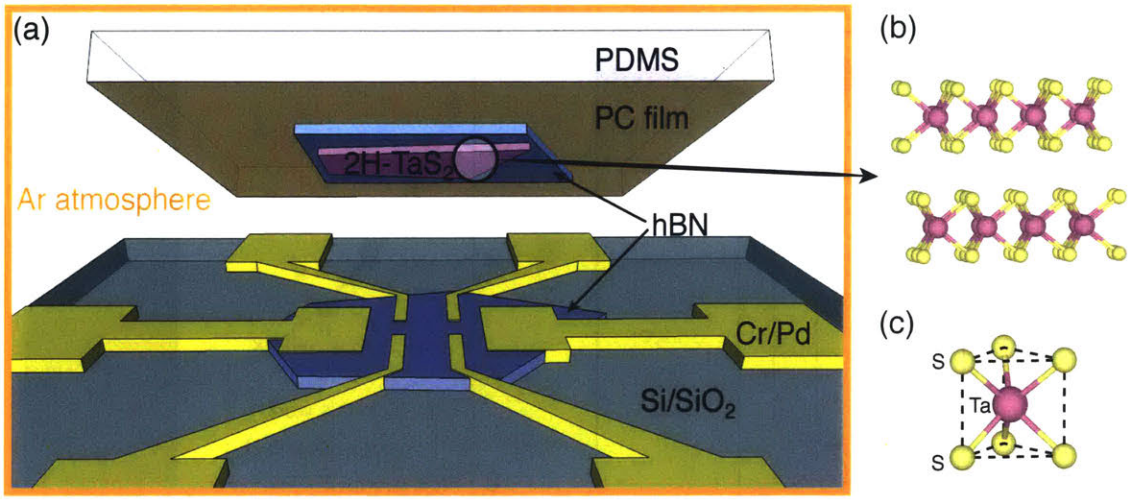

Figure 4-2: Device fabrication of atomically thin TaS_2 samples. (a) Schematic of fabrication of TaS_2 devices using a polymer pick-up technique. (b) Crystal structure of 2H-TaS_2 from side view. (c) Unit cell of 1H-TaS_2.

(PDMS) elastomer, hBN and TaS_2 flakes can be picked up in sequence and transferred onto the bottom contacts. Such encapsulation allows for a van der Waals seal between two hBN flakes and therefore prohibits exposure to air during the sample transportation outside the glove box.

With this method, we minimize the exposure to ambient atmosphere during the device fabrication process, which makes it possible to produce high quality TaS_2 samples as thin as monolayer in our experiment.

4.2.2 Enhanced superconductivity in the monolayer limit

As seen in Fig. 4-3(a), when the temperature is sufficiently low, a clear superconducting transition is observed for 1, 2, 3, 5, 7-layer, and bulk samples. By fitting the resistance to the Aslamazov-Larkin expression [6], we are able to determine the mean-field superconducting transition temperature T_c. When the sample thickness is decreased from bulk to monolayer, the corresponding T_c monotonically increases from 0.9 K to 3.4 K [2]. The trend observed in our experiment is strictly opposite that of

[2]For the monolayer flake, determination of T_c becomes tricky due to electrical shortage to adjacent flakes with different thickness. Detailed analysis and determination of T_c by critical current mapping can be found in the Supplemental Material.

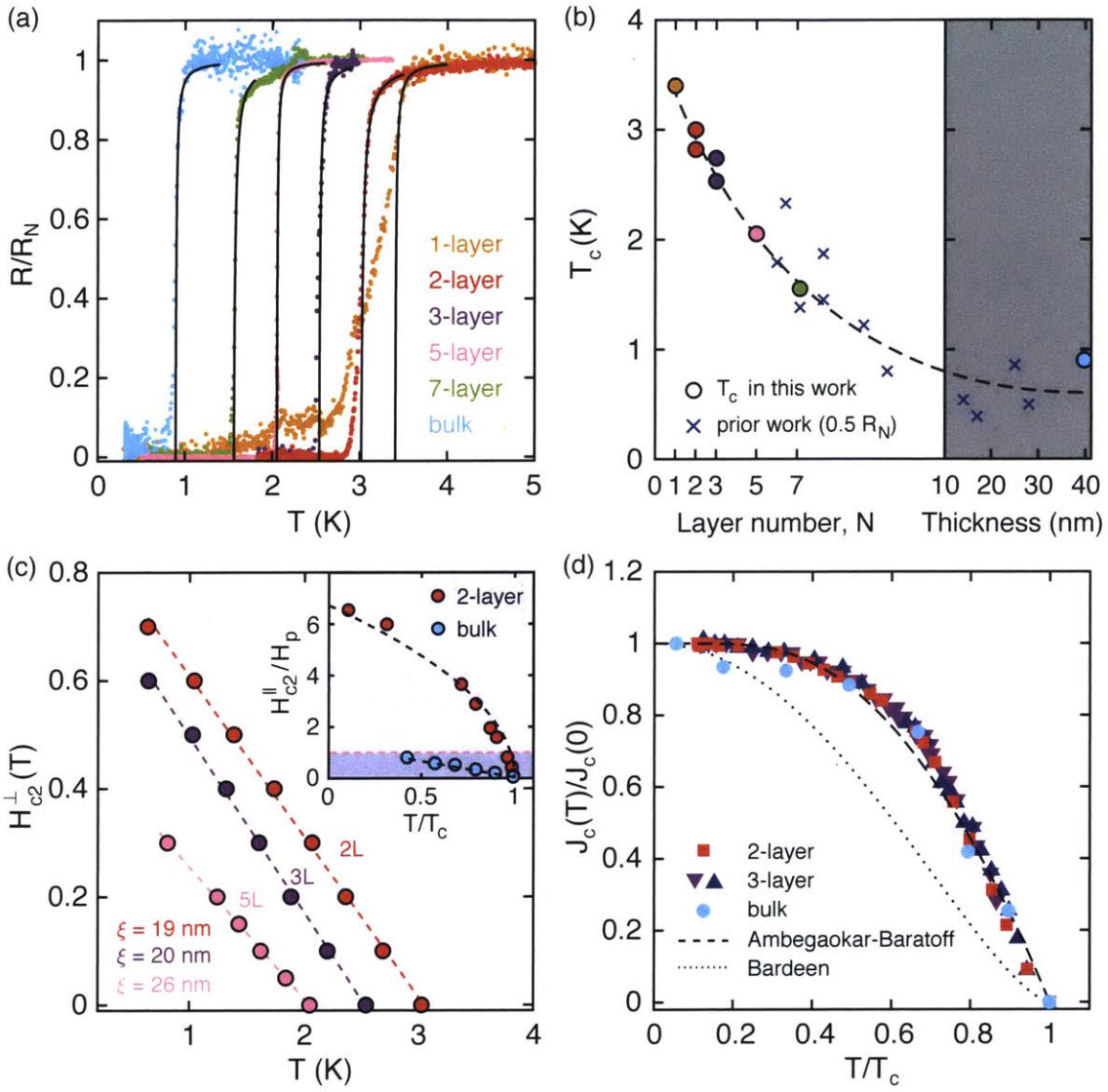

Figure 4-3: Thickness dependence of superconductivity properties in TaS_2. (a) Resistance normalized by the normal state (R/R_N) as a function of temperature for 1, 2, 3, 5, 7-layer and bulk (d = 40 nm) samples near the SC transition. The superconducting T_c is 3.4, 3.0, 2.5, 2.05, 1.6 and 0.9 K respectively, determined by fitting the transition curve to the Aslamazov-Larkin formula (black solid lines). (b) T_c reported in this work (circles) and in a prior study (crosses) [105]. The dashed line guides the eye to the general trend. (c) Out-of-plane critical field H_{c2} for 2, 3, 5-layer samples. The dashed lines are linear fits to $H_{c2}^{\perp} = \phi_0/(2\pi\xi(0)^2)(1 - T/T_c)$, where ϕ_0, $\xi(0)$ denote the flux quantum and in-plane GL coherence length at zero temperature, respectively. Inset: In-plane critical field $H_{c2}^{\parallel}$ normalized by Pauli limit ($H_p \approx 1.86T_c$) for bilayer and bulk samples. The dashed line for the bilayer is a fit to the Tinkham formula [137] for 2D samples $H_{c2}^{\parallel} = \sqrt{12}\phi_0/(2\pi\xi(0)d)\sqrt{(1 - T/T_c)}$. The purple background indicates the Pauli limit regime. (d) Normalized critical current as a function of T/T_c. Dashed and dotted lines denote the models proposed by Bardeen [9] and Ambegaokar-Baratoff [5], respectively.

a previous finding on $NbSe_2$ [156], where T_c decreases monotonically with thickness reduction, despite the fact that the two materials are isostructural and isovalent. In $NbSe_2$, the decrease in T_c is attributed to a weaker interlayer Cooper pairing as the layer number N is reduced. In our case, however, it is surprising to see that even with a reduced interlayer Cooper pairing, the T_c is dramatically enhanced when the thickness is reduced. To verify that the thickness dependence of T_c is independent of extrinsic factors (such as level of disorder, substrate, source of crystal, sample quality), we measure an additional set of bilayer and trilayer samples and plot our results alongside previously reported T_c values [105] in Fig. 4-3(b). Independent of different sample preparation procedures and substrates, the trend of T_c versus thickness is consistent between the two sets of experimental results, indicative of an intrinsic origin underlying the enhancement of T_c.

To further characterize the superconducting properties of thin TaS_2, we measure the superconducting transition under both out-of-plane and in-plane magnetic fields. Fig. 4-3(c) shows the $H_{c2}^{\perp}$ as a function of temperature. Close to T_c, the dependence of $H_{c2}^{\perp}$ is fitted well by the phenomenological 2D Ginzburg-Landau (GL) model, which yields $\xi(0) = 19,\ 20,\ 26$ nm for 2, 3, 5-layer respectively, where $\xi(0)$ denotes the GL coherence length at zero temperature. The reported values [68, 1] for 3D ranges from 22 nm to 32.6 nm. For in-plane field, we observe a much larger $H_{c2}^{\parallel} = 32$ T at 300 mK for a bilayer ($T_c = 2.8$ K), which is more than six times the Pauli paramagnetic limit H_p, obeying a square root rather than a linear temperature dependence (inset of Fig. 4-3(c)). This dramatic enhancement of in-plane $H_{c2}^{\parallel}$, often referred to as Ising superconductivity, has been observed in other 2D crystalline superconductors [91, 124, 156, 140]. The above observations verify that thin TaS_2 behaves as a 2D superconductor. We also show that the superconducting transition exhibits the Berezinskii-Kosterlitz-Thouless (BKT) transition as expected in 2D in Sec. B.2.1. Additionally, the critical current density increases by orders of magnitude as the devices become thinner (bulk $J_c \approx 700$ A/cm^2, trilayer $J_c \approx 7 \times 10^5$ A/cm^2, bilayer $J_c \approx 1.2 \times 10^6$ A/cm^2). The trend of critical current density versus temperature for representative thicknesses is shown in Fig. 4-3(d), with a more detailed discussion

given in Appendix B.2.2.

4.2.3 Transport properties and the CDW transition

In addition to the SC transition, bulk TaS_2 is known to exhibit CDW order below 70 K. The pattern of atomic displacements in the CDW state is illustrated in Fig. 4-4(a). In our experiment, we characterize the temperature dependent resistance of 2, 3, 5, 7-layer and bulk samples, and plot the normalized resistance versus temperature on a linear scale in Fig. 4-4(b). All samples manifest a linear decrease of resistance at high temperatures, consistent with phonon limited resistivity in a normal metal [39]. Below 70 K, the 7-layer and bulk devices undergo a CDW phase transition, producing a kink in resistance, which is manifested as a peak in $d\rho/dT$. In the inset of Fig. 4-4(b), the temperature derivative of the resistivity is shown, and a peak in $d\rho/dT$ develops in 7-layer and bulk samples close to the transition. In 2, 3, 5-layer samples, however, such a peak in $d\rho/dT$ is absent.

To further investigate the temperature dependence of the sample resistance, we plot the subtracted resistance $R - R_N(4\text{ K})$ on a log-log scale in Fig. 4-4(c). For bulk, the linear temperature dependence is disrupted by a sudden switch to T^5 near T_{CDW}, a well-known consequence of electron-phonon scattering at temperatures lower than the Debye temperature Θ_D. In contrast, a gradual transition to $R \sim T^2$ is observed in 2, 3-layer samples. It is important to note that these powers are only observed over the range between $T \sim 55$ K and SC T_c and thus extend over a bit less than a decade.

In bulk TaS_2, the Hall coefficient undergoes a broad transition between 70 and 20 K including a change in sign at 56 K [136], which is another indicator of the electronic structure change induced by the CDW transition. It has been shown that a two-carrier model with light holes and heavy electrons is necessary to explain the opposite signs for the Seebeck and Hall coefficients measured above the CDW transition temperature, as opposed to a single-carrier model describing the low-temperature behavior [136]. In Fig. 4-4(d), we plot the Hall coefficient (R_H) of three representative thicknesses below 100 K. In the 5-layer sample, a significant deviation from the bulk

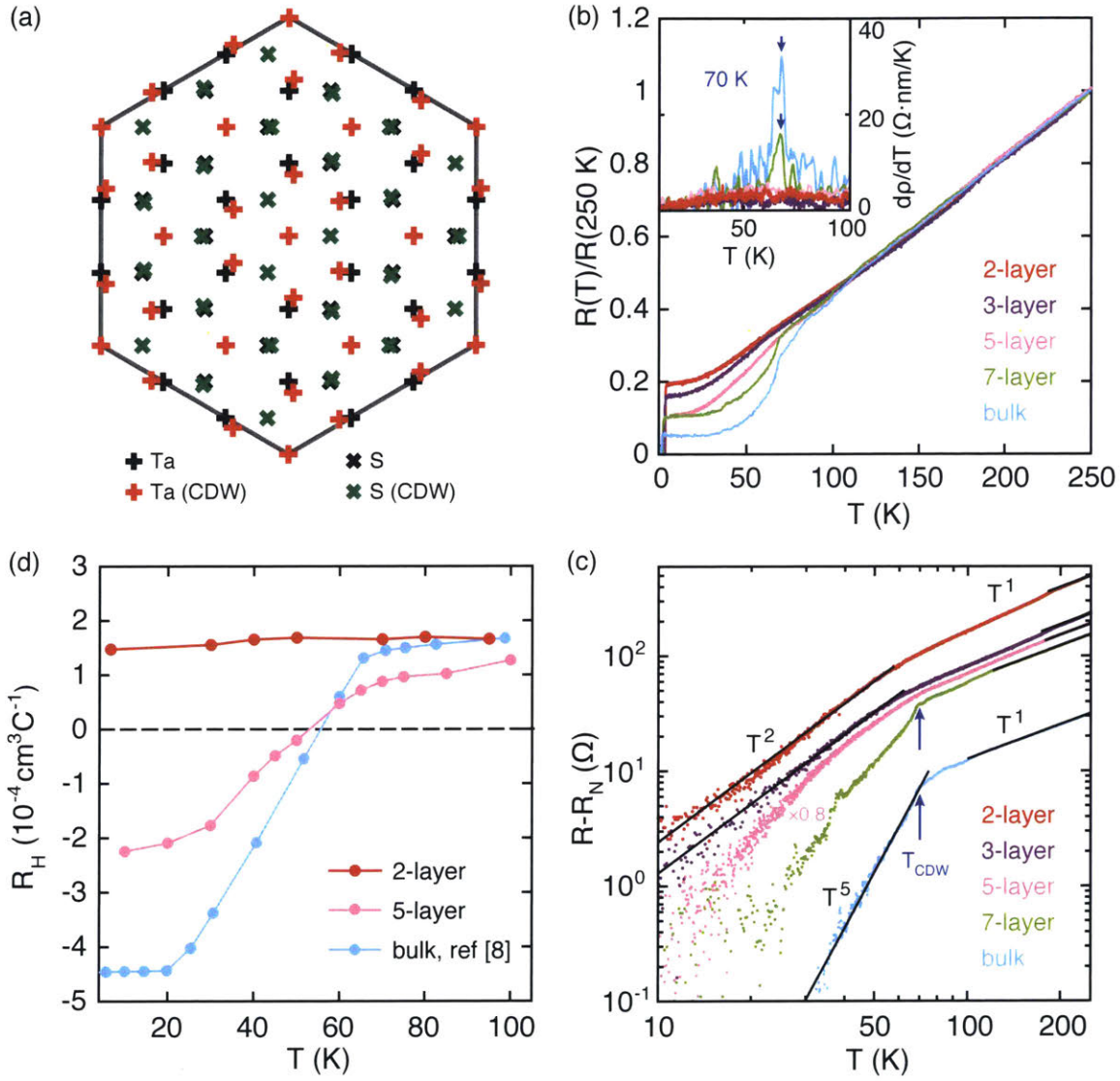

Figure 4-4: (a) Illustration of the atom position of Ta and S atoms in the normal phase and the CDW phase. The periodicity of the CDW order is 3×3. (b) Normalized resistance $R(T)/R(250K)$ for 2, 3, 5, 7-layer and bulk samples, measured while cooling down. Inset: derivative of the resistivity $\rho = d \cdot R$ close to the CDW ordering temperature. An arrow is used to mark the T_{CDW} for bulk and 7-layer, which both show a peak in $d\rho/dT$ at 70 K. (c) Resistance $R - R_N$ as a function of temperature plotted in a log-log scale, where R_N is the residual resistance just above the onset temperature of superconductivity. For clarity, data for 5-layer is scaled by a factor of 0.8. (d) Hall coefficient $R_H = d \cdot V_H/(I \cdot B)$ measured while cooling down. Data for the bulk crystal is from Ref. [136].

behavior is already apparent: the overall magnitude of R_H and temperature where it switches sign are both diminished. However, the most striking fact is the weak temperature dependence and absence of a sign change in the 2-layer sample. This implies that the same electronic structure modification caused by the CDW transition that affects the Hall coefficient is also absent in the 2D limit.

4.3 Discussion and conclusion

As superconductors are thinned down to the 2D limit, their critical temperature T_c typically decreases [60]. This suppression of SC is normally attributable to either disorder-induced localization of Cooper pairs, weaker Coulomb screening in 2D, or reduction of the superfluid stiffness which leads to a reduction of the BKT transition temperature. Recent studies reveal more novel origins of suppressed superconductivity in atomically thin $NbSe_2$, including a weaker interlayer Cooper pairing [156] and suppression of the Cooper pair density at the superconductor-vacuum interface [70]. Beyond these mechanisms, here we consider a key factor affecting T_c that not quantitatively studied in atomically-thin layered 2H-MX_2: the interaction with CDW order.

Anticorrelated trends between SC and CDW transition have been observed in bulk 2H-TaS_2 crystals under pressure [48, 1] and in single crystal alloys [144, 44, 83]. Here we hypothesize that the enhancement of T_c as sample thickness decreases all the way to the 2D limit is associated with a suppression of the electronic structure reconstruction induced by the CDW order.

4.3.1 DFT calculations

To better understand the possible interplay between the SC and CDW transitions, we investigate the electronic and vibrational properties of 2H-TaS_2 with density functional theory (DFT), as implemented in the VASP code [76, 75], which allows us to obtain the density of states (DOS) in the normal and the CDW phases for monolayer, bilayer and bulk. A comparison of Fig. 4-6(b) and (c) reveals an appreciable reduction

of DOS near the Fermi level induced by CDW order for all three thicknesses. This is consistent with previous magnetic susceptibility and heat capacity experiments showing a sharp drop of density of states below the CDW transition [37, 97].

We investigate next the effects of CDW on the band structure. In Fig. 4-6(a), we plot the band structures in the normal phase and in the CDW phase, denoted by red and grey curves. In order to display the band structure of the CDW phase in the original Brillouin zone (BZ), we need to "unfold" the calculated CDW band structure from the supercell BZ (sBZ) to the original BZ. This is achieved by performing a Wannier transformation [96] to decompose the extended Bloch wavefunctions onto localized atomic orbitals from the tight-binding Hamiltonian [45, 118] (see Appendix B.4.2 for more details). It is clearly seen in Fig. 4-6(a) that the CDW distortions result in a gap forming on the inner pocket around K along Γ-K and K-M. In addition, the saddle point located along Γ-K, is shifted to energies above the Fermi level. The reconstruction of electronic structures induced by the CDW order is also seen in the Fermi energy contour plots shown in Fig. 4-6(d) and (e). After the CDW transition, the pockets around K and Γ are either partially or fully gapped. This reconfiguration of electronic structures may account for the abnormal change of sign seen in the Hall measurement. However, a quantitative analysis is not possible without access to both the local curvature of the Fermi surface and the anisotropy in the scattering time at different k points. Given that the k dependent CDW-gap and SC-gap formation in 2H-MX_2 have been intensively studied by ARPES [71, 86], our DFT calculations can serve as a check of these results.

We also computed the phonon dispersion for the bulk and monolayer (see Fig. 4-5 and Appendix B.4.3). We find that in both cases, an acoustic mode that involves in-plane motion of Ta atoms softens and becomes unstable as the electronic temperature is lowered. In both cases the instability occurs at approximately the same wave vector that corresponds to the CDW ordering $\mathbf{Q}_{\mathrm{CDW}} \approx 2/3\,\Gamma\mathrm{M}$ [3]. This is in good agreement with the 3×3 periodicity of the CDW order observed in 2H-MX_2. One key message of this calculation is that CDW ordering remains energetically favorable even in the monolayer case.

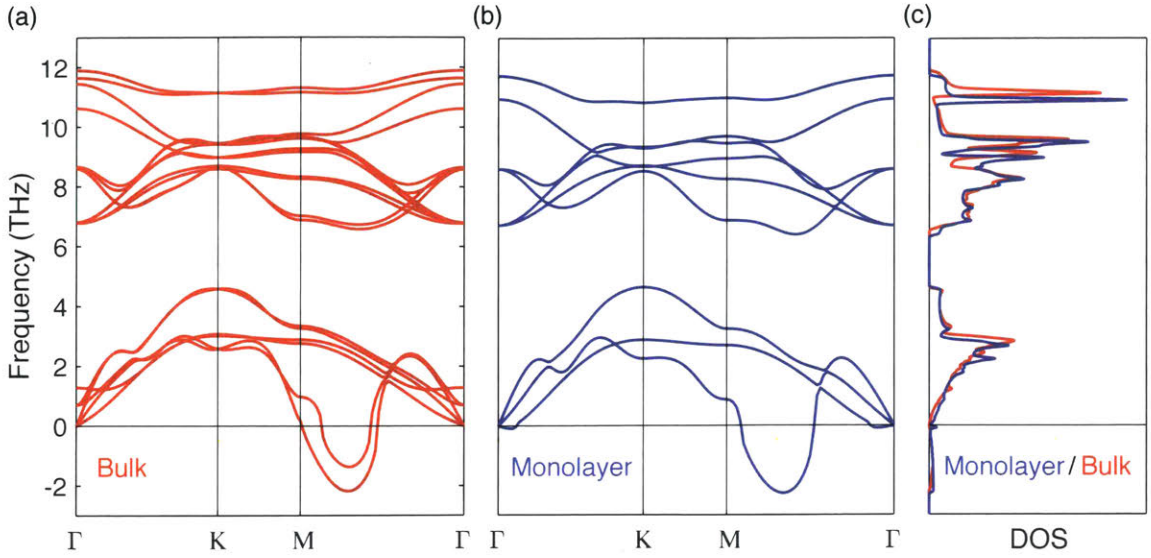

Figure 4-5: Phonon spectrum along Γ-K-M-Γ for TaS_2 (a) bulk, (b) monolayer crystals. (c) The comparisons of the density of states of the monolayer (blue) and the bulk (red) crystals.

4.3.2 Unconventional T_c enhancement

To investigate the change of T_c that may be induced by a suppression of the CDW order, we calculate T_c as a function of CDW amplitude based on electronic and phononic structure calculations. We recall that in McMillan's theory, the critical temperature is expressed as Eq. 4.15. We can investigate the impact of progressive weakening of the CDW by varying the magnitude of atomic distortion. A scaling factor, from 1 to 0, is used to define the fraction by which the magnitude of the atomic displacement is reduced with respect to the stable distorted configuration. The corresponding DOS as a function of atom displacement amplitude is calculated by DFT. Using the bulk as a starting point, we take into account the change in DOS(E_F) and a small phonon energy shift $\langle\omega^2\rangle$ calculated for the monolayer, and predict T_c within the McMillan formalism. We find that if the CDW distortion is completely suppressed, the corresponding change in DOS(E_F) can result in an enhancement of T_c up to 3.75 K (see Sec. 4.1.3). The result is summarized in Fig. 4-6(f). This provides a good approximate estimate on the impact of the suppression of the CDW instability on the superconducting T_c. Interestingly, this estimate agrees reasonably

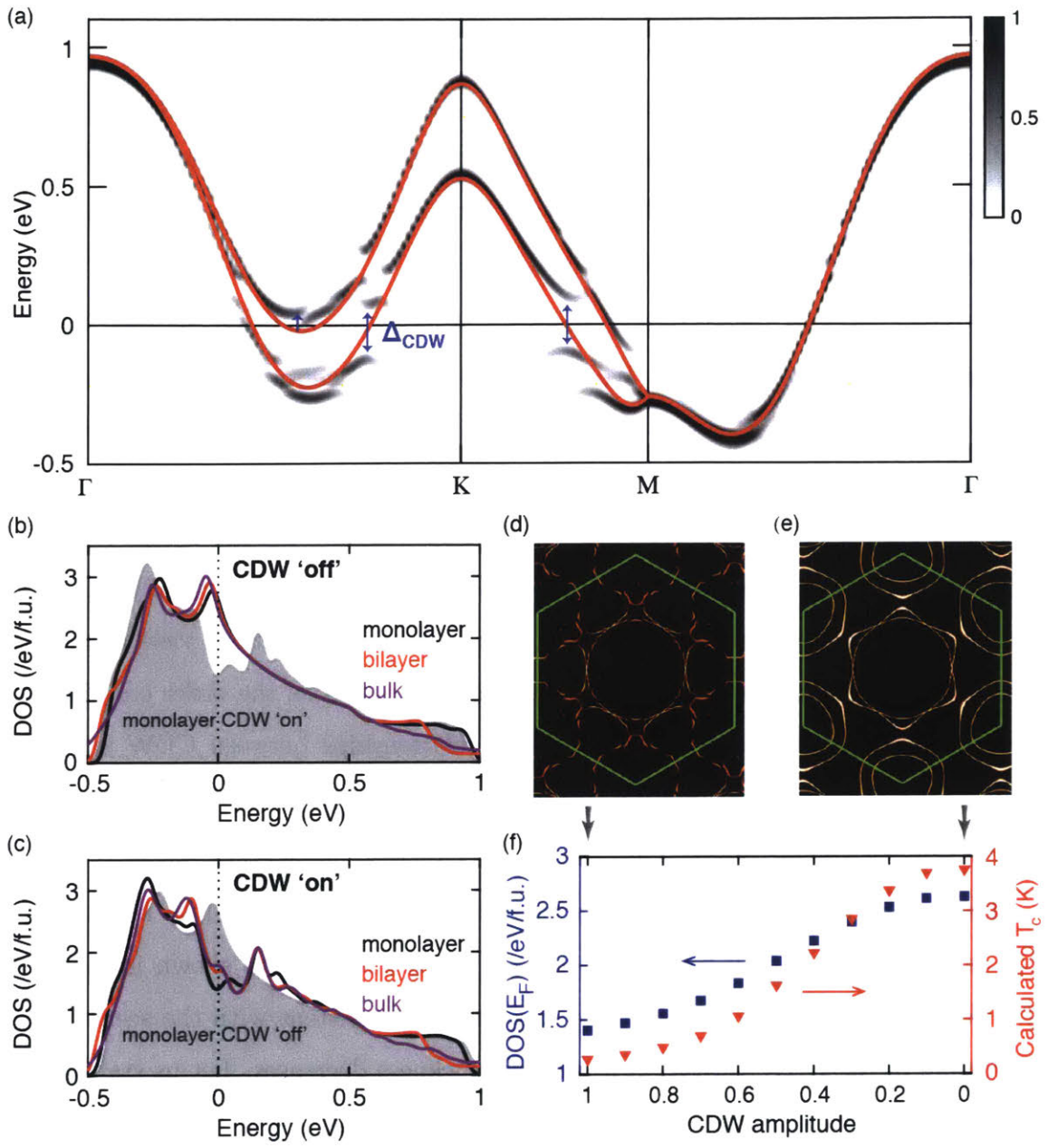

Figure 4-6: (a) Band structure for monolayer 2H-TaS_2. The grey lines show the unfolded band structure compared with the original band structure in the normal phase (red lines). (b) Density of states for monolayer/bilayer/bulk in the normal phase. Monolayer in the CDW phase is plotted as a grey shade for reference. (c) Density of states for monolayer/bilayer/bulk in the CDW phase. Monolayer in the normal phase is plotted as a grey shade for reference. (d) Energy contour at the Fermi energy in the CDW phase for monolayer TaS_2. (e) Energy contour at the Fermi energy in the normal phase for monolayer TaS_2. (f) Left axis: density of states at the Fermi level DOS(E_F) as a function of CDW amplitude for the monolayer. Right axis: T_c from McMillan's formalism [100] using the calculated DOS(E_F).

well with our experiment, indicating the importance of including electronic structure modifications induced by the CDW as a contributing factor. We note that there are several other factors that can impact T_c, such as substrate effects, the presence of a van Hove singularity near the Fermi level, enhanced electron-phonon coupling due to reduced screening [105] in 2D. These factors have been discussed in great detail in the literature and we do not reiterate them here.

The above analysis investigates primarily the direct competition between CDW and superconductivity over DOS. We further note that a continuous suppression of the CDW phase as a function of thickness would imply a softening of the CDW amplitude mode. If the presence of quantum fluctuations caused by proximity to a CDW transition is considered, the analysis of its impact on SC can go beyond a simple "competing order" scenario [150]. The competition between fermionic incoherence and the strong electron-mediated pairing near a quantum critical point can yield a pairing instability at temperature T_c which increases and saturates as the order correlation length $\xi \to \infty$. This reveals potentially rich relationships between CDW and SC that cannot be simply interpreted in the BCS framework as the material thickness is reduced towards the 2D limit.

After careful analysis of possible correlations between SC and CDW in TaS_2 by DFT calculations, we turn to a discussion on the transport data shown in Section 4.2.3. We will argue that the transport data is also consistent with the scenario of suppression of the CDW transition as sample thickness decreases. Let us start from the disappearance of the kink in the resistivity curve in Fig. 4-4(a). While the exact relation between the CDW ordering and the kink is not fully understood, its disappearance is definitely consistent with suppression of the CDW transition temperature or a complete disappearance of the ordering phase. The evolution of this kink was also studied in bulk samples of TaS_2 with intercalation, showing similar disappearance of the kink when the CDW order is suppressed [136]. The change in the power of the temperature dependent resistivity from T^5 to T^2 can also be explained within the same framework. However, in this case it is only consistent if the suppression of the CDW order is continuous, such that the gap of the amplitude mode of the

CDW becomes very small in ultra-thin samples. As we show in the Appendix B.5, when the gap of the amplitude mode is smaller than thermal excitations, scattering of electrons off these fluctuations leads to a strong T^2 contribution to the resistivity [61]. We also note that using a Kadawaki-Woods scaling [63] one finds that the T^2 resistivity from electron-electron scattering is expected to be much smaller than the one we measured. Finally, the absence of a change in the sign of the Hall coefficient indicates that the change in electronic structure occurring in the bulk is either absent or different in the 2D limit. Thus, it could be that the CDW order disappears, or a different type of CDW order is stabilized in the ultra-thin limit. In summary, we find that both the superconducting and transport data are consistent with the hypothesis that the CDW order is continuously suppressed when reducing the sample thickness towards the 2D limit. It is, however, important to point out that none of our probes directly measure such an effect and at this point it can only be viewed as a hypothesis consistent with multiple different measurements.

This is not the first experiment indicating that a CDW phase transition vanishes in reduced dimensions [136, 7, 114, 126, 166]. Its origin is still under debate [7, 50]. Recently, a study showed that lattice fluctuations arising from the strong electron-phonon coupling act to suppress the onset temperature of CDW order, leading to a pseudogap phase characterized by local order and strong phase fluctuations [47]. This is consistent with our model of presence of soft phonons, or CDW fluctuations [104] as primary contributor to the T^2 behavior of resistivity observed above T_{CDW}. More interestingly, theory predicts that quantum fluctuations caused by proximity to a CDW transition can boost superconducting pairing by providing sources of bosonic excitations [150]. Although there is no direct evidence that CDW fluctuations facilitate superconductivity in 2H-TaS_2, this scenario reveals a potentially rich relationship between CDW and SC.

4.3.3 Conclusion

In conclusion, we observe enhanced superconductivity in atomically thin 2H-TaS_2 accompanied with suppression of the CDW-induced transport signatures. Our elec-

tronic band structure calculations show that suppression of the CDW phase leads to a substantial increase in DOS(E_F), which acts to boost the superconducting T_c. Our result reveals that competition of the two ordered phases in determining the DOS can provide a reasonable explanation of the enhanced superconducting T_c in this material down to the monolayer limit. Future layer dependent studies that directly probe the CDW order, for example, through STM/STS, Raman and ultrafast spectroscopy measurements, will be essential to understanding the origin of the CDW formation and its stability against dimensional reduction. Future studies on the microscopic origin of the mechanisms (electronic, magnetic, electron-phonon, etc.) will be of paramount importance to comprehensive understanding of the mutual interactions between the CDW and SC.

Chapter 5

Machine Learning Assisted Identification of 2D Materials

5.1 Introduction

In 2003, one ingenious physicist took a piece of graphite, some Scotch tape and a lot of patience and persistence and produced a magnificent new wonder of material that is a million times thinner than paper, stronger than diamond, more conductive than copper. It is called graphene. It took the physics community by storm when the first paper appeared in *Science* magazine in 2004 [111], and it is now one of the most highly cited papers in materials physics. In 2010, the Nobel Prize in Physics was awarded jointly to Andre Geim and Konstantin Novoselov "for ground breaking experiments regarding the two-dimensional material graphene".

Despite numerous groundbreaking discoveries and proliferating research on graphene and 2D materials beyond graphene, mechanical exfoliation remains the best technique of producing such high-quality 2D materials. The procedure is illustrated in the left panel of Fig. 5-1. It relies on using Scotch tape to repeatedly peel away the top layer to achieve progressively thinner flakes attached to the tape. After transferring these flakes onto the surface of a silicon wafer, the flakes with different thicknesses are randomly distributed on a centimeter-scale wafer. After that, one need to spend hours seating in front of a microscope, in order to search for eligible micro-sized 2D

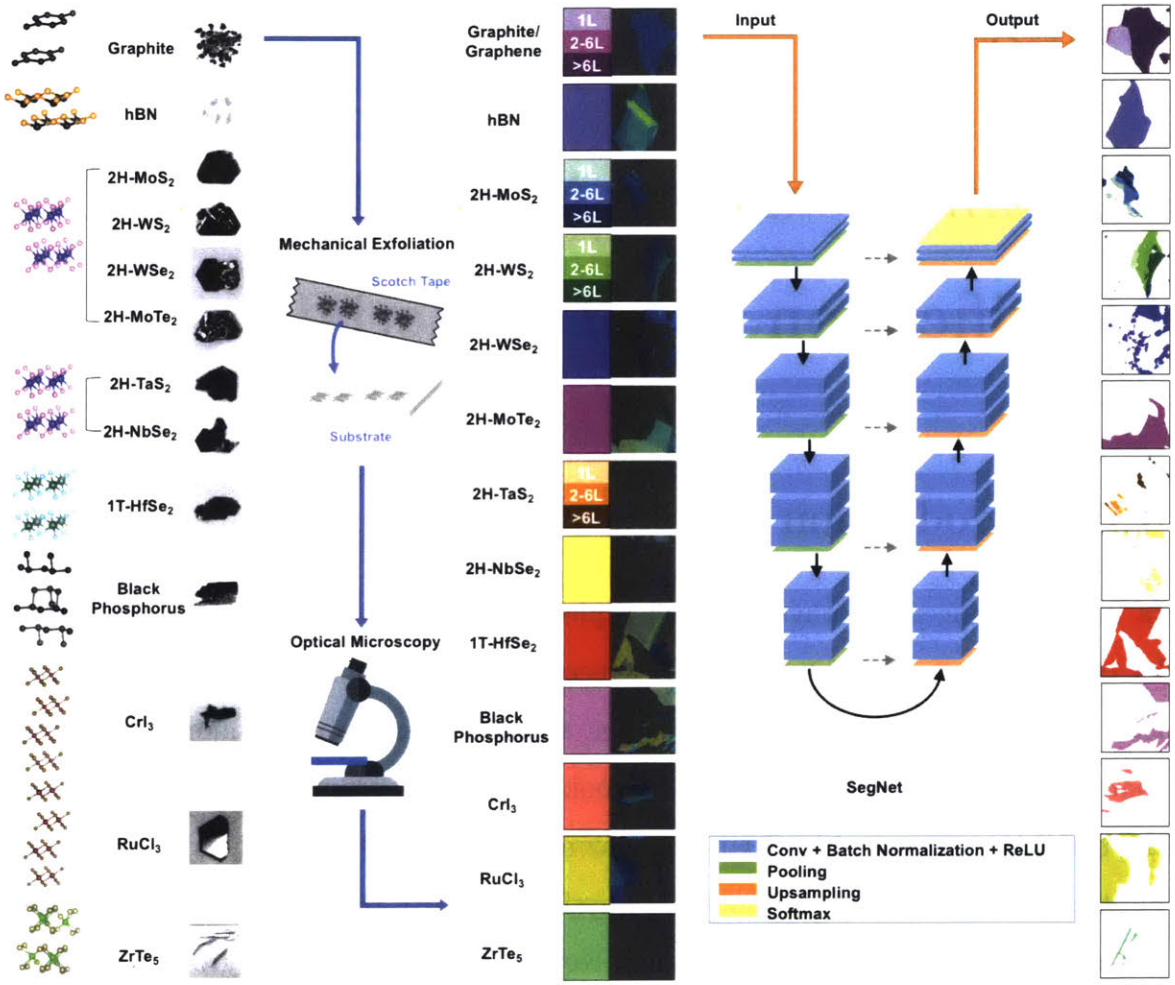

Figure 5-1: Project overview. We studied optical images of 13 different layered materials. For four types of crystals (graphite, MoS_2, WS_2, TaS_2), we also differentiate 1L (1 layer), 2-6L (2 to 6 layer) and $>$ 6L (larger than 6 layer). There are 22 pixel classes in total including "background". We developed a convolutional encoder-decoder semantic segmentation network ("SegNet") for pixel-wise image classification. It is capable of generating pixel-wise labels for input optical images of exfoliated 2D materials.

crystals for study. It would be fantastic if an automated "hunting" machine of 2D materials can be invented to replace human efforts. One of the key components of such an automated "hunting" machine is the algorithm to identify eligible flakes (i.e. single layer of 2D materials) in optical images of 2D materials. With the rapid development of deep learning, current semantic segmentation methods based on convolutional neural networks (CNNs) can analyze more complicated scenes than traditional methods, for applications such as autonomous vehicles and medical image diagnostics [90, 27, 121, 8]. These methods also fit the needs for processing microscopy or spectroscopy data.

In this chapter, we present deep learning assisted identification of 2D materials using semantic pixel-wise segmentation methods. This network is capable of generating pixel-wise labels for optical images of 2D materials. We show that this network can differentiate subtleties of different crystals as well as different thicknesses of the same crystal. This work is done with Yuxuan (Cosmi) Lin from Tomás Palacios's group, and Bingnan Han from Jing Kong's group.

5.1.1 Background

As mentioned above, to realize automated identification of eligible nanosheets of 2D materials, a robust optical identification algorithm is essential. It is desirable that the algorithm can be: 1) generic, thus applicable to different images of different 2D materials taken by different people from different research groups; 2) adaptable, in case that condition of image taking, material types or identification criterion changes; 3) fast, so that it can allow real-time processing.

Recently, several efforts have been made to automate such a process [18, 108, 26, 55, 120, 82, 67, 84, 95, 88]. These optical identification methods are mostly based on optical contrast of the 2D crystals, and as a result, they are usually very specific to a particular type of 2D crystals, the conditions and configurations of the microscope being used, and subject to the quality of images, etc. The requirement for optical contrast based method to work for multiple optical images is very stringent. First, all the conditions (microscope, light source, substrate) need to be kept exactly the

Figure 5-2: Representative optical images with different hues and brightnesses before (first row) and after (second row) normalization.

same. Second, the pixels that need to be differentiated must be well-separable in the color space. However, variations in quality of images are ubiquitous in real-world optical images of 2D materials, as shown in the first row of Fig. 5-2. There exist all sorts of variations in real world optical images, including brightness, white-balance, substrate thickness and so on. Different objectives or different brands of microscope can also generate different optical images. In addition, some images suffer from the problem of uneven illumination due to the lamp of the microscope. These variations greatly hamper the capability of contrast based or clustering based algorithm (details of clustering based technique can be found in Appendix C.1.2). Here we developed an image normalization algorithm by transforming RGB image to L*a*b color space and using background color as a reference for normalization. The result is illustrated in Fig. 5-2. For more details about this image normalization process, see Appendix C.1.1.

5.1.2 Deep learning for image segmentation

Semantic segmentation has wide applications ranging from scene understanding, inferring support-relationships among objects to autonomous driving. For example, in scene understanding tasks, it is capable to model appearance (road, building), shape (cars, pedestrians) and understand the spatial-relationship (context) between different classes such as road and side-walk. It is illustrated in Fig. 5-3.

This is achieved by a convolutional encoder-decoder semantic segmentation net-

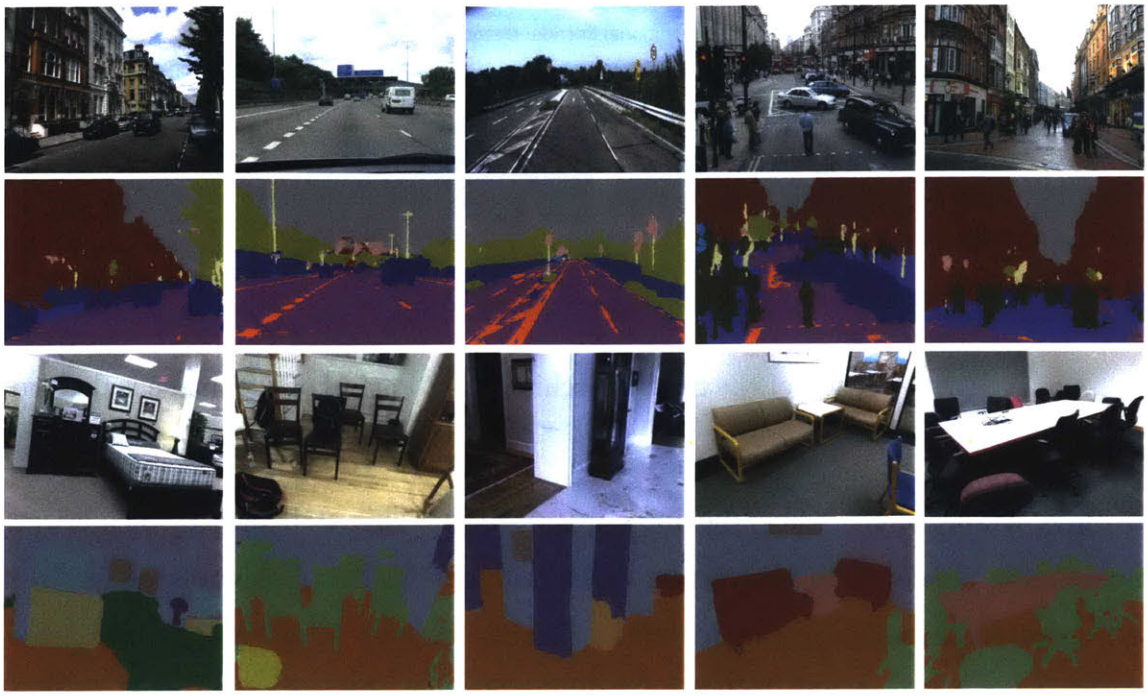

Figure 5-3: SegNet predictions on road scenes and indoor scenes from Ref. [8].

work ("SegNet") for pixel-wise image classification. This SegNet [8] we use in our paper has an encoder network and a corresponding decoder network, followed by a final pixel-wise classification layer. The architecture is illustrated in the right panel of Fig. 5-4. The encoder network consists of 13 **convolutional** layers which correspond to the first 13 convolutional layers in the VGG16 network [131] designed for object classification. In this experiment, we fix the number of convolutional kernels in each convolutional layer and the number convolutional layers in each depth to be 64 and 2, respectively, rather than varying them gradually as the layer becomes deeper, as in the case of the VGG16 structure. Each encoder in the encoder network performs convolution with several **filters** to produce a set of **feature maps**, followed with **batch normalization**. Then an element-wise **ReLU** layer is applied. Then a **max-pooling** layer with a 2×2 window and stride 2 is performed and result in downsampling of the image by a factor of 2. Besides, the network stores the max-pooling indices, i.e, the locations of the maximum feature value in each pooling window is memorized for each encoder feature map.

The decoder produces sparse feature maps in the decoder network by **upsampling**

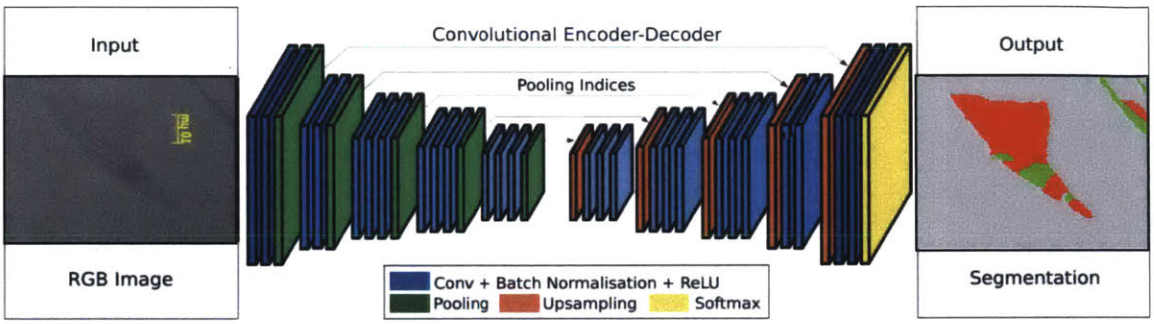

Figure 5-4: An illustration of the SegNet architecture. Part of of the image is derived from Ref. [8]

its input feature maps using the **max-unpooling**. This step utilizes memorized max-pooling indices from the corresponding encoder layers. **Convolution** is then performed on these feature maps with trainable decoder filters to produce dense feature maps, followed with **batch normalization**. An element-wise **ReLU** layer is then applied. After equal number of upsampling to match the input size, the final output feature maps are fed to a soft-max classifier for pixel-wise classification. The predicted segmentation is matched to the class with maximum **softmax** probability at each pixel.

Semantic segmentation network in a nut shell

To understand the functionality of each layer of the SegNet, we briefly introduce some basic components in the SegNet. Some of the descriptions can be found in Wikipedia. The full architecture of the SegNet is shown in Appendix C.2.

Convolution In deep learning, a convolutional neural network (CNN, or ConvNet) is a class of deep neural networks, most commonly applied to analyzing image. It is capable of assigning importance (learnable weights and biases) to various aspects/objects in the image. The **feature maps** generated by convolutional layers can be used to differentiate one image from the other by learning appropriate **filters**. A convolutional neural network consists of an input and an output layer, as well as multiple hidden layers. The hidden layers of a CNN typically consist of **convolutional** layers, **ReLU** layer i.e. **activation func-**

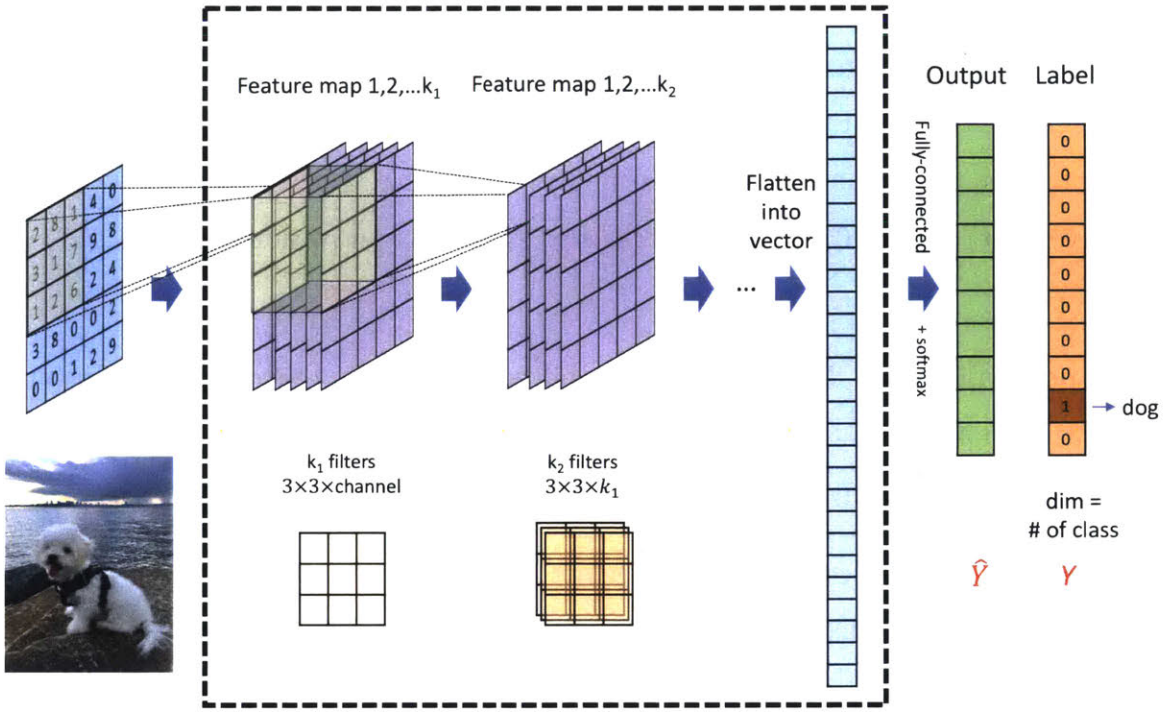

Figure 5-5: Illustration of a convolutional neural network for image classification.

tion, **pooling** layers, **fully connected** layers and normalization layers. This is shown in Fig. 5-5.

Pooling Convolutional networks may include pooling layers. Pooling layers reduce the spatial size of the convolved feature by combining the neuron clusters at one layer into a single neuron in the next layer. There are two types of pooling: max pooling and average pooling. **Max pooling** returns the maximum value from the portion of the image covered by the kernel. **Average pooling** returns the average of all the values from the portion of the image covered by the kernel. The kernel size is typically 2×2. Max pooling can extract dominant features and also perform as a noise suppressant.

Fully connected Fully connected layers connect every neuron in one layer to every neuron in another layer. It is in principle the same as the traditional multi-layer perceptron neural network (MLP). The flattened matrix goes through a fully connected layer to classify the images.

Activation function The activation function of a node defines the output of that node, or neuron, given an input or set of inputs. It adds none-linearity to the neural network. It decides whether a neuron should be "fired" (activated) or not. For example, **ReLU** is the abbreviation of rectified linear unit, which gives $f(x) = \max(0, x)$. **Softmax** is also a common activation function $f_i(\vec{x}) = \frac{e^{x_i}}{\sum_j e^{x_j}}$.

Batch normalization To increase the stability of a neural network, batch normalization normalizes the output of a previous activation layer by subtracting the batch mean and dividing by the batch standard deviation.

Upsampling The key component of SegNet is the decoder network which consists of a hierarchy of decoders with **unpooling** layers corresponding to each **pooling** layer in encoder. The appropriate decoders use the **max-pooling** indices received from the corresponding encoder to perform non-linear upsampling of their input feature maps.

Training The process of optimizing weights and biases in the network to achieve desirable performance. **Training dataset** is the actual dataset that is used to train the model. The model sees and learns from this data.

Validation A sample of data is used to provide an unbiased evaluation of a model fit on the training dataset while tuning model hyperparameters. This sample is called **validation dataset**. It produces more unbiased result if the validation dataset is separated from the training dataset. Sometimes cross-validation is used where validation dataset is incorporated into the model configuration.

Test The process of providing an unbiased evaluation of a final model fit on the **test dataset**.

5.1.3 Image segmentation toolbox in Matlab

Matlab provides a toolbox (since 2018 version) for image segmentation. Fig. 5-6 shows a semi-automatic labeling process using the toolbox. Foreground and background

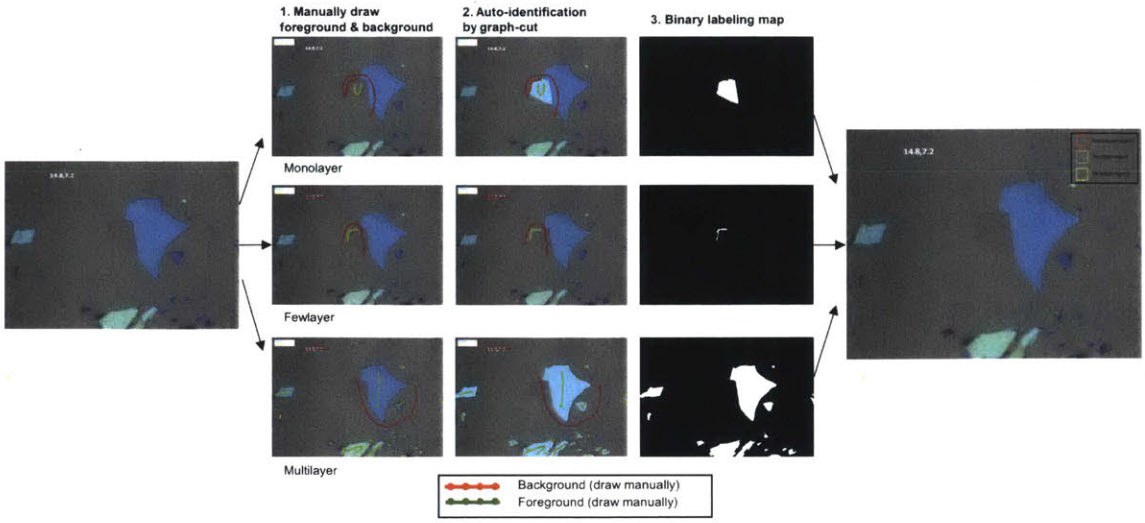

Figure 5-6: Image segmentations with Matlab image segmentation toolbox. In each step, the pixels of one class is specified by user and corresponding binary mask is created. The final pixel-label result combines all binary masks and assign the pixels that are not in the masks as "background".

Material	Crystal system	Point group	Space group	Bandgap	Exfoliation energy
graphite	Hexagonal	D_{6h}	$P6/mmm$	0 eV	70.36 meV
hBN	Hexagonal	D_{6h}	$P6_3/mmc$	~6 eV	71.34 meV
2H-MoS_2	Hexagonal	D_{6h}	$P6_3/mmc$	1.8 eV	76.99 meV
2H-WS_2	Hexagonal	D_{6h}	$P6_3/mmc$	2.1 eV	76.27 meV
2H-WSe_2	Hexagonal	D_{6h}	$P6_3/mmc$	1.7 eV	79.63 meV
2H-$MoTe_2$	Hexagonal	D_{6h}	$P6_3/mmc$	1.1 eV	90.98 meV
2H-TaS_2	Hexagonal	D_{6h}	$P6_3/mmc$	0 eV	87.15 meV
2H-$NbSe_2$	Hexagonal	D_{6h}	$P6_3/mmc$	0 eV	98.28 meV
1T-$HfSe_2$	Trigonal	D_{3d}	$P\bar{3}m1$	1.1 eV	92.05 meV
BP	Orthorhombic	D_{2h}	Cmce	~0.5 eV	111.62 meV
CrI_3	Monolithic	C_{2h}	C2/m	1.2 eV	-
$RuCl_3$	Monolithic	C_{2h}	C2/m	0.3 eV	-
$ZrTe_5$	Orthorhombic	D_{2h}	Cmcm	0 eV	90.00 meV
$1T_d$-WTe_2	Orthorhombic	C_{2v}	$Pmn2_1$	0 eV	84.90 meV

Table 5.1: Summary of the physical properties of the 2D materials used in this study [152, 15, 99, 78, 132, 159, 57, 28, 175].

can be specified by users and a corresponding graph cut can be auto-identified and created. In this way, we can create a label map for each class and then combine it into a multi-class label map.

5.2 Training and analysis

We start with optical images of 13 different layered materials (Fig. 5-1), including graphene/graphite, hBN, 2H-MoS_2, 2H-WS_2, 2H-WSe_2, 2H-$MoTe_2$, 2H-TaS_2, 2H-$NbSe_2$, 1T-$HfSe_2$, black phosphorous (BP), CrI_3, $RuCl_3$ and $ZrTe_5$. These 2D materials offer a full variety of optical and electrical properties, such as metals, semiconductors, insulators, magnets and superconductors. The physical properties of these 2D materials such as crystal structure, optical band-gap and exfoliation energy is summarized in Table 5.1.3. There are in total 850 labeled images used in our study. These images are taken by more than 30 users from different research groups using 6 different microscopes in a time span of greater than 10 years. Many of them are contributed from Pablo Jarillo-Hererro's group @ MIT Physics.

By utilizing the segmentation toolbox in Matlab (some of them are labeled by a Superpixelization + DBSCAN clustering based algorithm explained in Appendix C.1.3), we are able to associate each pixel in the optical image to either background or one of the 13 crystals. In particular, for four crystals - graphene, 2H-TaS_2, 2H-MoS_2 and 2H-WS_2 - we also assign the labels according to their thicknesses. The categories are 1-layer (1L), 2- to 6-layer (2-6L) and larger than 6-layer ($>$ 6L). There are 22 categories in total including the "background". Images are then normalized in l*a*b color space as illustrated in Appendix C.1.1. We then perform data augmentation involving cropping and random transformation. After cropping, the input images have size of 224 $\times$ 224 pixels. We feed 90% of the augmented data (22,950 RGB images) to the semantic segmentation network as described in Sec. 5.1.2 and reserved 10% (2,550 RGB images) for validation. The network is trained in a GPU environment.

It is worth mentioning that in our training dataset, there is a large variation in the number of pixels from each class in the training dataset. For example, number of

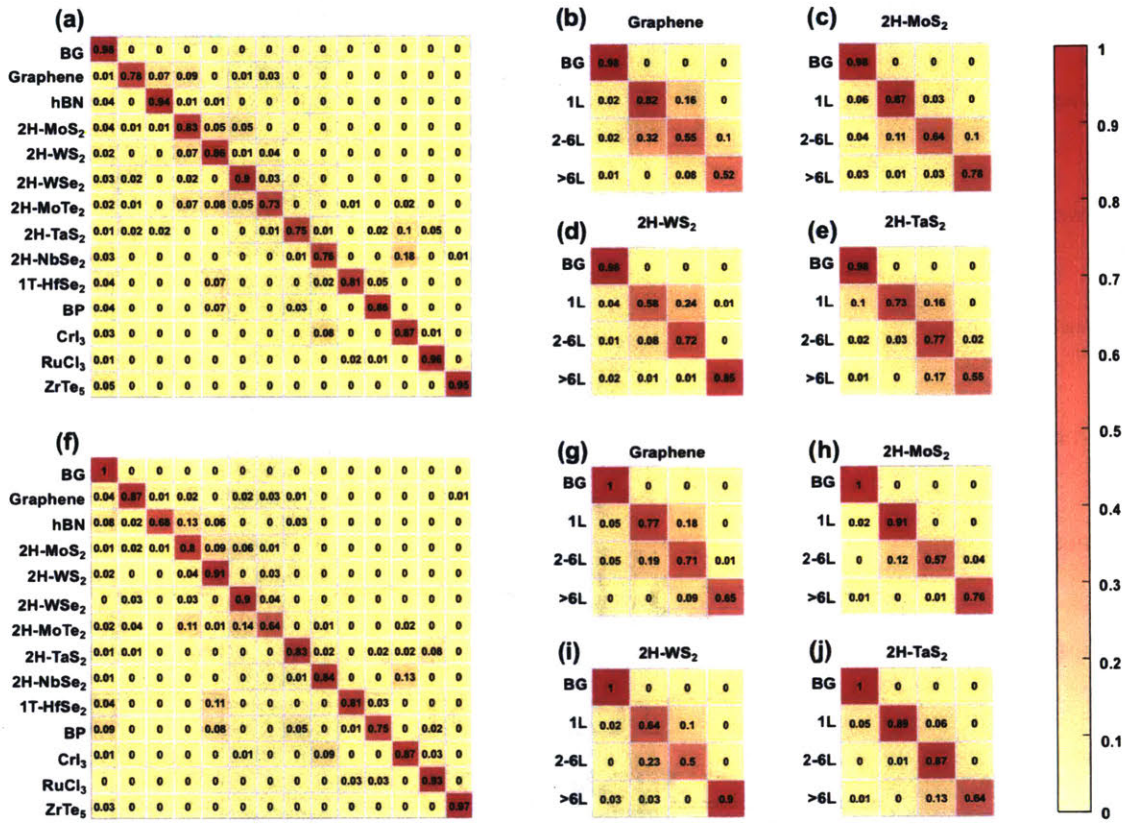

Figure 5-7: Confusion matrix of pixel-level classification for (a) 13 crystals, (b) graphene with different layers, (c) 2H-MoS_2 with different layers, (d) 2H-WS_2 with different layers, (e) 2H-TaS_2 with different layers. Confusion matrix of flake-level classification for (f) 13 crystals, (g) graphene with different layers, (h) 2H-MoS_2 with different layers, (i) 2H-WS_2 with different layers, (j) 2H-TaS_2 with different layers. "BG" stands for background. "L" in "1L" denotes 1 layer.

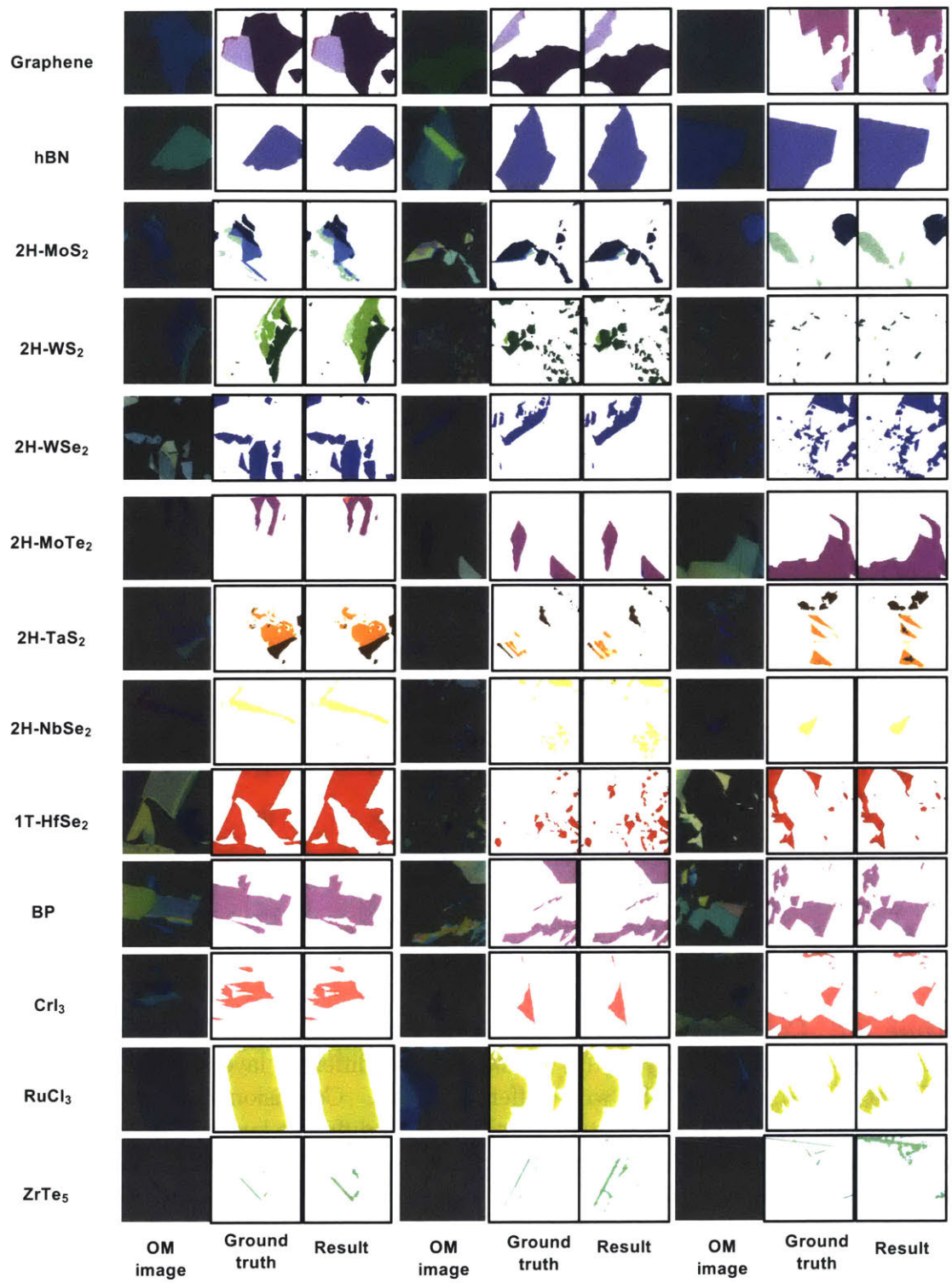

Figure 5-8: Test results. The first row is the optical microscope (OM) image of 2D materials. The image has been normalized in color space. The second row is the pixel-wise labels created by human researchers, which is called "ground truth". The third row is the pixel-wise labels generated by SegNet, which is called "result".

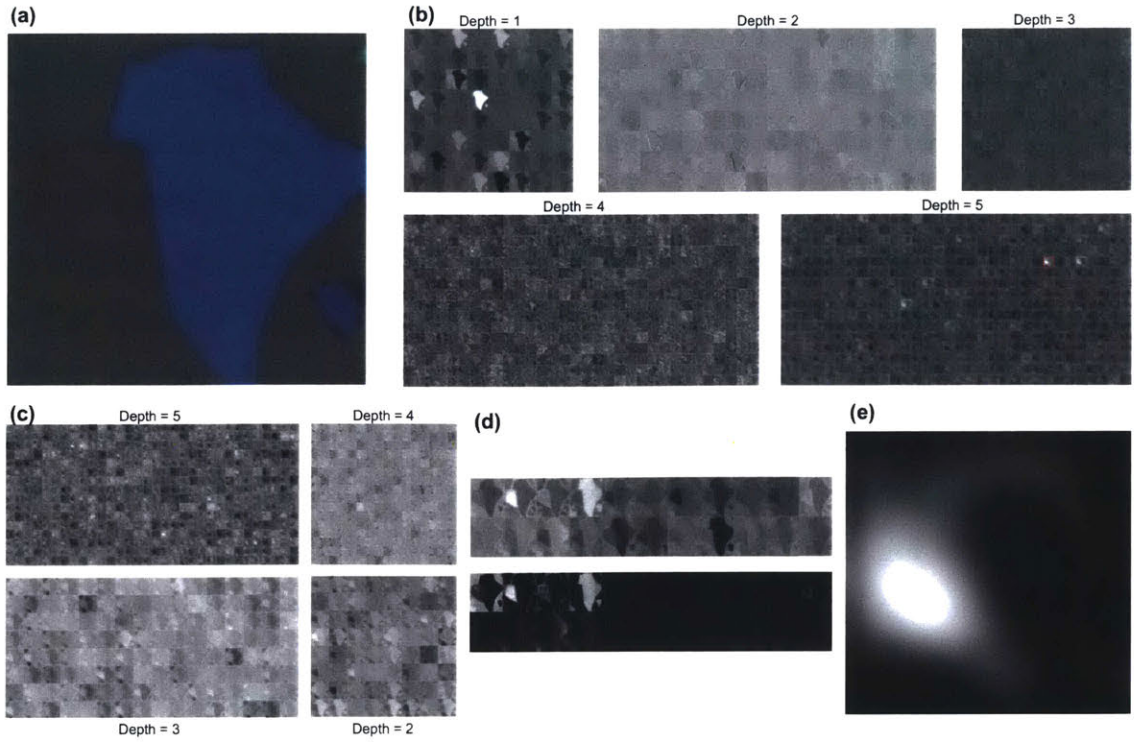

Figure 5-9: Feature maps in the trained SegNet. (a) the input OM image. (b) Depth=1 to 5 encoder layers. Channel #153 of the Depth=5 encoder layer is circled by red. (c) Depth = 5 to 2 decoder layers. (d) The last decoder layers (conv. and ReLU layer). (e) Channel #153 feature map of the Depth=5 encoder layer.

"background" pixels is expected to be much larger than number of pixels labeled with any 2D materials. If not handled properly, this imbalance can jeopardize the learning process and the correct labeling of the dominant classes will always be favored. It hampers the capability to classify small object in the image. Therefore, there is a need to weight the loss differently based on the class pixel numbers. One way to assign the weights is to compute the ratio of the median of class frequencies based on the entire training set divided by the class frequency. The weights are then assigned to each class when calculating the loss function.

With our computing environment (see Appendix C.3), the training process for the VGG16 SegNet took around 9 hours with a GPU, whereas the testing speed can be as high as 3 frames per second (fps) using a CPU, and 20 fps using a GPU. This means the SegNet, once properly trained, and be easily adapted to computers with common configurations and integrated to an optical microscope with an automatic scanning

stage for fast or even real-time identification.

Here in Fig. 5-7 shows the pixel-level and flake-level classification accuracy for different categories for validation dataset. It is reflected in the confusion matrix heat map. Each row of the matrix represents the labeled class while each column represents the percentage of pixels labeled in an actual class. The diagonal elements in confusion matrix describe the correctly labeled percentage of pixels. We also plot the confusion matrix within each crystal types that have sub-classes of different thicknesses. The accuracy of different classes ranges from 73% to 98%. Fig. 5-1 also shows representative label outputs of test images for each crystal class. More test results can be found in Fig. 5-8. The rows in the figure correspond to optical microscope (OM) image, human labeled ground truth and label result generated by SegNet. As one can see from this figure, the result generated by SegNet agrees very well with ground truth.

In addition to classification accuracy, it is interesting to explore what has been learnt by our neural network. To understand how the SegNet extracts features from 2D material optical microscopy images, we analyzed the output feature maps of all the layers in the trained network for OM images in the test dataset as the inputs. As a demonstration, we used a typical image of graphite/graphene (shown in Fig. 5-9 (a)) as the input. The corresponding convolutional feature maps of all the layers in the encoder, decoder, and output sections of the SegNet are summarized in Fig. 5-9 (b)-(d). Taking the convolutional feature maps in the encoder as an example (Fig. 5-9 (b)), we can clearly see that Depth=1 feature maps are highly correlated to color and contrast information. In this shallow layer, the background and monolayer region of graphene are not easily separable because of the weak contrast between the two classes, whereas multilayer graphene region is already quite distinguishable. In Depth=2 feature maps, more boundary characteristics are detected, and the edges of graphene monolayer regions start to stand out in some of the feature maps. With the increase of the depth, the size of each feature map becomes smaller because of the pooling layers in the network, and the receptive field of each convolutional kernel becomes relatively larger, which leads to a higher level abstraction of the global

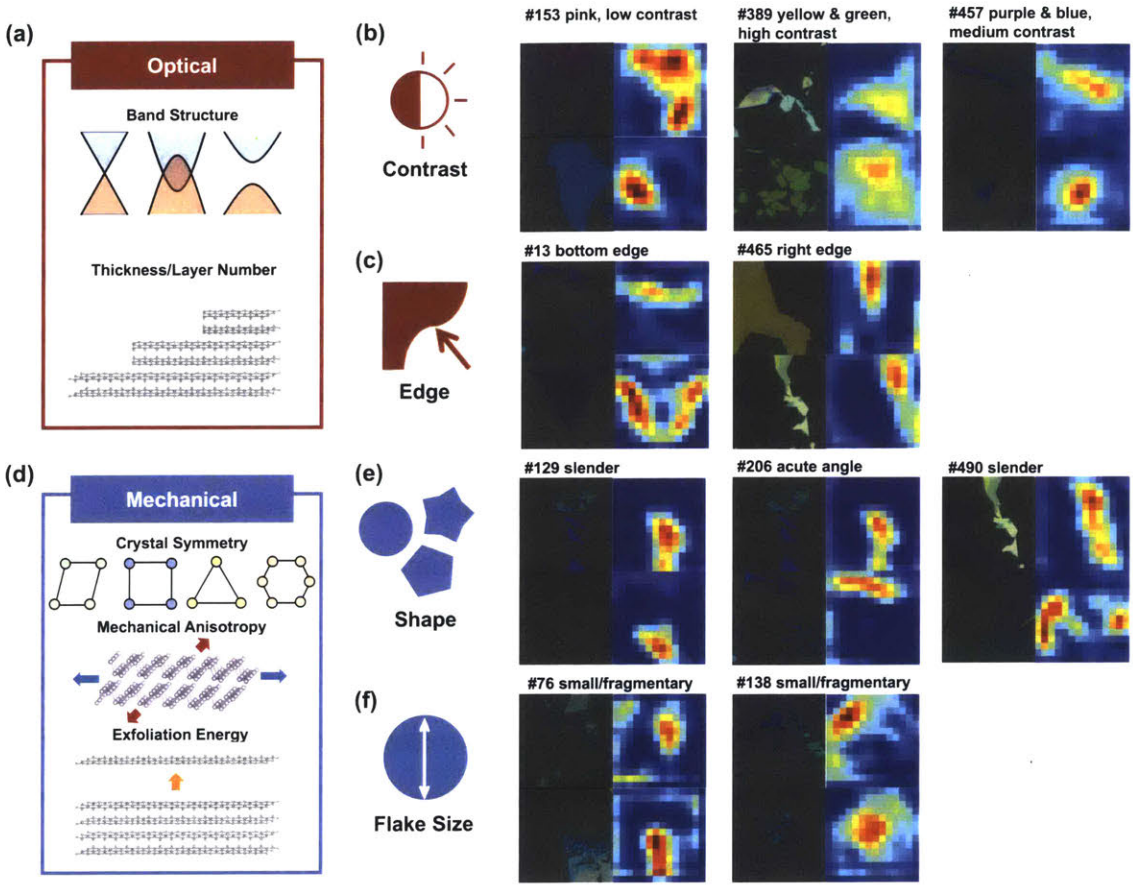

Figure 5-10: Investigation of feature extraction mechanism in the SegNet. (a) Optical properties such as band structure and layer thickness can lead to (b) object contrast and determine (c) object edges. (d) Mechanical properties can impact the (e) flake shape and (f) flake size. All these properties are captured by feature maps generated by different filters in the encoder network.

graphical features. For instance, Fig. 5-9 (e) displays the most prominent feature map (Channel #153) of the Depth=5 encoder layer with the largest activation value. It is observed that this feature map is highly correlated to the monolayer graphene region. By feeding the network with more images that contain thin layers of graphene and other materials as summarized in Fig. 5-10, we further confirmed that Channel #153 is actually sensitive to pink/ light purple flakes with smooth edges and regular shapes.

In the SegNet architecture, the deepest layer (Depth = 5) in the encoder part contains the most dense features that SegNet learns from a particular image. It is enables by the hierarchy of filters in the convolutional layers of the encoder. By investigating the feature maps generated in Depth = 5 layer in the encoder component, one can tell what characteristics in the image has been captured by different filters. In our study, we feed several test images into the neural network, and examine the feature maps generated by the 512 channels of the Depth=5 encoder layer. Out of 512 channels, there exist a few that we can associate interpretable functionality. For example, some of the filters are good at recognizing low contrast objects, while others are better at detecting objects with higher contrast. Some filters are good at detecting edges, while some filters are sensitive to slender objects or objects with acute edges. Some filters are capable of differentiating small fragments from others. These observationss are summarized in Fig. 5-10. It confirms that our neural network is capable of generalizing and detecting various intrinsic properties and universal features of 2D crystals through learning.

The above feature map analysis has provided a better understanding about how deep graphical features can be exploited by the SegNet for more accurate and generic optical identification of exfoliated 2D materials. More interestingly, we found that the same trained network can be used for more advanced tasks such as prediction of material properties. The deep graphical features captured by the network are correlated to the optical and mechanical properties of the material. This work demonstrates a promising deep learning platform to realize fully automated 2D crystals 'hunting'.

5.3 Outlook

Now it is time to re-examine the robustness of the deep learning assisted technique for identification of 2D materials. First, as is shown in the previous section, this deep learning algorithm is capable of generating reasonable pixel-label result for various images (850 original images, 13 materials, 22 categories, $>$ 30 users from 8 research groups, 6 microscopes, $>$ 10 years' time span). These images offer a full variety of substrates and material types and microscope/lamp conditions. Therefore, we believe that this is a universal method for reliable identification of 2D materials, not necessarily constrained to images taken under specific condition.

Second, an important advantage of our machine learning method, is that it is adaptive. It can pass on the learnt knowledge to a new identification task, where pre-trained models are used as the starting point of the new model. This can greatly enhance the training process, especially when the dataset of the new task is limited. In a new study, we conducted a new identification task on $1T_d$-WTe_2, which is not seen by the SegNet. Only 41 labeled images are provided, and 31 of them are used for training. By loading the pretrained network and about 4 hours' training, we can achieve 96.7% global accuracy.

Last, the test speed of our network reaches 2.8 fps (frame per second) for CPU environment and 20 fps for GPU environment. This is fast enough to allow real-time processing.

In brief, we show that identification of 2D materials can be readily and reliably fulfilled using a deep learning architecture, without complex set-up or expensive instrument. By this development, we can reduce the human intervention involved in the 2D material device fabrication by orders. We believe that this work is able to free up researchers from time-consuming repetitive tasks and allow them to focus on more intellectually creative tasks. It will greatly facilitate the autonomous robotic searching and assembly of two-dimensional devices, thus expedite their research toward practical applications.

Moreover, the fact that the SegNet is capable of differentiating different 2D ma-

terials is also worthy of attention. We know that the library 2D materials offer a full variety of mechanical, electronic and optical properties. By far, there is no systematic study on the morphology and color tonality of exfoliated 2D crystals as well as their relationship to the intrinsic mechanical, electronic and optical properties of the material. The subtleties of morphology and color tonality of different exfoliated 2D crystals may not be captured by human eyes, or it is hard to cross validate the analysis if the images are taken under different conditions. Therefore, optical images are not yet proven as reliable sources to infer crystal properties. However, it is possible that a deep learning neural network is capable of summarizing enough features from images and infer their intrinsic properties utilizing the morphology and color tonality information. It would be very exciting if our deep learning algorithm that is based on optical images can serve as a technique, similar to X-ray and Raman spectroscopy, to infer crystal structures or optical properties in the future.

Appendix A

WSe_2 High Mobility Devices: Supplementary Information

Here we present supplementary information for Chapter 3.

A.1 Characterization of Sample B at 220 K

In Chapter 3, we showed transport measurement performed on two different devices, sample A and B. Sample B is a 4-layer WSe_2 device, with the same device structure as sample *A*. Fig. A-1 shows the current characteristic and extracted contact resistance and conductivity for different ionic liquid gate settings. As shown in Fig. A-1 (a), by changing the ionic liquid gate voltage V_{IL} from 0 V to -3 V, while sweeping the back-gate voltage, the device changes from balanced, ambipolar transistor behavior to strong p-type conduction, which indicates the enhancement of p-type contact when applying a favorable negative ionic liquid gate voltage. This effect is also shown in the I-V curves with different ionic liquid gate voltages at fixed V_{BG} = -75 V (see Fig. A-1 (b)). Compared to V_{IL} = 0, the linearity of I-V curve at V_{IL} = -3 V is greatly improved. This nearly ohmic contact rendered by high negative V_{IL} enables four-terminal resistivity and Hall measurements to extract contact resistance, intrinsic conductivity, and Hall mobility of this device. We note that all the measurements are done at a temperature $\sim$ 220 K, which is slightly above the freezing temperature

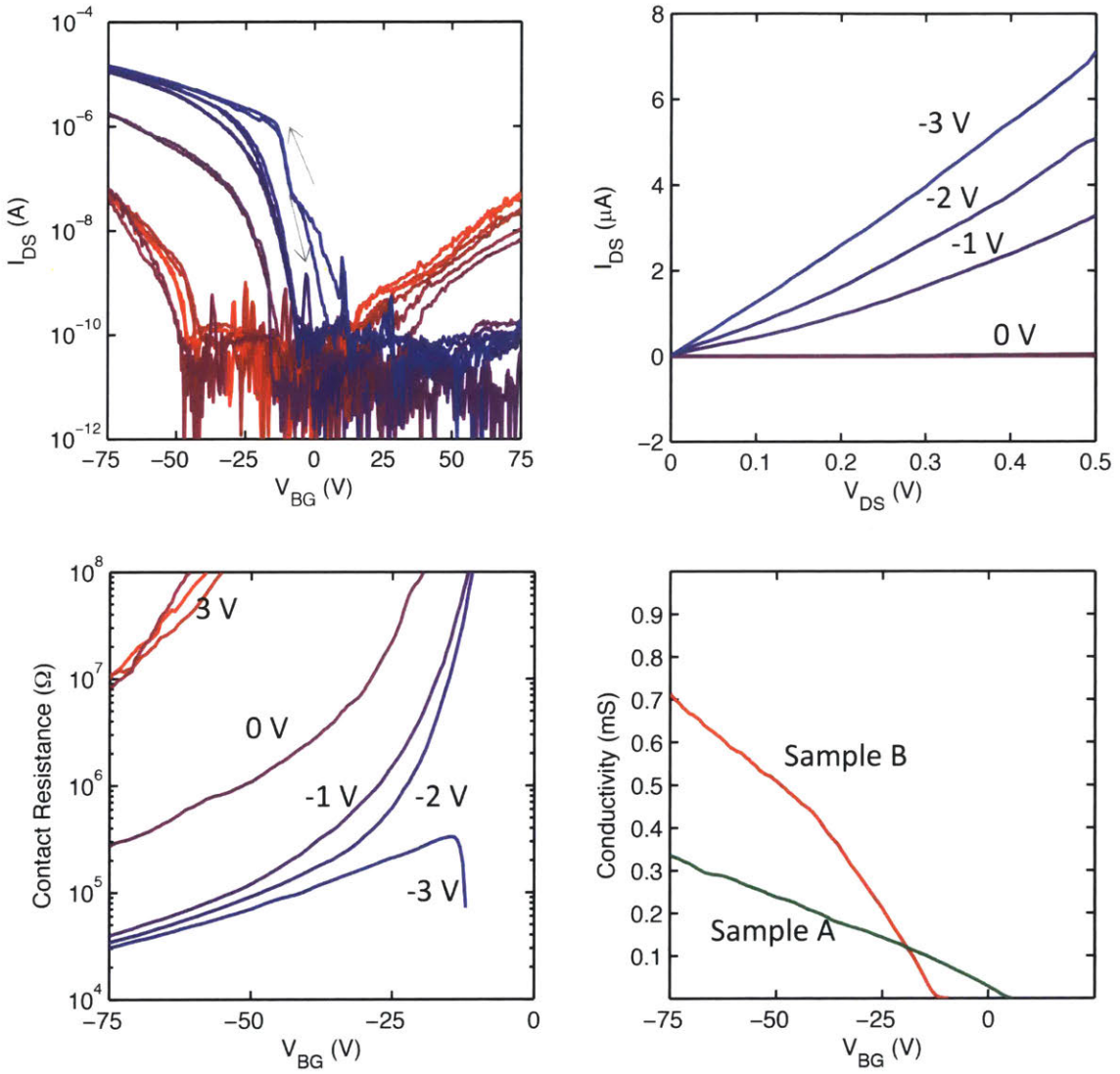

Figure A-1: Sample B: I_{DS} as a function of V_{BG} measured at different ionic liquid gate voltages: V_{IL} = -3, -2, -1, 0 V. V_{DS} = 0.5 V. (b) I_{DS} as a function of V_{DS} for the same set of V_{IL}, with fixed V_{BG} = -75 V. (c) Contact resistance as a function of V_{BG} of the WSe_2 device at different V_{IL}. (b) The comparison of conductivity of sample A and B as a function of V_{BG}, extracted from four-probe measurements with ionic liquid gate voltage configured for best performance of p-type contacts. The temperature for all measurements was 220 K.

of the liquid ($\sim$ 200 K) [164] to minimize chemical reactions between the ionic liquid and contact leads.

Based on four-terminal measurements, the contact resistance, R_c, is extracted from the resistivity as $R_c = V_{ds}/I_{ds} - \rho \cdot l/w$, where l and w are the full sample length and width, respectively, and $\rho = (V_{xx}/I_{ds})/(l_{in}/w)$, with l_{in} the length between the inner contacts. From V_{IL} = 3 V to -3 V, the contact resistance for V_{BG} = -75 V decreases by more than two orders of magnitude, which demonstrates the tunability of the contact resistance by the ionic liquid. We also plot conductivity as a function of V_{BG} for V_{IL} = -3 V compared with conductivity of sample A in Fig. A-1 (d).

Appendix B

TaS_2 Supplementary Information

Here we present supplementary information for Chapter 4.

B.1 Device fabrication

In our experiment, the sample fabrication process takes place in a glove box filled with Argon gas. 2H-TaS_2 crystals (from HQgraphene) are exfoliated onto Si/SiO_2 wafers inside the glovebox. The flake thickness is determined by atomic force microscope or optical contrast. We then build our device utilizing a polymer pick-up technique [147], taking advantage of the van der Waals adhesion between 2D materials.

hBN flakes that support bottom contacts is exfoliated onto Si/SiO_2 wafers. Wafers with hBN flakes are then annealed in Ar/H_2 atmosphere at 350 °C for 3 hours. Selected hBN flakes, with thickness ranging from 20 to 30 nm, are patterned with e-beam lithography using MMA/ZEP which serves as e-beam resist and etch mask for a XeF_2 etch. After development in o-xylene for 1 min and IPA:water solution (3:1) for 2 min (cooled in ice bath), hBN is then etched with XeF_2 gas for 20 s $\times$ 5 cycles. This is sufficient to etch all the hBN in the exposed channel. Then Cr/Pd 2/25 nm is evaporated by thermal or e-beam deposition. In this way, bottom contacts that are embeded in hBN are fabricated.

Polymer slides that are used to pick up exfoliated flakes and build 2D heterostructures are made in the following way: 1) A piece of polydimethylsiloxane (PDMS)

elastomer (1 mm × 1 mm square) is laid down on a glass slide. 2) A droplet of Poly(Bisphenol A carbonate) (PC, dissolved in chloroform 6% in weight) is dropped to a glass slide, and then forced to spread by pressing another glass slide on top. After left dry for about 10 min, a uniform thin film of PC is made. 3) The PC film is then transferred on top of PDMS and held in place with a double-sided tape.

Meanwhile, another hBN flake is exfoliated onto Piranha-cleaned SiO_2 and annealed in Ar/H_2 atmosphere at 350 °C for 3 hours. 2H-TaS_2 is exfoliated onto Piranha-cleaned SiO_2 inside the glove box. Using the polymer slide, hBN and 2H-TaS_2 can be picked up in sequence and transferred onto the bottom contacts. All the pick-up and transfer procedure takes place inside glove box. Such encapsulation allows for a van der Waals seal between two hBN flakes and therefore prohibits exposure to air during the transportation of device outside the glove box.

B.2 Superconductivity Properties

B.2.1 Superconductivity in 2D: BKT transitions

In 2D superconductors, when $d < \xi(0)$ and the lateral size is smaller than the in-plane magnetic penetration length ($\lambda_{ab} = \lambda^2/d$, estimated to be ~ 30 μm in thin-layer 2H-TaS_2, assuming $\lambda = 210$ nm and $d = 1.4$ nm [68]), the SC transition is expected to be of the Berezinskii-Kosterlitz-Thouless (BKT) type [74]. In BKT theory, when the temperature drops below the Bardeen-Cooper-Schrieffer (BCS) mean-field transition temperature T_c, a loss of global phase coherence and dissipation due to a finite flux resistance occur with thermally excited vortices. In this regime, a finite supercurrent can flow below the BKT transition temperature T_{BKT}, as a consequence of formation of bound vortex-antivortex pairs. Experimentally, T_{BKT} can be determined by analyzing the I-V characteristic curves at various temperatures, expected to manifest a universal relation $V \propto I^3$ when vortex-antivortex pairs dissociate. I-V analysis for bilayer ($T_c = 3$ K) and another trilayer ($T_c = 2.78$ K) samples is shown in Fig. B-1, where voltage obeys non-linear current dependence $V \propto I^\alpha$ during the BKT transi-

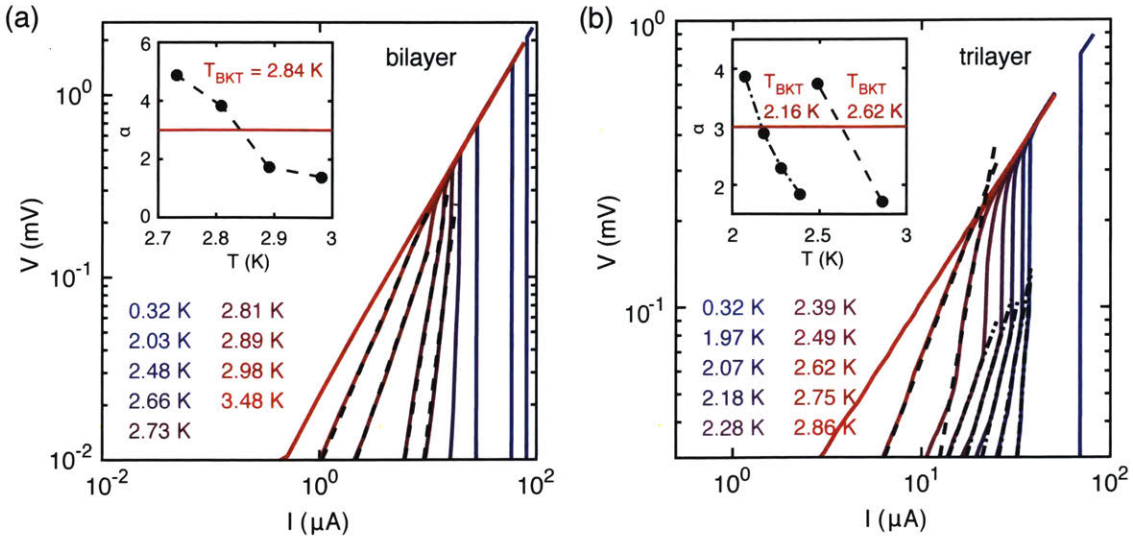

Figure B-1: Characterization of the BKT transition of (a) bilayer and (b) trilayer samples by measuring voltage-current behavior at various temperatures. Inset shows the exponent α versus T extracted from power-law fitting $V \propto I^{\alpha}$ near the BKT transition. The transition temperature T_{BKT} is obtained when the exponent α passes through 3.

tion. By plotting the voltage-current data in a log-log scale and fitting the slope to α, we can get α as a function of temperature (shown in inset of Fig. B-1). In this way, we estimate T_{BKT} as when α crosses the value of 3. T_{BKT} is found to be 2.8 K and 2.6 K for bilayer and trilayer respectively. They are close to and slightly lower than the BCS mean field T_c measured with $R(T)$ curves, which is also consistent with the BKT theory. Here we note that there might be inhomogeneity in this trilayer sample, which shows two sections of upturning voltages, possibly due to vortex pinning by a selected disordered region.

B.2.2 Critical current

In Fig. 4-3(d), it is remarkable that all the critical current data collapse into a single trace. By analysis of this curve, we observe that it clearly deviates from the Ginzburg-Landau (GL) theory [137], which predicts that J_c is proportional to $(1 - T/T_c)^{3/2}$. In addition, we compare our result with Bardeen's phenomenological expression [9] $J_c(T)/J_c(0) = (1 - (T/T_c)^2)^{3/2}$ (dotted line in Fig. 4-3(d)), which is an approxima-

tion of numerical calculations based on dirty-limit microscopic theory that extends the GL theory to low temperatures. There is still a discrepancy between our result and Bardeen's model. Ambegaokar and Baratoff [5] then proposed that if the system comprises of superconducting grains connected with an insulating region, the maximum dc Josephson current is expressed as

$$I_0(T) = [\pi\Delta(T)/2eR_N]\tanh(\Delta(T)/2k_BT), \tag{B.1}$$

where $\Delta(T)$ is the temperature-dependent BCS gap parameter and R_N is the normal-state tunneling resistance of a junction. Among the aforementioned models, Ambegaokar-Baratoff model fits best with our experimental data.

B.2.3 Residual resistance ratio, coherence length and mean free path

When the temperature is further decreased, a clear superconductivity (SC) transition is ubiquitously observed for all the samples and resistance is dropped to zero to the limit of our instrument resolution. A typical source current we apply is between 100 nA to 1 μA, which corresponds to current density of a few kA/cm^2. The residual resistance ratio (RRR) is found to generally decrease when the thickness is reduced, from RRR $\sim$ 22 for bulk to RRR $\sim$ 6 for bilayer. The sheet resistance in the normal-state right above the superconducting transition temperature ranges from 120 Ω to 0.4 Ω, and generally decreases when the sample gets thicker. These values lie far below the quantum resistance for Cooper pairs R_0 ($= h/4e^2 = 6.45$ kΩ), which verifies our samples to be in the low-disorder regime.

Shown in Fig. B-2 we plot the R-T curves near the SC transition for 2, 3, 5-layer samples under different perpendicular magnetic field. From this plot, we could obtain the H_{c2} as a function of temperature for 2, 3, 5-layer samples that is shown in Fig. 1 (d) in main text. The corresponding GL coherence length is $\xi_{ab}(0) =$ 19, 20, 26 nm. Here we need to note that the trilayer sample shown in Fig. B-2 (b) displays a clear two-step SC transition at 3 K and 2.5 K. This multi-step transition

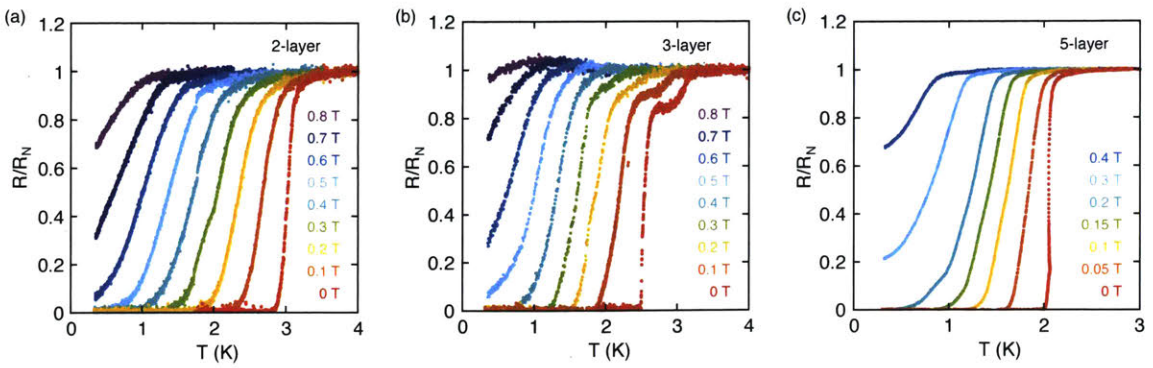

Figure B-2: Resistance normalized by the normal state (R/R_N) as a function of temperature at different perpendicular magnetic fields for (a) 2-layer, (b) 3-layer, (c) 5-layer samples near the SC transition.

is absent in the other trilayer device, as well as the 2, 5, 7-layer and bulk devices, therefore its origin cannot be intrinsic. We speculate that the sample thickness is not entirely homogeneous and there exists a small bilayer region, which leads to the initial superconducting transition at 3 K, which coincides with the measured T_c for bilayer. In addition, we observe a extremely large in-plane upper critical field $H_{c2}^{\parallel} = 31.2$ T. The anisotropy ratio for bilayer 2H-TaS_2 can be derived as $\gamma = H_{c2}^{\parallel}/H_{c2}^{\perp} \sim 39$.

The estimation of mean free path in ultra-thin samples is not as straightforward. It has been shown that determination of carrier density by Hall measurement is difficult due to the presence of both electrons and holes in different concentrations and with very different mobilities. For moderate magnetic field, the Hall coefficient takes the form $R_H = (p\mu_h^2 - n\mu_e^2)/e(p\mu_h + n\mu_e)^2$, where n and p are the electron and hole concentration, μ_e and μ_h are the electron and hole mobility, and e is the elementary charge. The negative sign for the Seebeck coefficient combined with the positive Hall coefficient measured in bulk crystal at room temperature suggests that the number of electrons is greater than the number of holes but with the hole mobility larger than the electron mobility. If we adhere to a single-carrier model, the number of holes in the bilayer sample calculated from R_H is $n = 3.8 \times 10^{22}$ cm^{-3}. It corresponds to hole density of approximately 1.3×10^{15} cm^{-2} per layer. This value far exceeds the atomic density of Ta in TaS_2 and hence is too large. Without an estimation of carrier concentration, it is difficult to estimate mean free path using a Drude-model

relation. Alternatively, we use Boltzmann transport in 2D within the relaxation time approximation at zero frequency to give a rough estimation of the mean free path. In Boltzmann transport equation (in 2D),

$$\sigma_{xx} = \frac{e^2\tau}{2}\int v_k^2 \delta(\epsilon - \epsilon_F)\mathrm{d}n \tag{B.2}$$

$$= \frac{1}{2}e^2\tau v_F^2 D(\epsilon_F) \tag{B.3}$$

In bilayer, we derive $\tau = 6\times10^{-14}$ s, assuming $D(\epsilon_F) = 2.556$ /eV/f.u., $v_F = 2.54\times10^5$ m/s (or $\hbar v_F = 1.67$ eV Å) calculated by DFT for bilayer in the normal phase. This corresponds to mean free path $l_{mfp} = 15.3$ nm.

From the Faber-Pippard ratio, the coherence length is found to be $\xi_{BCS} = 0.18\hbar v_F/k_B T_c = 116$ nm for bilayer in the normal phase. The zero-temperature coherence length ξ can have two forms depending on whether the superconductor is in the clean ($\xi \gg l_{mfp}$) or dirty ($\xi \ll l_{mfp}$) limits, and depends on dimensionality D = 1, 2, 3:

$$\xi_{clean} = 0.74\xi_{BCS}\sqrt{\frac{3}{D}}$$

$$\xi_{dirty} = 0.85\sqrt{\xi_{BCS}l_{mfp}}\sqrt{\frac{3}{D}}$$

In our case, $\xi_{BCS} \ll l_{mfp}$, hence the coherence length of bilayer is approximately $\xi_{dirty} = 43.8$ nm. This value is still twice of the experimental value measured for the bilayer sample. Here we need to note that the above analysis is based on a simple model assuming a single band with isotropic v_F. This is clearly not the case in our material. Besides, there are a number of factors not considered. For example, if the couplings are strong, the coherence length can be much shorter than theoretical value [16]. Also, a multi-band superconductor with spin-orbit coupling can exhibit shorter coherence length [53]. Here we also listed the average Fermi velocity for all the cases from our calculation: $\hbar v_F = 1.61$ eV Å (normal phase) and 1.53 eV Å (CDW phase) for monolayer, and $\hbar v_F = 1.77$ eV Å (normal phase) and 1.13 eV Å (CDW phase) for bulk.

B.3 Characterization of monolayer

The degradation of monolayer samples usually forbids any etching method to shape the flake or separate it from adjacent thicker pieces, which creates significant difficulty in terms of sample fabrication. Monolayer is also more fragile and easy to break during pick-up process, especially when it is attached to thicker flakes, so that the van der Waals interaction between the top h-BN and the monolayer flake becomes even weaker due to the uneven 2H-TaS_2 surface. Therefore the method that we use to fabricate the monolayer device is slightly modified according to what is used for other samples. First, we use the PC slide to directly pick up the targeted flake instead of using a top h-BN, which ensures more uniform adhesion between the PC and the TaS_2 flake. Second, to maintain minimum exposure to air, we seal the chip carrier with a glass coverslip inside glove box, before transferring the device out to measurement setup.

Fig. B-3 (a) shows the optical image of the monolayer flake that is used to build the monolayer device, and an overlay with the optical image of the completed device is shown in Fig. B-3 (b), in order to better illustrate where the monolayer region is located. It is seen that the monolayer is connected to adjacent flakes with different thickness. This is responsible for the multiple steps in the temperature dependence of the resistance during the superconducting transition of the monolayer deivice shown in Fig. 1(b).

We associate the multiple T_c with different regions of the flake. To determine the T_c of the monolayer region, we perform a differential resistance measurement. We apply a small AC signal superimposed on a DC bias and measure the dV/dI using a lock-in amplifier. Fig. B-3 (c) shows a 2D color plot of the differential resistance dV/dI versus DC bias current and temperature. It is seen that zero bias dV/dI starts to drop at around 3.5 K, which is consistent with previous measurement on temperature dependence of resistance. When the density of current flowing through a certain area exceeds the critical value, superconductivity gets destroyed in that region, which results in a peak in dV/dI signal. From the color plot, we can clearly observe multiple peaks in dV/dI map. Using curve of J_c as a function of T/T_c obtained in

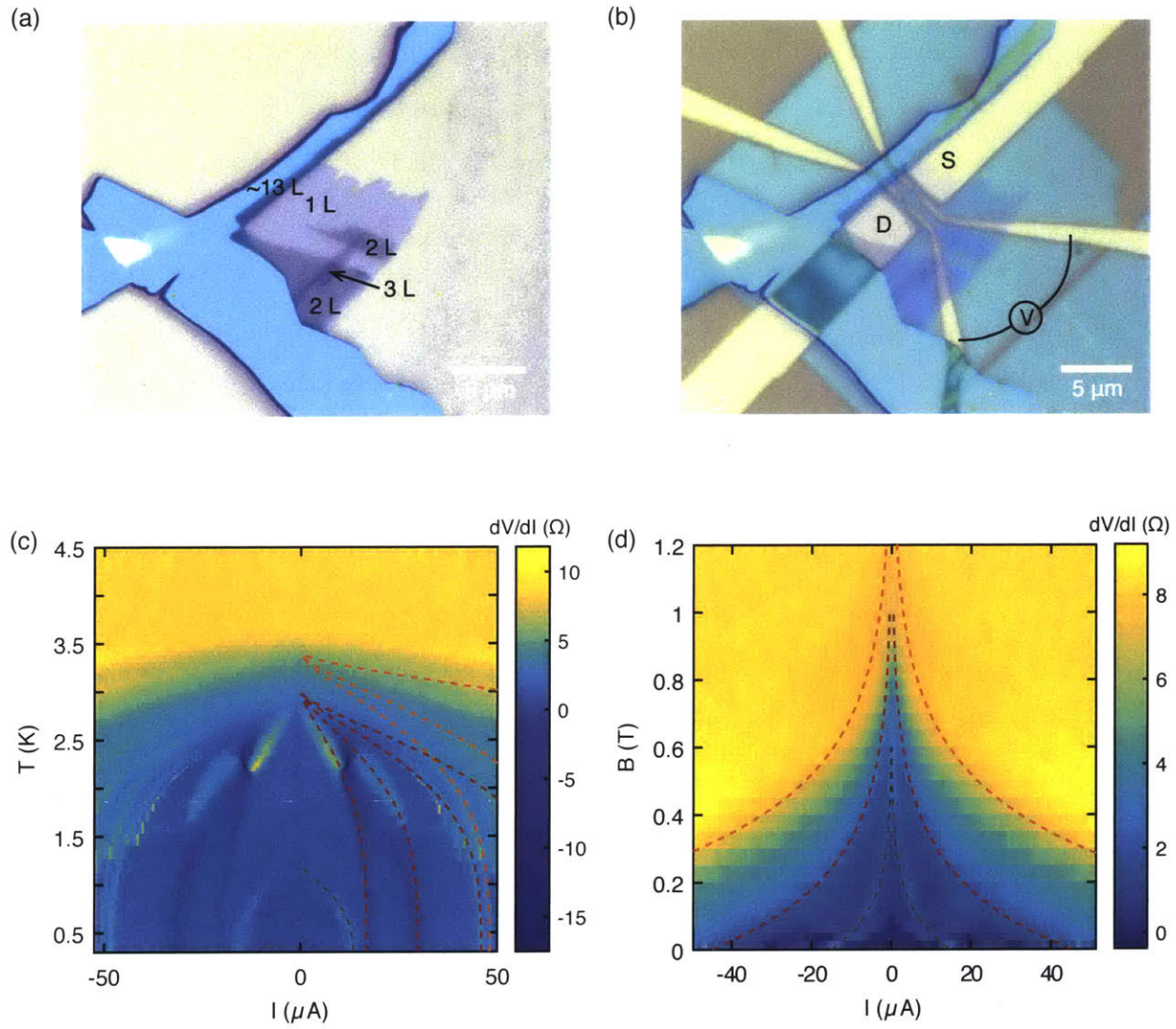

Figure B-3: (a) Optical image of the monolayer measured. The scale bar is 5 μm. (b) Overlay of the optical image of the monolayer flake and the metal bottom contacts. The scale bar is 5 μm. (c) Colormap of differential resistance dV/dI as a function of temperature and DC bias current. dV/dI manifests various peaks associated with different SC transition T_c. The dashed lines are fit of the dV/dI peaks to the J_c vs. T/T_c curve derived from Fig. 1 (e) in main text. T_c = 3.4, 3.0 and 1.3 K for orange, red and grey lines respectively. (d) Critical current colormap as a function of perpendicular magnetic field that manifests various dV/dI peaks associated with different H_{c2}. The dashed lines are drawn as guide to the eye.

the last session, we could fit these peak with three temperatures: T_c = 3.4, 3.0 and 1.3 K. This result identifies the transition temperature of the monolayer to be 3.4 K, which is consistent with the Aslamazov-Larkin fitting shown in main text. T_c = 3 K corresponds to superconducting transition temperature of the small bilayer region. T_c = 1.3 K can be ascribed to the thick region with thickness of $\sim$ 13 layers. This value also lies between 0.9 K and 1.6 K observed for bulk and 7-layer, respectively, consistent with our finding that the T_c increases monotonically as thickness is reduced. Here we note that for T_c = 3.4 and 3.0 K, critical current with multiple $J_c(0)$ is observed, which is likely due to the thickness inhomogeneity and existence of various parallel current paths on different regions.

B.4 DFT calculations

B.4.1 Electronic band structure for pristine crystals

2H-TaS_2 and the TMD family exhibit a trigonal prismatic structure, in which the Ta atoms in all the layers are aligned vertically but the S sublattice is rotated by 60° with respect to that of the neighboring layer. In the simplest monolayer structure with spin-orbit coupling, the relevant group of bands near the Fermi level are 22 bands that are mostly composed of the d orbitals of Ta atoms and the p orbitals of S atoms. Thus, we include all these relevant p-d orbital hybrids in deriving the Wannier tight-binding Hamiltonians. Due to the broken inversion symmetry, spin splitting in the bands from spin-orbit coupling is present at generic k points. To give the essential physics picture and elucidate the features in the electronic structure, here we provide more electronic structure details for the pristine monolayer, bilayer and bulk crystals. In Fig. B-4, we summarize the band plots along Γ-K-M-Γ, density of states and the energy contour at the Fermi energy. We find that the Fermi contour and the DOS at the Fermi level in the monolayer are not very different from the bulk case. Therefore band structure modification due to reduction of dimensionality itself cannot result in the enhancement of T_c. More details and numerical implementations can be found in

the Supplemental Material.

B.4.2 Electronic band structure unfolding

The CDW phase leads to a deformed crystal lattice as shown in Fig. 4-4(a) with 3×3 periodicity, whose band structure can be plotted in a supercell Brillouin zone. It can be viewed as the "folded" bands from the original bands of the pristine crystal. We describe here the details for the reverse "unfolding" procedure [77, 45, 87], which aims to present the CDW effects as perturbation on the pristine band structure.

When the primitive unit cell in real space is enlarged to the supercell, the corresponding Brillouin zone (BZ) in the reciprocal space is shrink to the supercell Brillouin zone (sBZ). In Fig. B-5(a), we compare in reciprocal space the original BZ (red hexagon) and the sBZ (blue hexagons) in the repeated zone scheme. We use $\vec{a}_i$ to denote the primitive vectors of the original 1×1 unit cell, and $\vec{a}_i^{\mathrm{SC}} = 3\vec{a}_i$ for the 3×3 supercell primitive vectors. The corresponding reciprocal lattice vectors are $\vec{G}_i$ and $\vec{G}_i^{\mathrm{SC}} = \vec{G}_i/3$. The area of one original BZ contains nine sBZ. Suppose the crystal momentum $\vec{k}^{\mathrm{SC}}$ lies within sBZ, any crystal momentum $\vec{k} = \vec{k}^{\mathrm{SC}} + p_1\vec{G}_1^{\mathrm{SC}} + p_2\vec{G}_2^{\mathrm{SC}}$ with integers p_i in original BZ would be classified as the same $\vec{k}^{\mathrm{SC}}$ in the sBZ (repeated zone). This can be seen from the Bloch theorem derived from the translational symmetry under the supercell translation vectors $\vec{T}^{\mathrm{SC}} = m_1\vec{a}_1^{\mathrm{SC}} + m_2\vec{a}_2^{\mathrm{SC}}$ with integers m_i.

$$e^{i\vec{k}\cdot\vec{T}^{\mathrm{SC}}} = e^{i(\vec{k}^{\mathrm{SC}} + p_1\vec{G}_1^{\mathrm{SC}} + p_2\vec{G}_2^{\mathrm{SC}})\cdot(m_1\vec{a}_1^{\mathrm{SC}} + m_2\vec{a}_2^{\mathrm{SC}})} \tag{B.4}$$

$$= e^{i\vec{k}^{\mathrm{SC}}\cdot(m_1\vec{a}_1^{\mathrm{SC}} + m_2\vec{a}_2^{\mathrm{SC}})} \tag{B.5}$$

$$= e^{i\vec{k}^{\mathrm{SC}}\cdot\vec{T}^{\mathrm{SC}}} \tag{B.6}$$

for distinct p_i integers. Various crystal momentum states in the original 1×1 unit cell description are thus mapped onto the "folded" $\vec{k}^{\mathrm{SC}}$ crystal momentum label in the supercell description. The perturbation from CDW deformation introduces coupling and mixing between these momentum states. Because the states and bands are folded in the sBZ, for each $\vec{k}^{\mathrm{SC}}$ there are nine times the number of bands in the sBZ than

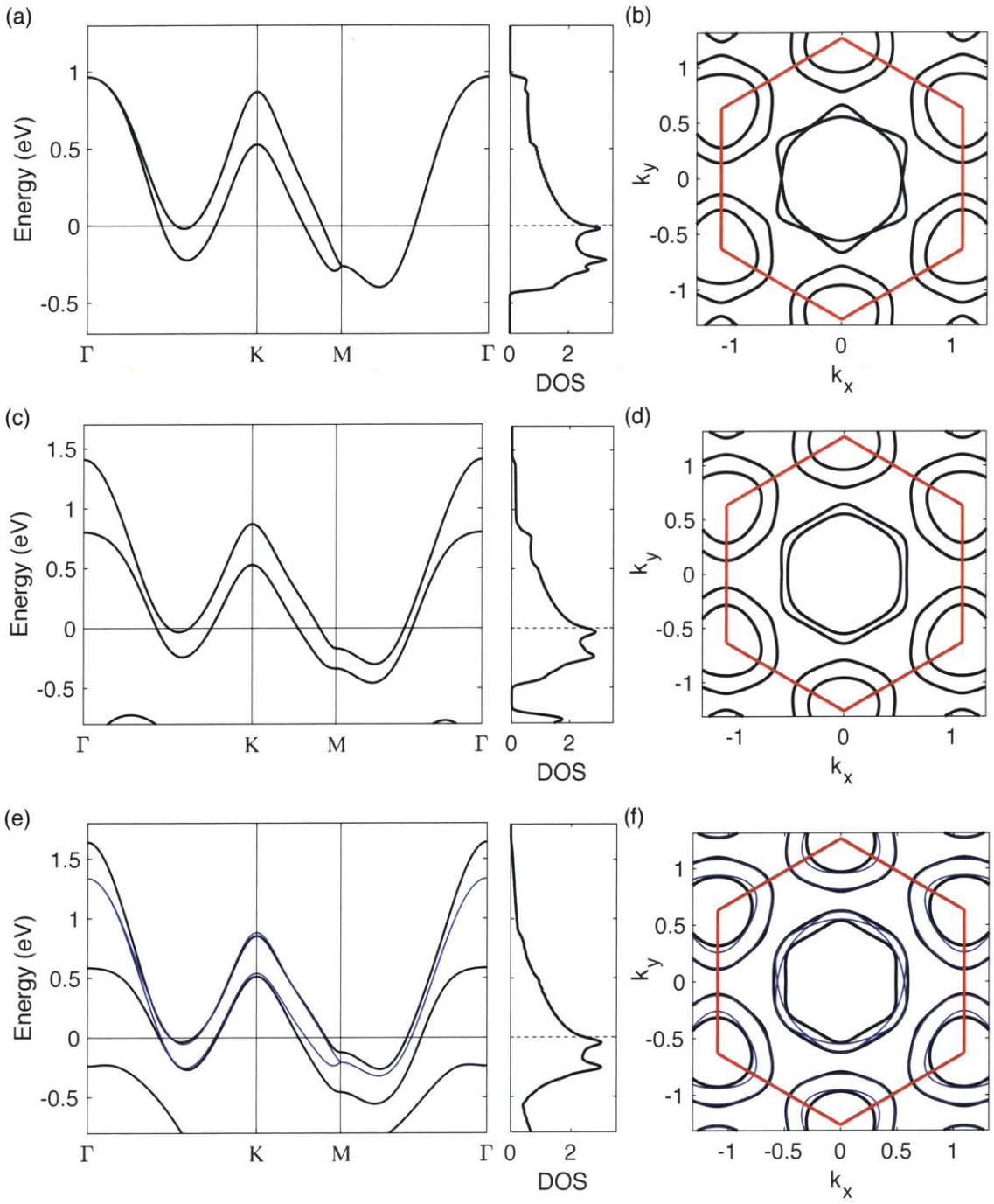

Figure B-4: Electronic band structure with spin-orbit coupling along Γ-K-M-Γ and the corresponding density of states (number of electrons/eV/f.u.) for TaS_2 crystals of the (a) monolayer, (c) bilayer, (e) bulk form (black lines for $k_z = 0$ and thinner blue lines for $k_z = \pi$). The density of states here contains contributions from all bands. The corresponding energy contour at the Fermi level with Brillouin zone delineated by the red hexagon for the: (b) monolayer, (d) bilayer, (f) bulk cases (the black thick lines are the energy contours with $k_z = 0$ while the thinner blue lines are for contours with $k_z = \pi$).

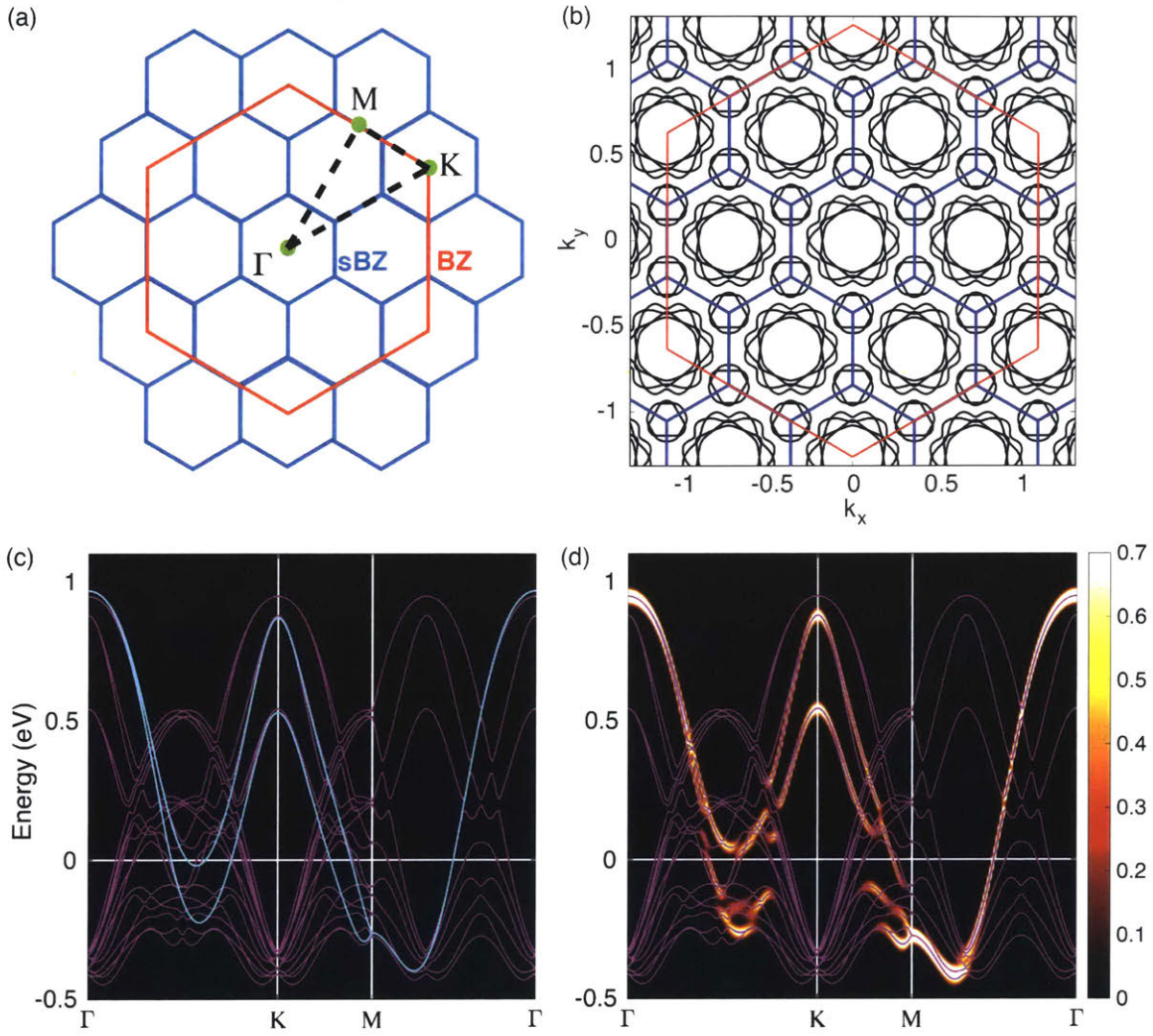

Figure B-5: CDW-ordered monolayer electronic band structure, the folding effects from the supercell geometry and the inverse unfolding process. (a) BZ (red hexagon) and sBZ (blue hexagons) in the repeated zone. (b) Energy contour of the CDW-ordered monolayer crystal in the repeated zone scheme (contrast with the ones for the pristine crystal without CDW order in Fig. B-4). (c) Folded CDW band structure (magenta) along Γ-K-M-Γ as outlined in (a). For comparison, bands from the pristine crystal without CDW order in 1×1 unit cell are also plotted (cyan). (d) Folded supercell bands (magenta) compared with the unfolded and weighted effective bands. The unfolded effective bands differ from the pristine electronic band structure by additional features such as gap opening from CDW perturbations (as in Fig. 4-6(a)). The Fermi level is indicated by the white horizontal line. When the CDW energy contour in (b) is decorated with the unfolding weight as the band structure, the unfolded CDW energy contour is obtained in Fig. 4-6(d).

the original BZ description. In the repeated sBZ scheme, the energy contour at Fermi energy for the monolayer with CDW is shown in Fig. B-5(b). The topography of the energy contour from the band folding is substantially more complicated than that of the pristine crystal without CDW, shown in Fig. B-4. The band structure in Fig. B-5(c) along the momentum line as in Fig. B-5(a) also shows the supercell bands that are drastically different from the ones of the pristine crystal.

As shown in Fig. B-4, the band folding can be traced back to the associated phase factor and the crystal momentum of the Bloch theorem. Within the supercell description, the crystal momentum $\vec{k}^{\mathrm{SC}}$ is defined under the supercell translation $\vec{T}^{\mathrm{SC}}$. As a result, the translational properties under the smaller original primitive vectors are not resolved with the $\vec{k}^{\mathrm{SC}}$ supercell crystal momentum labeling. Any state with $\vec{k} = \vec{k}^{\mathrm{SC}} + p_1\vec{G}_1^{\mathrm{SC}} + p_2\vec{G}_2^{\mathrm{SC}}$ (original crystal momentum defined with translation $\vec{T}$ spanned by primitive vector $\vec{a}_i$) is compatible with the supercell crystal momentum $\vec{k}^{\mathrm{SC}}$, with the same reasoning as in Eq. B.4. However in many cases such as CDW order, there is weak translational symmetry breaking, and the translational symmetry for the 1×1 unit cell can be treated as the approximate symmetry of the crystal. That is, we can decompose a supercell Bloch state or an energy eigenstate at $\vec{k}^{\mathrm{SC}}$ into components with distinct translational properties under the original $\vec{T}$ and label them with $\vec{k} = \vec{k}^{\mathrm{SC}} + q_1\vec{G}_1^{\mathrm{SC}} + q_2\vec{G}_2^{\mathrm{SC}}$:

$$\psi_{\vec{k}}^{\mathrm{SC}} = \sum_{\vec{k}'=\vec{k}+p_1\vec{G}_1^{\mathrm{SC}}+p_2\vec{G}_2^{\mathrm{SC}}} \psi_{\vec{k}'} \tag{B.7}$$

which has nine components in the 3×3 supercell. In the perturbative regime, we can start with the pristine crystal without CDW order and the translational symmetry under $\vec{T}$ is recovered. This translation symmetry eliminates the mixings between distinct $\vec{k}'$ components classified under the same supercell $\vec{k}^{\mathrm{SC}}$. CDW order breaks the $\vec{T}$ translation symmetry and induces mixing between $\vec{k}'$ components. To compare and contrast with the original pristine crystal band structure in the repeated zone scheme, the $\psi_{\vec{k}'=\vec{k}}$ component is singled out and the unfolding weight for the state is defined as the norm of this specific component $|\psi_{\vec{k}'}|^2$. When the supercell band

structure is plotted with the unfolding weight for each state as in Fig. B-5(d), the band structure with weights is greatly simplified and they are defined as the unfolded band structure. These unfolded and weighted bands are then compared with the pristine bands without CDW in Fig. 4-6(a). Clearly, these unfolded CDW bands introduce additional electronic features to the pristine band structure such as the splittings and the gap opening from CDW order. The same unfolding procedure can also be applied to the Fermi energy contour change due to CDW as in Fig. 4-6(d).

The unfolded band structure can be compared with the band structure from the angle-resolved photoemission spectroscopy (ARPES) measurements. The same unfolding scheme can also be applied to the cases of impurities in the crystal [118] or disordered solids [123], and Fe-based high-temperature superconductors [87]. When the perturbation terms in these cases are added to the system gradually, the unfolded bands with weights also change perturbatively from the original ones. The effective band structures are a more natural and intuitive way of generalizing the conventional band structure and comparing with experiment in these cases even though the translation symmetries of the primitive cell are broken.

B.4.3 Phonon dispersion

For TaS_2 crystals, the phonon properties are calculated within density functional perturbation theory (DFPT), using VASP code with the phonopy package [138]. A $6 \times 6 \times 2$ ($8 \times 8 \times 1$) supercell geometry is employed for the bulk (monolayer) crystal, with the calculated phonon spectrum and the density of states shown in Fig. 4-5. We find that the average phonon frequency slightly decreases for the monolayer case, with squared phonon frequency $\langle \omega^2 \rangle$ change from 58.12 THz^2 in bulk to 56.59 THz^2 in monolayer.

B.5 T^2 Behavior and Scattering by phonons

In this section we elaborate on the theory for the low temperature resistivity in TaS_2. Shown in Fig. B-6 (a) is a zoom-in of the resistivity plot for 2, 3, 5, 7-layer and

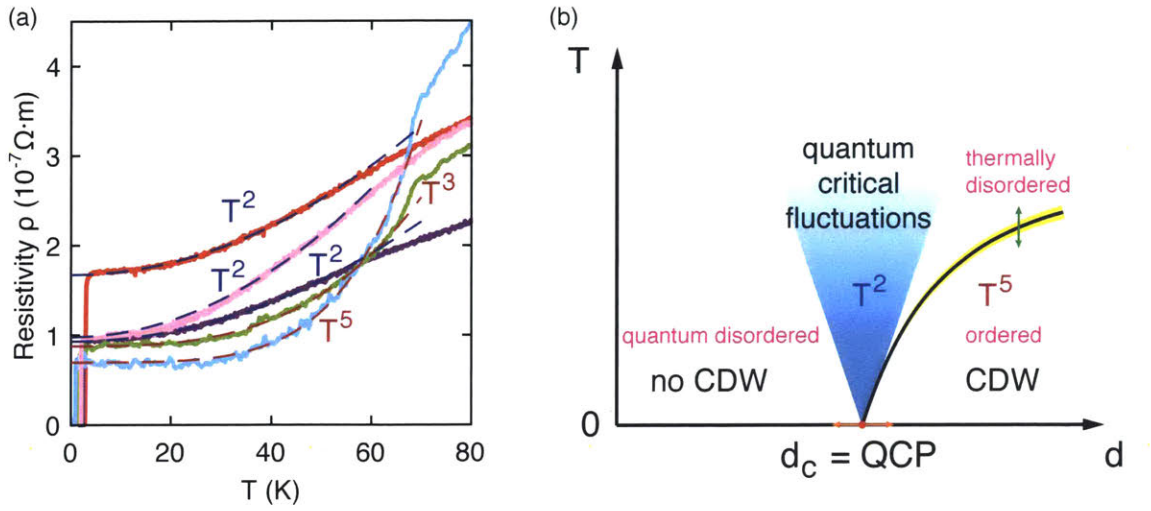

Figure B-6: (a) Resistivity as a function of temperature below 80 K for 2, 3, 5, 7-layer and bulk. (b) Illustration of the quantum critical fan. A quantum critical point is located at critical thickness d_c, where CDW order disappears.

bulk. The T^5 and T^3 behavior observed in bulk and 7-layer sample is attributable to electron-phonon intraband and interband scattering. In this plot, it is clear that 2, 3-layer manifest a T^2 behavior from $\sim$ 55 K down to the onset temperature of SC. The R(T) curve for 5-layer cannot be fitted to a single power law, and it deviate from T^2 at low temperatures. It has been well established in Fermi liquid theory that electron-electron (e-e) scattering leads to $\rho = AT^2$. However, the prefactor A for our ultra-thin samples is very large. For example, A is found to be 3×10^{-9} Ω cm/K^2 for bilayer sample, which is approximately two orders of magnitude larger than that of transitional metals [143]. In addition, we calculate A/γ^2 of the bilayer sample, known as the Kadowaki-Woods ratio (γ: electron heat capacity, $\sim$ 8.5 mJ/mol K^2 for bulk 2H-TaS_2), is also very large, comparable to Kadowaki-Woods ratio measured in heavy fermion and strongly-correlated materials [63]. In general, the large coefficient in heavy fermions reflects the narrow band width and strong correlations in those systems, which is unlikely the case in TMDs. Therefore, we switch to scenario of electron-phonon scattering to explain the low temperature resistivity in TaS_2. We first review the well known result for phonon scattering using Ziman's variational technique [176]. We then use the same machinery to discuss the situation where the dispersion softens at some finite point in the Brillouin zone $\boldsymbol{q} = \boldsymbol{Q}$.

B.5.1 Acoustic phonon scattering – review of the well known result

The resistivity can be calculated by the variational principle, which states that the solution of the Boltzman equation minimizes the excess entropy due to the deviation from equilibrium distribution. Then the resistivity is bound from above by the ratio of the entropy and the square of the current (see for example the book by Ziman)

$$\rho = \frac{1}{J^2 T} \sum_{\boldsymbol{k},\boldsymbol{k}',\boldsymbol{q}} (\Phi_{\boldsymbol{k}} - \Phi_{\boldsymbol{k}'})^2 \mathcal{P}_{\boldsymbol{k}\boldsymbol{q}}^{\boldsymbol{k}'} \tag{B.8}$$

Here

$$\boldsymbol{J} = -e \int \frac{d^d k}{(2\pi)^d} \frac{f_{\boldsymbol{k}}^0 (1 - f_{\boldsymbol{k}}^0)}{T} \Phi_{\boldsymbol{k}} \boldsymbol{v}_{\boldsymbol{k}}$$

is the total current, $\mathcal{P}_i^j$ is the transition rate from states i to j and Φ_k is the deviation from equilibrium distribution of the electrons defined in the following manner

$$f_{\boldsymbol{k}} = f_{\boldsymbol{k}}^0 + \frac{f_{\boldsymbol{k}}^0 (1 - f_{\boldsymbol{k}}^0)}{T} \Phi_{\boldsymbol{k}}$$

where $f_{\boldsymbol{k}}^0$ is the Fermi-Dirac distribution. It is important to note that in within Eq. (B.8) we have neglected the phonon drag by assuming that they remain in thermal equilibrium throughout. This is also the reason that the resistivity from phonons can still be finite despite the conservation of momentum that will be enforced in the calculation. Thus, in principle, the phonon gas is absorbing momentum, but by assuming that the distribution remains in equilibrium we have assumed that they loose momentum to the crystal defects and boundaries on a time scale which is much shorter than the time it takes electrons to lose momentum to the phonons.

The transition rate is given by

$$\mathcal{P}_{\boldsymbol{k}}^{\boldsymbol{k}'\boldsymbol{q}} = \frac{2\pi}{\omega_{\boldsymbol{q}}} |g_{\boldsymbol{q}}|^2 \delta(\boldsymbol{k} - \boldsymbol{k}' + \boldsymbol{q}) \delta(\epsilon_{\boldsymbol{k}} - \epsilon_{\boldsymbol{k}'} + \omega_{\boldsymbol{q}}) n_{\boldsymbol{q}}^0 f_{\boldsymbol{k}}^0 (1 - f_{\boldsymbol{k}'}^0) \tag{B.9}$$

where $n_{\boldsymbol{q}}^0$ is the Bose distribution function, $\epsilon_{\boldsymbol{k}} = k^2/2m - \epsilon_F$ and $\omega_{\boldsymbol{q}} = u|\boldsymbol{q}|$ are the electron and phonon dispersions. Notice the conservation of total energy and

momentum. (We have neglected umklapp process in the phonon scattering.) $g_{\boldsymbol{q}}$ is the electron phonon coupling, which in the case of *longitudinal* acoustic phonons takes the form $g_{\boldsymbol{q}} = -i\lambda|\boldsymbol{q}|$. The units of λ are given by $[\lambda] = Energy \times Length^{d/2}/Mass^{d/2}$, which follows from $\lambda = D/\sqrt{\rho_m}$, where D is the deformation potential and ρ_m is the crystal mass density.

To proceed we use the standard ansatz for the deviation from equilibrium distribution

$$\Phi_{\boldsymbol{k}} = \boldsymbol{c} \cdot \boldsymbol{k}\,, \tag{B.10}$$

where $\boldsymbol{c}$ points along the direction of the current. The magnitude of the current is then given by

$$J = \frac{e k_F^d c}{2d\pi^{d-1}} \tag{B.11}$$

Now to compute the resistivity we perform the integration over the three momenta $\boldsymbol{k}$, $\boldsymbol{k}'$ and $\boldsymbol{q}$. The latter is eliminated by the delta function, which sets $\boldsymbol{q} = \boldsymbol{k}' - \boldsymbol{k}$, and thus also $(\Phi_{\boldsymbol{k}} - \Phi_{\boldsymbol{k}'})^2 = \frac{1}{d}c^2q^2$. The magnitude of $\boldsymbol{k}'$ can also be eliminated by the conservation of energy delta function. Overall we get

$$\begin{aligned}\rho &= \frac{d\lambda^2}{2^{3(d-1)}\pi^{d+1}e^2k_F^2v_F^2T}\int d\Omega' \int d\Omega \int d\epsilon_{\boldsymbol{k}}\, \frac{q^4}{\omega_{\boldsymbol{q}}}\frac{1}{e^{\frac{\omega_{\boldsymbol{q}}}{T}}-1}\frac{1}{e^{\frac{\epsilon_{\boldsymbol{k}}}{T}}+1}\frac{1}{1+e^{-\frac{\omega_{\boldsymbol{q}}+\epsilon_{\boldsymbol{k}}}{T}}} \\ &= \frac{d\lambda^2}{2^{3(d-1)}\pi^{d+1}e^2k_F^2v_F^2T}\int d\Omega' \int d\Omega\; q^4 n^0_{\boldsymbol{q}}(1+n^0_{\boldsymbol{q}})\end{aligned} \tag{B.12}$$

where $d\Omega$ is an integral over a solid angle.

This is about as far as we can go without specifying the dimension. In three dimensions we can use the relation $q^2 = 2k_F^2\,(1-\cos\theta)$ to make a change of variables in the solid angle integration $d(\cos\theta) = -2qdq/k_F^2$, with limits of integration between 0 and $2k_F$

$$\rho_{3D} = \frac{3\lambda^2}{16\pi^3e^2k_F^4v_F^2T}\int_0^{2k_F} dq\; q^5 n^0_{\boldsymbol{q}}(1+n^0_{\boldsymbol{q}}) \tag{B.13}$$

From here it is already clear that at $T \to 0$ this gives a scaling T^5. By making a

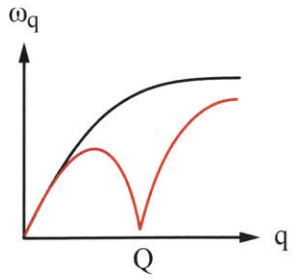

Figure B-7: Acoustic phonon dispersion in a TMDC along the ΓM direction. Black curve is the dispersion far from the CDW transition. Red is the softenining of the mode at $\boldsymbol{q} = \boldsymbol{Q}$.

change of variables $x = uq/T$, one gets

$$\rho_{3D} = \frac{6}{\pi^3}\frac{k_F\lambda^2}{e^2 v_F^2 u}\left(\frac{T}{\Theta}\right)^5 \int_0^{\frac{\Theta}{T}} dx\, x^5 \frac{1}{e^x - 1}\frac{1}{1-e^{-x}} \tag{B.14}$$

which in the limit of $T \ll \Theta$ gives T^5, where $\Theta = 2uk_F$.

Now let us move to two dimensions. In this case the change of variables gives $k_F\, d\theta = -2dq/\sqrt{2-(q/2k_F)^2}$, therefore we have

$$\begin{aligned}\rho_{2D} &= \frac{\lambda^2}{\pi^2 e^2 k_F^3 v_F^2 T}\int_0^{2k_F} dq\, \frac{q^4 n_{\boldsymbol{q}}^0(1-n_{\boldsymbol{q}}^0)}{\sqrt{2-(q/2k_F)^2}} \\ &= \frac{2^4}{\pi^2}\frac{k_F\lambda^2}{e^2 v_F^2 u}\left(\frac{T}{\Theta}\right)^4 \int_0^{\frac{\Theta}{T}} dx\, \frac{x^4}{\sqrt{2-(xT/\Theta)^2}}\frac{1}{e^x-1}\frac{1}{1-e^{-x}}\end{aligned} \tag{B.15}$$

In this case, the limit of $T \ll \Theta$ this function grows like T^4.

B.5.2 Scattering by a preformed charge density wave

We now turn to the situation in which the phonon branch becomes soft at some finite momentum (red curve in Fig. B-7)

$$\omega_{\boldsymbol{q}} = \sqrt{(u'|\boldsymbol{q}-\boldsymbol{Q}|)^2 + \Delta^2} \tag{B.16}$$

where Δ is the gap, which is assumed to be much smaller than the phonon band width, and $\boldsymbol{Q}$ is the momentum at which the phonon branch becomes soft. This can happen, for example, close to a CDW transition. The situation is very similar to that considered by Hlubina & Rice [61], and the resulting T^2 behavior follows. In what follows we apply their theory for the case of a soft phonon.

The dispersion Eq. (B.16) leads to strong electron-boson coupling in the vicinity of certain points on the Fermi surface, the so called "hot spots". These are points on the Fermi surface which are connected to each other by a momentum shift of $\boldsymbol{Q}$. These points will be the main focus of the calculation as they will dominate the resistivity, and therefore we will expand physical quantities in the vicinity of these points denoted by the angles of the hot spots on the Fermi surface θ_j, with $j = 1, 2, \ldots$

Before we continue we note that Eq. (B.12) can be generalized to account for scattering from a generic bosonic mode and using an arbitrary ansatz for the deviation from equilibrium, to give

$$\rho = \frac{dg_Q^2}{2^{3(d-1)}\pi^{d+1}e^2k_F^2v_F^2T}\int d\Omega' \int d\Omega \frac{(\Phi_{\boldsymbol{k}} - \Phi_{\boldsymbol{k}'})^2}{c^2} I(\omega_{\boldsymbol{q}}) \tag{B.17}$$

where g_Q is the coupling to the soft phonon in the vicinity of $\boldsymbol{Q}$, which is taken to be a constant with the units of λ times momentum. Here

$$I(\omega_{\boldsymbol{q}}) \equiv \int_0^\infty d\omega\, \omega\, n^0(\omega)[1 + n^0(\omega)]\, \mathrm{Im}\chi(\boldsymbol{q}, \omega)\,,$$

and $\chi_{\boldsymbol{q}}$ is the propagator (susceptibility) of the mode, which has the form

$$\chi(\boldsymbol{q}, \omega) = \frac{1}{\omega_{\boldsymbol{q}}^2 - \omega^2 - i\gamma\omega}\,.$$

Note that here we have added the damping γ. Unlike the acoustic phonon branch close to $q = 0$, this low energy part of the phonon spectrum is Landau damped by the Fermi surface. Moreover, since at low enough energy $\omega^2 < \gamma\omega$ we may neglect

the dynamical term, we will use the simpler form

$$\mathrm{Im}\chi(\boldsymbol{q},\omega) = \frac{\gamma\omega}{\omega_{\boldsymbol{q}}^4 + \gamma^2\omega^2} \tag{B.18}$$

We are now in position to compute the resistivity. We consider the simpler case of two dimensions

$$\begin{aligned}\rho_{2D} =& \frac{g_Q^2}{\pi^2 e^2 k_F^2 v_F^2 T}\int d\theta' \int d\theta \int_0^\infty d\omega \, \frac{(\Phi_{\boldsymbol{k}} - \Phi_{\boldsymbol{k}'})^2}{c^2} \frac{\gamma\omega^2}{\omega_{\boldsymbol{q}}^4 + \gamma^2\omega^2} n^0(\omega)[1 + n^0(\omega)] \\ \approx& \frac{g_Q^2 \gamma T^2}{3e^2 k_F^2 v_F^2}\int d\theta' \int d\theta \, \frac{(\Phi_{\boldsymbol{k}} - \Phi_{\boldsymbol{k}'})^2/c^2}{\omega_{\boldsymbol{q}}^2(\omega_{\boldsymbol{q}}^2 + \frac{2\pi\gamma T}{3})}\end{aligned} \tag{B.19}$$

The hotspots are effective when θ and θ' are located on opposite hot spots. Let us denote two hot spots of this sort by θ_1 and θ_2, such that θ will be expanded close to θ_1 and θ' near θ_2. It is also convenient to transform to relative and sum coordinates $\theta_\pm = \frac{\theta \pm \theta'}{2}$. When $\boldsymbol{Q} \parallel \boldsymbol{x}$ then the hot spot scenario is obtained when $\theta_+ = \pi/2$ and $\theta_- = \sin^{-1} Q/2k_F$. Thus, we expand around these points and define two new relative coordinates $\delta\theta_\pm$. The dispersion is then given by

$$\omega_{\boldsymbol{q}\approx\boldsymbol{Q}} = u' k_F \sqrt{(1-r^2)\delta\theta_-^2 + r^2\delta\theta_+^2} \tag{B.20}$$

where $r = Q^2/4k_F^2$. Thus, $\omega_{\boldsymbol{q}}$, scales linearly with $d\theta_\pm$. Thus, we have

$$\rho_{2D} \approx \frac{2g_Q^2\gamma T^2}{3e^2 k_F^2 v_F^2}\int d\theta_+ \int d\theta_- \, \frac{(\Phi_{\boldsymbol{k}} - \Phi_{\boldsymbol{k}'})^2/c^2}{\omega_{\boldsymbol{q}}^2(\omega_{\boldsymbol{q}}^2 + \frac{2\pi\gamma T}{3})}$$

A naive ansatz, as Eq. (B.10), clearly leads to a scaling which is $\omega_{\boldsymbol{q}} \sim \theta_\pm \sim \sqrt{T}$. A simple power counting gives $\rho \propto T$. However, this ansatz, is simply not a very good one and thus gives a bad bound. A better bound is obtained by cutting off (or short circuiting) the hot spots in the following manner [61]

$$\Phi_{\boldsymbol{k}} = \frac{ck_F \cos\theta}{e^{\beta(\delta - |\theta - \theta_{1,2}|)} + 1} \tag{B.21}$$

By setting $\beta \to \infty$ and taking $\delta \sim Q/k_F \gg \sqrt{T/\gamma}$, we find that the resistivity goes as

$$\rho_{2D} \approx \frac{4}{3} \frac{p}{r\sqrt{1-r^2}} \frac{g_Q^2}{\epsilon_F^2 u'^2} \frac{\gamma}{e^2} \left(\frac{T}{\Theta'}\right)^2 \tag{B.22}$$

where $\Theta' = 2u'k_F$ and p is the number of hot spot pairs that are connected by $\boldsymbol{Q}$. Thus, we find that $\rho \propto T^2$ due to scattering from the soft phonon mode. The same temperature dependence is also expected for 3D Fermi surfaces. Also note that $g_Q^2 = D^2/M$, where D is the deformation potential (of order 2 eV [47]) and M is the *effective* ion mass. Thus $g_Q^2/\epsilon_F^2 u'^2 \sim 1/W$, where W is the effective elastic constant in units of energy.

We point out a few important caveats. The first is that in obtaining (B.22) we have neglected disorder, which influences the power law dependence of ρ, as pointed out by Rosch [122]. The issue is that the ansatz (B.21) gives a lower bound on the resistivity only when the contribution (B.22) is significantly larger than the residual resistivity. In the opposite limit the best solution is actually given by Eq. (B.10) and the temperature dependence goes like $\rho \propto a + bT$.

The second caveat is that the mode is "soft" only if $\Delta < \min[\gamma, T]$. Otherwise the integral in Eq. (B.19) becomes exponentially suppressed, and we expect the standard T^4 Bloch law.

B.5.3 Umklapp e-e scattering in 2D

It is well known that another possible origin for $\rho \propto T^2$ is electron-electron scattering. In the previous calculation we assumed conservation of momentum, but once the momentum was dumped into the phonons we were not concerned how it is further lost to the crystal. Here this will become a crucial problem, where it will be essential that scattering processes generate a loss of momentum. Without disorder this is only allowed if the total momentum lost in the process is a reciprocal lattice vector $\boldsymbol{G}$, i.e. the process is umklapp.

We will again focus on the result in 2D, as the one in 3D is well known. The

Coulomb interaction in 2D is given by

$$V(q) = \frac{2\pi e^2}{q + q_{TF}} \tag{B.23}$$

where $q_{TF} = 2\pi e^2 N(0)$ is the Thomas-Fermi momentum.

The resistivity is then given by (see Ziman for example)

$$\rho = \frac{\pi}{4(2\pi)^{4d} T J^2} \int d^d k_1 d^d k_2 d^d k_3 d^d k_4 \left(\Phi_{\boldsymbol{k}_1} + \Phi_{\boldsymbol{k}_2} - \Phi_{\boldsymbol{k}_3} - \Phi_{\boldsymbol{k}_4}\right)^2 \mathcal{P}^{\boldsymbol{k}_3 \boldsymbol{k}_4}_{\boldsymbol{k}_1 \boldsymbol{k}_2} \tag{B.24}$$

where

$$\mathcal{P}^{\boldsymbol{k}_3 \boldsymbol{k}_4}_{\boldsymbol{k}_1 \boldsymbol{k}_2} = V^2(|\boldsymbol{k}_1 - \boldsymbol{k}_3|)\delta\left(\boldsymbol{k}_1 + \boldsymbol{k}_2 - \boldsymbol{k}_3 - \boldsymbol{k}_4 - \boldsymbol{G}\right)\delta(\xi + \xi') f^0_{\boldsymbol{k}_1} f^0_{\boldsymbol{k}_2} (1 - f^0_{\boldsymbol{k}_3})(1 - f^0_{\boldsymbol{k}_4})$$

Here $\xi = \epsilon_{\boldsymbol{k}_4} - \epsilon_{\boldsymbol{k}_1}$, $\xi' = \epsilon_{\boldsymbol{k}_3} - \epsilon_{\boldsymbol{k}_2}$ and $\boldsymbol{G}$ is a reciprocal lattice vector.

In principle there should be a sum over vectors $\boldsymbol{G}$, however, two particle collisions can only scatter from one Brioullin zone to its nearest neighbours. Thus, we will consider a single $\boldsymbol{G}$ process, which is a fundamental reciprocal lattice vector of the order of $2k_F$. Using the standard ansatz (B.10), then momentum conservation integral leads to $\Phi_{\boldsymbol{k}_1} + \Phi_{\boldsymbol{k}_2} - \Phi_{\boldsymbol{k}_3} - \Phi_{\boldsymbol{k}_4} = \boldsymbol{c} \cdot \boldsymbol{G}$

$$\begin{aligned}
\rho &= \frac{\pi G^2 T^2}{4(2\pi)^8 e^2 v_F^4} \int d\theta_1 d\theta_2 d\theta_3 d\theta_4 \delta\left(\boldsymbol{k}_1 + \boldsymbol{k}_2 - \boldsymbol{k}_3 - \boldsymbol{k}_4 - \boldsymbol{G}\right) V^2(|\boldsymbol{k}_1 - \boldsymbol{k}_3|) \\
&\quad \int \frac{dx dx' dy dy' \delta(x + x')}{\left(1 + e^{y}\right)\left(1 + e^{-y-x}\right)\left(1 + e^{y'}\right)\left(1 + e^{-x'-y'}\right)} \\
&= \frac{2\pi^3 G^2 T^2}{12(2\pi)^8 e^2 v_F^4} \int d\theta_1 d\theta_2 d\theta_3 d\theta_4 \delta\left(\boldsymbol{k}_1 + \boldsymbol{k}_2 - \boldsymbol{k}_3 - \boldsymbol{k}_4 - \boldsymbol{G}\right) V^2(|\boldsymbol{k}_1 - \boldsymbol{k}_3|) \\
&= \frac{8\pi^5 G^2 T^2 \eta^2}{12(2\pi)^8 e^2 v_F^2 k_F^4} \int d\theta_1 d\theta_2 d\theta_3 d\theta_4 \\
&\quad \frac{\delta\left(\sin\theta_+ \sin\theta_- + \sin\varphi_+ \sin\varphi_- - G/2k_F\right) \delta\left(\cos\theta_+ \sin\theta_- + \cos\varphi_+ \sin\varphi_-\right)}{\left(|\sin\theta_-| + \eta\right)^2} \\
&\approx \frac{8\pi^5 G^2 T^2 \eta^2}{12(2\pi)^8 e^2 v_F^2 k_F^4} \frac{2\pi^4}{\eta(\eta + \pi/2)}
\end{aligned} \tag{B.25}$$

where $\eta \equiv q_{TF}/2k_F$. Thus the resistivity is given by

$$\rho_{2D} \approx \frac{\pi}{4 \times 192e^2} \frac{G^2}{k_F^2} \left(\frac{T}{\epsilon_F}\right)^2 \frac{\eta^2}{\eta(\eta + \pi/2)} \tag{B.26}$$

Thus we conclude that there is no special enhancement of the e-e resistivity in 2D.

Appendix C

2D Materials Deep Learning Supplementary Information

Here we present supplementary information for Chapter 5.

C.1 Data preprocessing with unsupervised learning

In order to facilitate the pixel-by-pixel labeling of the microscopic images, we need to develop an unsupervised learning algorithm to segment each image into several regions according to the similarities of the distributions of the pixels in each region in the color and/or real spaces. To achieve this goal, several image segmentation methods were tried, including L*a*b space K-means clustering, edge detection based segmentation, and superpixel based segmentation. As all three methods rely heavily on the optical contrast of different regions in the images, we need to firstly find a way to normalize the images in the color space to minimize the variations of the images taken under different conditions. Another challenge is that the optical contrast between different classes could be extremely subtle. This makes any optical contrast based method highly sensitive to the tuning of the hyperparameters. In the following, the normalization and image segmentation methods will be discussed in more details, and according to our analysis, we found that the superpixel based method outperformed the other two methods.

C.1.1 Normalization and L*a*b color space

It is found that the variances of brightness, contrast, white balance, etc. of different images are very large, because the data was collected through a long period of time, with different microscopes, under different tool conditions and by different users with different preferences. Fig. 5-2, the first row shows the different hues and brightnesses of some of the images. Intuitively, we need to normalize the color according to a "reference" color point. The "reference" color point should exist in every single image, and represent the same optical response in the real world. As we used 300 nm SiO_2/Si wafers as the substrates for all the images, it is then possible to use the pixels in the "background" regions as the reference color. Considering that the "background" region takes $60 - 70\%$ of the area in each image, we used the median pixel color to approximate the background color. The images were firstly projected from the RGB color space to the L*a*b color space [1], in which L, a and b indicate respectively the lightness and the components of green-red and blue-yellow. The normalization transformation can be expressed as $L \leftarrow 50L/L_{ref}$, $a \leftarrow a - a_{ref}$, and $b \leftarrow b - b_{ref}$, and the resulting images are shown in the second row of Fig. 5-2. It is clearly seen that the color distributions of each classes become very similar after normalization.

C.1.2 K-Means clustering and edge detection

One way to imlement the unsupervised segmentation is to use the K-means clustering algorithm with the Euclidean distances of the pixels in the L*a*b color space. The top right panel of Fig. C-1 shows the K-means clustering segmentation results with 10 clusters. The profiles of the flakes can be clearly seen and flakes with different thicknesses can be successfully classified into different clusters. However, because such an algorithm only takes the color space distances into consideration, the resulting clusters often include many disconncted regions. To make it worse, some of the thin flakes are classified in the same cluster as certain parts of the non-uniform background because they look similar in color, which is highly undeired. Furthermore, the best

[1] Wikipedia: Lab color space. https://en.wikipedia.org/wiki/Lab_color_space.

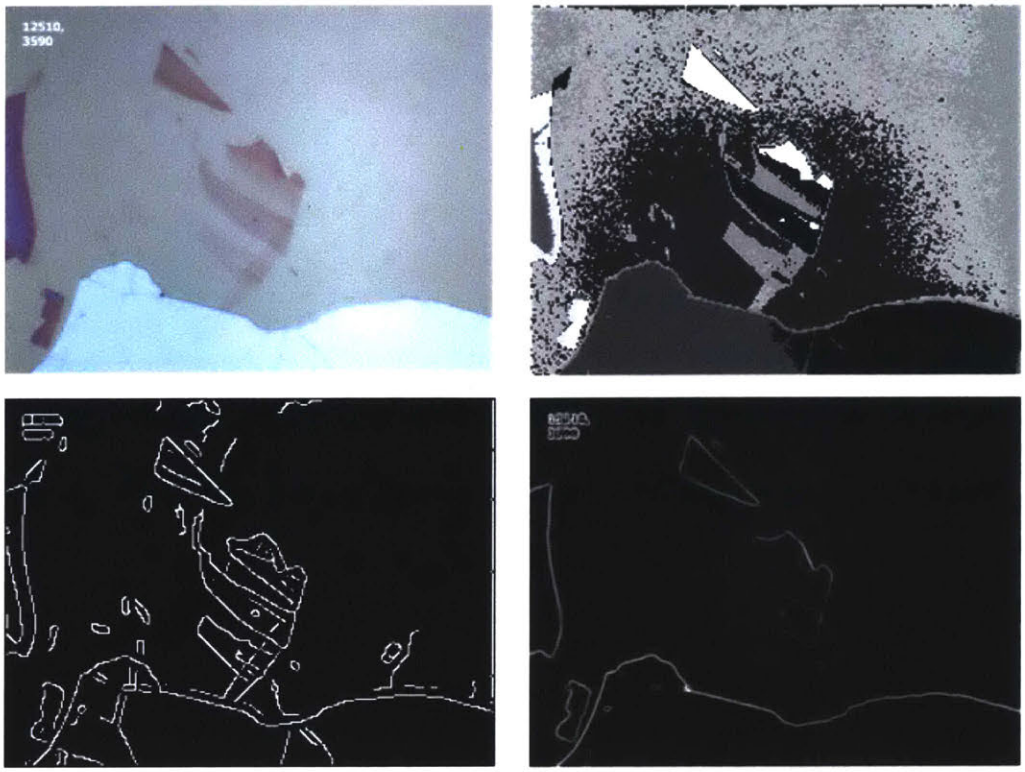

Figure C-1: Image segmentations with K-means clustering and edge detection. (top left) original; (top right) K-means clustering in L*a*b color space, with 10 clusters; (bottom left) edge detection with Canny method; (bottom right) magnitude of gradient of the image.

choice of the number of clusters may vary a lot, as the complexity of the images may be quite different.

Given that the flakes are usually homogeneous in color and have certain level of contrasts with respect to adjacent regions, we also considered several edge detection algorithm and attempted to implement the segmentation based on the detected edges. There exists several edge detection algorithms, and the bottom row of Fig. C-1 shows two of the algorithms, that is, Canny method [2] and magnitude of gradient. However, the edge detection based methods also suffer from several probelms: (1) the threshold of the edge intensity needs to be carefully tuned to balance its ability to detect the very weak edges (usually the edges between the monolayer regions and the background, which is very critical), and its immunity to noises; and (2) many of the detected edges

[2]Wikipedia: Canny edge detector. https://en.wikipedia.org/wiki/Canny_edge_detector.

do not form a closed form, and the therefore the segmentation fails.

C.1.3 Superpixelization and DBSCAN clustering

The third method we have tried is a superpixelization based clustering algorithm. In this algorithm, we firstly over-segment the input images into superpixels with the simple linear iterative clustering (SLIC) method [2]. Superpixel is a clustering of neighboring pixels with perceptually meaningful similarities. The SLIC method adapts the K-means clustering algorithm into the superpixelization problems. The distance used in the K-means clustering algorithm is the distance in the combinational pixel position space $[x, y]^T$ and the L*a*b color space $[l, a, b]^T$ with a specified scaling factor. To eliminate the searching effort, the algorithm also confined the regions of k-means searching to a limited range instead of the entire image as in the standard K-means clustering algorithm. In order to make sure the superpixelization is able to capture finest features of the images, we increased the total number of superpixels and decreased the minimum superpixel diameters. The first and second rows of Fig. C-2 show respectively some typical normalized images and the corresponding superpixel segmentations after the SLIC algorithm.

The second step is to further combine the superpixels according to similarities and achieve the desired level of segmentations of the images. Although the color distributions of each desired cluster may be tight and regular, the spans in the pixel space of the desired clusters may be in very ireggular shape, and thus could not be determined by simply thresholding a distance function. This is when the spectral clustering comes into place. Here we adapted the density based spatial clustering of applications with noise (DBSCAN) method [40] and used the medians of the scaled combination of the L*a*b color space and the pixel space distances as the measure of weigths of the edges between two superpixel vertices. One hyperparameter that is very critical in this algorithm is the threshold value that indicates the maximum distances of two superpixels that can be combined into a single cluster. Because the color-pixel distance between the background and the monolayer regions are usually substantially smaller than the variations within the background and/or the multilayer regions, a

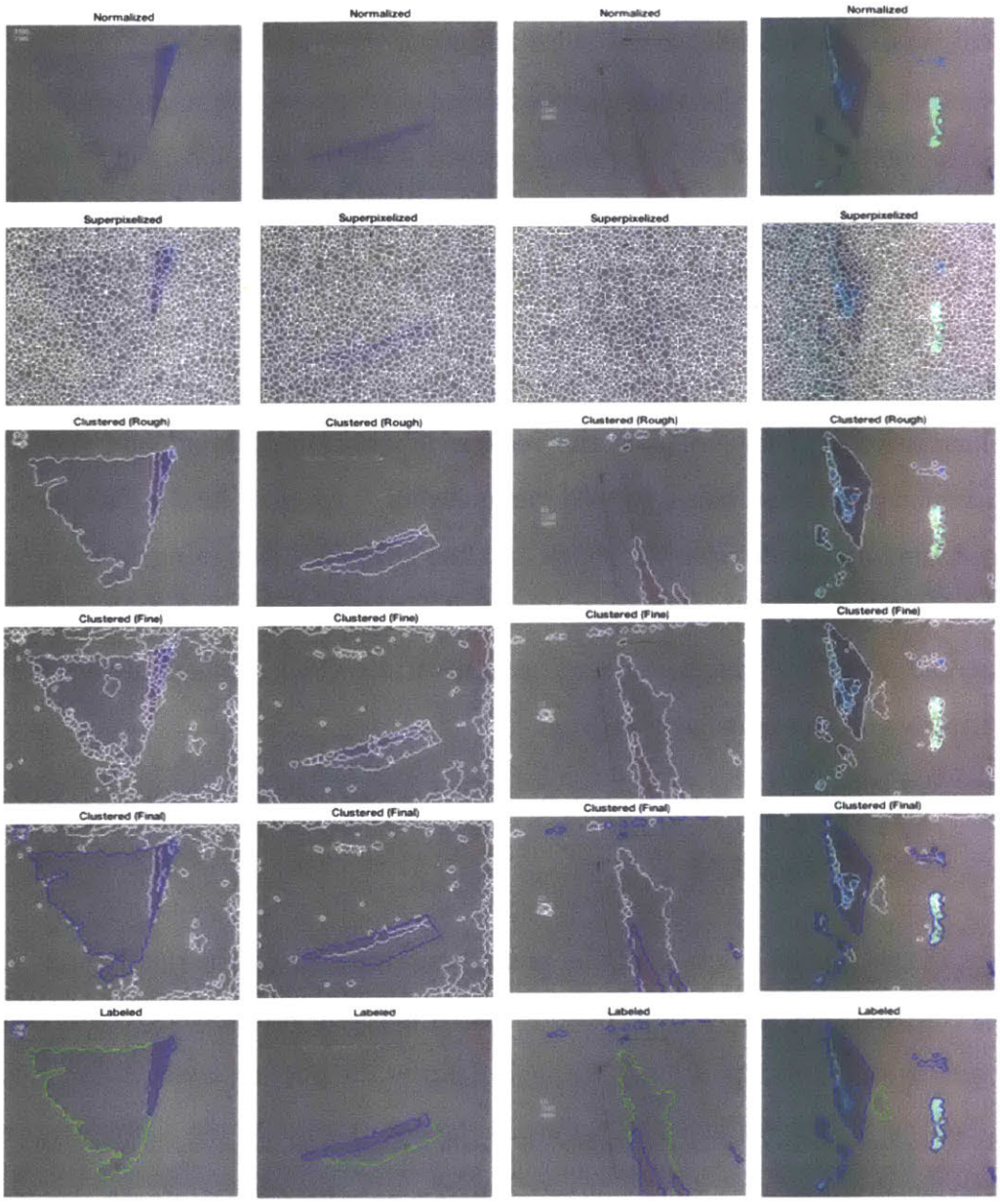

Figure C-2: Image segmentations with superpixelization and DBSCAN clustering.first row: normalized images; second row: superpixelized; third row: after rough DBSCAN clustering; fourth row: after fine DBSCAN clustering; fifth row: combination of two clusterings; sixth row: manually corrected final labels.

single threshold value would either incorrectly combined the monolayer regions into the background regions, or segment the background and the multilayer regions into too many clusters.This aspect is clearly shown as the threshold is set to be relatively large and small, respectively, in the third and fourth row of Fig. C-2.

Nevertheless, among the three methods discussed above, we found that the superpixelization and DBSCAN clustering method does the best job in clustering our data. Therefore we finally used this method to do the unsupervised clustering.

Fig. C-2 shows four examples of the labeling procedure, with each row indicating the normalized images, superpixelations, rough DBSCAN clusterings, fine DBSCAN clusterings, proposed labeling, and manually corrected labeling results, respectively. The blue-circled regions indicates the regions labeled "multilayer" and the green-circled regions indicates those labeled "monolayers". As seen in the fifth row, the proposed labeling results from the rough and fine DBSCAN clusterings could identify the background and multilayer regions very well, but the supposely monolayer regions were merged into either regions underdeterministically. This is when human power is needed to correct the monolayer regions.

C.2 Architecture

In Fig. C-3, we plot the details of the architecture of SegNet. In this figure, "conv" denotes convolutional layers, "bn" denotes batch normalization layers, "relu" denotes ReLU activation layers, "pool" and "unpool" denotes the pooling layers and unpooling layers, "softmax" denotes Softmax activation layers. Arrows in the figure denote the connectivity and information flow in the SegNet.

C.3 Training and testing

The training and testing of the SegNet were implemented in MATLAB R2018b with the help of the Deep Learning Toolbox, the Parallel Computing Toolbox, the Computer Vision Toolbox and the Image Processing Toolbox. The training and testing

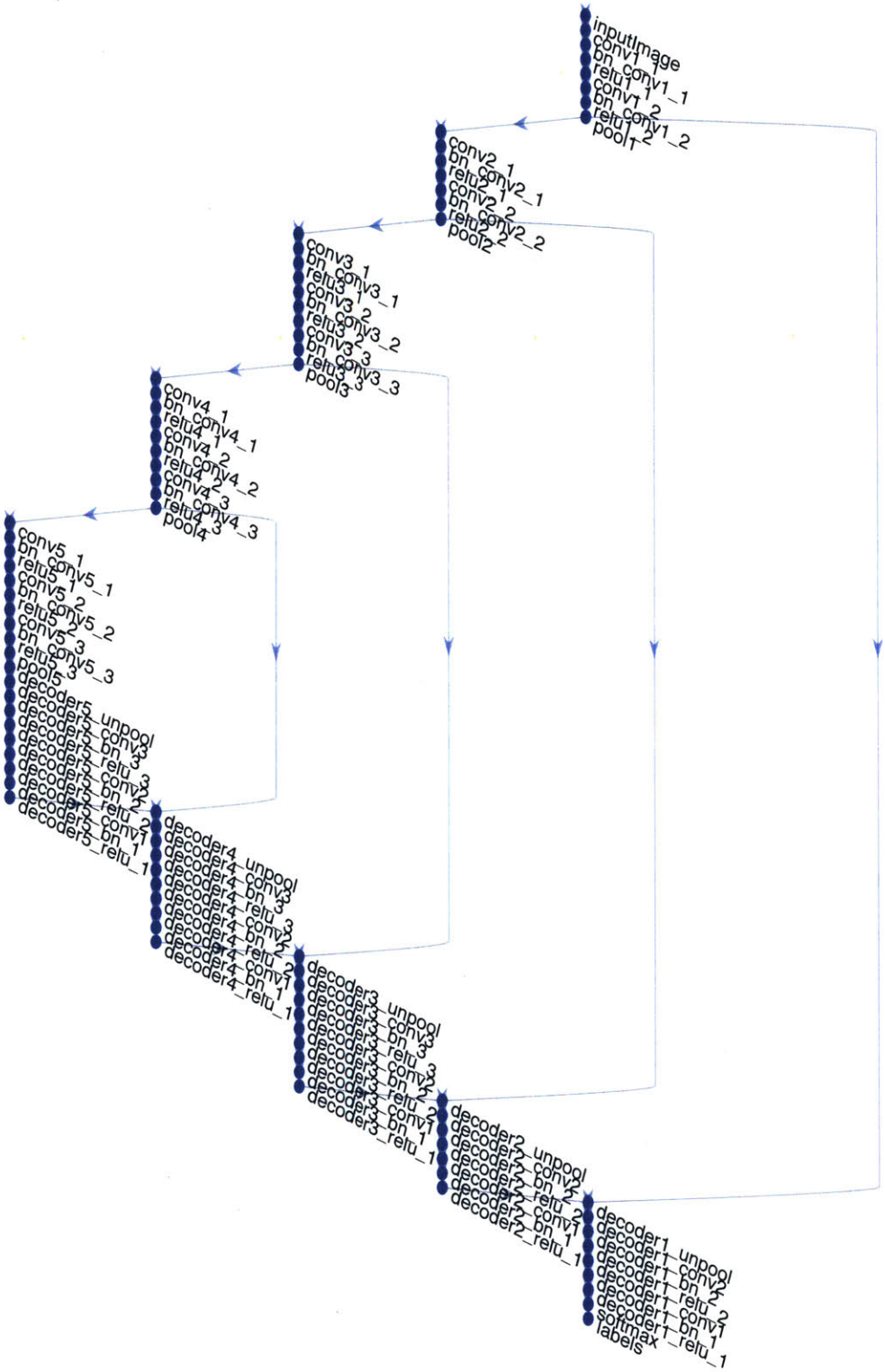

Figure C-3: Architecture of the SegNet used in our study.

were performed using a desktop computer equipped with a CPU (Intel(R) Core (TM) i7-8700K @ 3.70GHz, 32.0GB RAM) and a GPU (NVIDIA GeForce GTX 1080 Ti, 11 GB GDDR5X). The stochastic gradient descent with momentum (SGDM) method was used to find the weights in the convolutional filters of the SegNet during the training process. To compensate for the imbalanced numbers of pixels for different classes (for example, the "background" labels take more than 85% of areas in most images), class weightings based on inverse frequencies were used in the soft-max classifier.

C.4 Resources

1. Matlab's Image Processing Package and Deep Learning Package.
2. Peter Koveski's Image Segmentation Package. Methods: slic(), dbscan(), etc. (link: http://www.peterkovesi.com/projects/segmentation/)
3. Courtesy of the Data Source: Pablo Jarillo-Hererro's group @ MIT Physics.
4. Thanks to Yuxuan (Cosmi) Lin from Tomás Palacios's group, Bingnan Han and Nannan Mao from Jing Kong's group @ MIT.
5. Part of the code is posted on GitHub: `https://github.com/yafangy/Nanomaterial_DeepLearning`

Bibliography

[1] M. Abdel-Hafiez, X.-M. Zhao, A. Kordyuk, Y.-W. Fang, B. Pan, Z. He, C.-G. Duan, J. Zhao, and X.-J. Chen. Enhancement of superconductivity under pressure and the magnetic phase diagram of tantalum disulfide single crystals. *Sci. Rep.*, 6, 2016.

[2] R. Achanta, A. Shaji, K. Smith, A. Lucchi, P. Fua, S. Süsstrunk, et al. Slic superpixels compared to state-of-the-art superpixel methods. *IEEE Trans. Pattern Anal. Mach. Intell.*, 34(11):2274–2282, 2012.

[3] O. R. Albertini, A. Y. Liu, and M. Calandra. Effect of electron doping on lattice instabilities in single-layer 1H-TaS_2. *Phys. Rev. B*, 95(23):235121, 2017.

[4] E. M. Alexeev, D. A. Ruiz-Tijerina, M. Danovich, M. J. Hamer, D. J. Terry, P. K. Nayak, S. Ahn, S. Pak, J. Lee, J. I. Sohn, et al. Resonantly hybridized excitons in moiré superlattices in van der Waals heterostructures. *Nature*, 567(7746):81, 2019.

[5] V. Ambegaokar and A. Baratoff. Tunneling between superconductors. *Phys. Rev. Lett.*, 10(11):486, 1963.

[6] L. Aslamasov and A. Larkin. The influence of fluctuation pairing of electrons on the conductivity of normal metal. *Phys. Lett. A*, 26(6):238–239, 1968.

[7] A. Ayari, E. Cobas, O. Ogundadegbe, and M. S. Fuhrer. Realization and electrical characterization of ultrathin crystals of layered transition-metal dichalcogenides. *J. Appl. Phys.*, 101(1):014507, 2007.

[8] V. Badrinarayanan, A. Kendall, and R. C. SegNet. A deep convolutional encoder-decoder architecture for image segmentation. *arXiv preprint arXiv:1511.00561.*

[9] J. Bardeen. Critical fields and currents in superconductors. *Rev. Mod. Phys.*, 34(4):667, 1962.

[10] J. Bardeen, L. N. Cooper, and J. R. Schrieffer. Microscopic theory of superconductivity. *Phys. Rev.*, 106(1):162, 1957.

[11] J. Bardeen, L. N. Cooper, and J. R. Schrieffer. Theory of superconductivity. *Phys. Rev.*, 108(5):1175, 1957.

[12] S. C. Barrera, M. R. Sinko, D. P. Gopalan, N. Sivadas, K. L. Seyler, K. Watanabe, T. Taniguchi, A. W. Tsen, X. Xu, D. Xiao, et al. Tuning ising superconductivity with layer and spin–orbit coupling in two-dimensional transition-metal dichalcogenides. *Nat. Commun.*, 9(1):1427, 2018.

[13] B. W. Baugher, H. O. Churchill, Y. Yang, and P. Jarillo-Herrero. Intrinsic electronic transport properties of high-quality monolayer and bilayer MoS_2. *Nano Lett.*, 13(9):4212–4216, 2013.

[14] B. W. Baugher, H. O. Churchill, Y. Yang, and P. Jarillo-Herrero. Optoelectronic devices based on electrically tunable p-n diodes in a monolayer dichalcogenide. *Nat. Nano.*, 9(4):262, 2014.

[15] A. Beal, H. Hughes, and W. Liang. The reflectivity spectra of some group VA transition metal dichalcogenides. *J. Phys. C: Solid State Phys.*, 8(24):4236, 1975.

[16] L. Benfatto, A. Toschi, S. Caprara, and C. Castellani. Coherence length in superconductors from weak to strong coupling. *Phys. Rev. B*, 66(5):054515, 2002.

[17] R. Bistritzer and A. H. MacDonald. Moiré bands in twisted double-layer graphene. *Proc. Natl. Acad. Sci. U.S.A.*, 108(30):12233–12237, 2011.

[18] P. Blake, E. Hill, A. Castro Neto, K. Novoselov, D. Jiang, R. Yang, T. Booth, and A. Geim. Making graphene visible. *Appl. Phys. Lett.*, 91(6):063124, 2007.

[19] T. Cai, S. A. Yang, X. Li, F. Zhang, J. Shi, W. Yao, and Q. Niu. Magnetic control of the valley degree of freedom of massive dirac fermions with application to transition metal dichalcogenides. *Phys. Rev. B*, 88(11):115140, 2013.

[20] M. Calandra, I. Mazin, and F. Mauri. Effect of dimensionality on the charge-density wave in few-layer 2H-$NbSe_2$. *Phys. Rev. B*, 80(24):241108, 2009.

[21] T. Cao, G. Wang, W. Han, H. Ye, C. Zhu, J. Shi, Q. Niu, P. Tan, E. Wang, B. Liu, et al. Valley-selective circular dichroism of monolayer molybdenum disulphide. *Nat. Commun.*, 3:887, 2012.

[22] Y. Cao, V. Fatemi, A. Demir, S. Fang, S. L. Tomarken, J. Y. Luo, J. D. Sanchez-Yamagishi, K. Watanabe, T. Taniguchi, E. Kaxiras, et al. Correlated insulator behaviour at half-filling in magic-angle graphene superlattices. *Nature*, 556(7699):80, 2018.

[23] Y. Cao, V. Fatemi, S. Fang, K. Watanabe, T. Taniguchi, E. Kaxiras, and P. Jarillo-Herrero. Unconventional superconductivity in magic-angle graphene superlattices. *Nature*, 556(7699):43, 2018.

[24] Y. Cao, J. Luo, V. Fatemi, S. Fang, J. Sanchez-Yamagishi, K. Watanabe, T. Taniguchi, E. Kaxiras, and P. Jarillo-Herrero. Superlattice-induced insulating states and valley-protected orbits in twisted bilayer graphene. *Phys. Rev. Lett.*, 117(11):116804, 2016.

[25] Y. Cao, A. Mishchenko, G. Yu, E. Khestanova, A. Rooney, E. Prestat, A. Kretinin, P. Blake, M. Shalom, C. Woods, et al. Quality heterostructures from two-dimensional crystals unstable in air by their assembly in inert atmosphere. *Nano Lett.*, 15(8):4914–4921, 2015.

[26] A. Castellanos-Gomez, N. Agraït, and G. Rubio-Bollinger. Optical identification of atomically thin dichalcogenide crystals. *Appl. Phys. Lett.*, 96(21):213116, 2010.

[27] L.-C. Chen, G. Papandreou, I. Kokkinos, K. Murphy, and A. L. Yuille. Deeplab: Semantic image segmentation with deep convolutional nets, atrous convolution, and fully connected crfs. *IEEE Trans. Pattern Anal. Mach. Intell.*, 40(4):834–848, 2018.

[28] K. Choudhary, G. Cheon, E. Reed, and F. Tavazza. Elastic properties of bulk and low-dimensional materials using van der Waals density functional. *Phys. Rev. B*, 98(1):014107, 2018.

[29] C. Chu, V. Diatschenko, C. Huang, and F. DiSalvo. Pressure effect on the charge-density-wave formation in 2H-$NbSe_2$ and correlation between structural instabilities and superconductivity in unstable solids. *Phys. Rev. B*, 15(3):1340, 1977.

[30] H.-J. Chuang, X. Tan, N. J. Ghimire, M. M. Perera, B. Chamlagain, M. M.-C. Cheng, J. Yan, D. Mandrus, D. Tománek, and Z. Zhou. High mobility WSe_2 p- and n-type field-effect transistors contacted by highly doped graphene for low-resistance contacts. *Nano Lett.*, 14(6):3594–3601, 2014.

[31] S. Chuang, C. Battaglia, A. Azcatl, S. McDonnell, J. S. Kang, X. Yin, M. Tosun, R. Kapadia, H. Fang, R. M. Wallace, and A. Javey. MoS_2 p-type Transistors and Diodes Enabled by High Work Function MoO_x Contacts. *Nano Lett.*, 14(3):1337–1342, Mar. 2014.

[32] X. Cui, G.-H. Lee, Y. D. Kim, G. Arefe, P. Y. Huang, C.-H. Lee, D. A. Chenet, X. Zhang, L. Wang, F. Ye, et al. Multi-terminal transport measurements of MoS_2 using a van der Waals heterostructure device platform. *Nat. Nano.*, 10(6):534, 2015.

[33] S. Das, H.-Y. Chen, A. V. Penumatcha, and J. Appenzeller. High performance multilayer MoS_2 transistors with scandium contacts. *Nano Lett.*, 13(1):100–105, 2012.

[34] S. Datta. *Quantum Hall effect*, page 175–195. Cambridge Studies in Semiconductor Physics and Microelectronic Engineering. Cambridge University Press, 1995.

[35] C. R. Dean, L. Wang, P. Maher, C. Forsythe, F. Ghahari, Y. Gao, J. Katoch, M. Ishigami, P. Moon, M. Koshino, et al. Hofstadter's butterfly and the fractal quantum hall effect in moiré superlattices. *Nature*, 497(7451):598, 2013.

[36] C. R. Dean, A. F. Young, I. Meric, C. Lee, L. Wang, S. Sorgenfrei, K. Watanabe, T. Taniguchi, P. Kim, K. L. Shepard, and J. Hone. Boron nitride substrates for high-quality graphene electronics. *Nat. Nano.*, 5(10):722–726, 2010.

[37] F. Di Salvo, R. Schwall, T. Geballe, F. Gamble, and J. Osiecki. Superconductivity in layered compounds with variable interlayer spacings. *Phys. Rev. Lett.*, 27(6):310, 1971.

[38] D. Efetov, L. Wang, C. Handschin, K. Efetov, J. Shuang, R. Cava, T. Taniguchi, K. Watanabe, J. Hone, C. Dean, et al. Specular interband Andreev reflections at van der Waals interfaces between graphene and $Nbse_2$. *Nat. Phys.*, 12(4):328, 2016.

[39] M. S. El-Bana, D. Wolverson, S. Russo, G. Balakrishnan, D. M. Paul, and S. J. Bending. Superconductivity in two-dimensional $NbSe_2$ field effect transistors. *Supercond. Sci. Technol.*, 26(12):125020, 2013.

[40] M. Ester, H.-P. Kriegel, J. Sander, X. Xu, et al. A density-based algorithm for discovering clusters in large spatial databases with noise. In *Kdd*, volume 96, pages 226–231, 1996.

[41] B. L. Evans and P. A. Young. Optical Absorption and Dispersion in Molybdenum Disulphide. *Proc. Royal Soc. Lond A*, 284:402, 1965.

[42] B. Fallahazad, H. C. Movva, K. Kim, S. Larentis, T. Taniguchi, K. Watanabe, S. K. Banerjee, and E. Tutuc. Shubnikov-de haas oscillations of high-mobility holes in monolayer and bilayer WSe_2: Landau level degeneracy, effective mass, and negative compressibility. *Phys. Rev. Lett.*, 116(8):086601, 2016.

[43] H. Fang, S. Chuang, T. C. Chang, K. Takei, T. Takahashi, and A. Javey. High-performance single layered WSe_2 p-FETs with chemically doped contacts. *Nano Lett.*, 12(7):3788–3792, 2012.

[44] L. Fang, P. Y. Zou, Y. Wang, L. Tang, Z. Xu, H. Chen, C. Dong, L. Shan, and H. H. Wen. Competition of superconductivity and charge density wave order in Na_xTaS_2 single crystals. *Sci. Technol. Adv. Mater.*, 6(7):736–739, Jan. 2005.

[45] M. Farjam. Projection operator approach to unfolding supercell band structures. *arXiv:1504.04937*, 2015.

[46] R. Fivaz and E. Mooser. Mobility of charge carriers in semiconducting layer structures. *Phys. Rev.*, 163(3):743, 1967.

[47] F. Flicker and J. van Wezel. Charge order in $NbSe_2$. *Phys. Rev. B*, 94(23):235135, 2016.

[48] D. Freitas, P. Rodiere, M. Osorio, E. Navarro-Moratalla, N. Nemes, V. Tissen, L. Cario, E. Coronado, M. García-Hernández, S. Vieira, et al. Strong enhancement of superconductivity at high pressures within the charge-density-wave states of 2H-TaS_2 and 2H-$TaSe_2$. *Phys. Rev. B*, 93(18):184512, 2016.

[49] P. Gallagher, M. Lee, T. A. Petach, S. W. Stanwyck, J. R. Williams, K. Watanabe, T. Taniguchi, and D. Goldhaber-Gordon. A high-mobility electronic system at an electrolyte-gated oxide surface. *Nat. Commun.*, 6:6437, 2015.

[50] Y. Ge and A. Y. Liu. Effect of dimensionality and spin-orbit coupling on charge-density-wave transition in 2H-$TaSe_2$. *Phys. Rev. B*, 86(10):104101, 2012.

[51] A. K. Geim and I. V. Grigorieva. Van der Waals heterostructures. *Nature*, 499:419, 2013.

[52] A. K. Geim and K. S. Novoselov. The rise of graphene. *Nat. Mater.*, 6(3):183–191, 2007.

[53] A. A. Golubov and A. Koshelev. Upper critical field in dirty two-band superconductors: Breakdown of the anisotropic ginzburg-landau theory. *Phys. Rev. B*, 68(10):104503, 2003.

[54] R. Gorbachev, A. Geim, M. Katsnelson, K. Novoselov, T. Tudorovskiy, I. Grigorieva, A. MacDonald, S. Morozov, K. Watanabe, T. Taniguchi, et al. Strong coulomb drag and broken symmetry in double-layer graphene. *Nat. Phys.*, 8(12):896, 2012.

[55] R. V. Gorbachev, I. Riaz, R. R. Nair, R. Jalil, L. Britnell, B. D. Belle, E. W. Hill, K. S. Novoselov, K. Watanabe, T. Taniguchi, et al. Hunting for monolayer boron nitride: optical and Raman signatures. *Small*, 7(4):465–468, 2011.

[56] I. Guillamón, H. Suderow, J. G. Rodrigo, S. Vieira, P. Rodière, L. Cario, E. Navarro-Moratalla, C. Martí-Gastaldo, and E. Coronado. Chiral charge order in the superconductor 2H-TaS_2. *New J. Phys.*, 13(10):103020, Oct. 2011.

[57] G. Guizzetti, L. Nosenzo, I. Pollini, E. Reguzzoni, G. Samoggia, and G. Spinolo. Reflectance and thermoreflectance studies of crcl 3, crbr 3, nicl 2, and nibr 2 crystals. *Physical Review B*, 14(10):4622, 1976.

[58] O. Gunawan, Y. Shkolnikov, K. Vakili, T. Gokmen, E. De Poortere, and M. Shayegan. Valley susceptibility of an interacting two-dimensional electron system. *Phys. Rev. Lett.*, 97(18):186404, 2006.

[59] M. V. Gustafsson, M. Yankowitz, C. Forsythe, D. Rhodes, K. Watanabe, T. Taniguchi, J. Hone, X. Zhu, and C. R. Dean. Ambipolar Landau levels and strong band-selective carrier interactions in monolayer WSe_2. *Nat. Mater.*, 17(5):411, 2018.

[60] D. Haviland, Y. Liu, and A. Goldman. Onset of superconductivity in the two-dimensional limit. *Phys. Rev. Lett.*, 62(18):2180, 1989.

[61] R. Hlubina and T. Rice. Resistivity as a function of temperature for models with hot spots on the fermi surface. *Phys. Rev. B*, 51(14):9253, 1995.

[62] B. Hunt, J. Sanchez-Yamagishi, A. Young, M. Yankowitz, B. J. LeRoy, K. Watanabe, T. Taniguchi, P. Moon, M. Koshino, P. Jarillo-Herrero, et al. Massive dirac fermions and Hofstadter butterfly in a van der Waals heterostructure. *Science*, page 1237240, 2013.

[63] A. Jacko, J. Fjærestad, and B. Powell. A unified explanation of the kadowaki–woods ratio in strongly correlated metals. *Nat. Phys.*, 5(6):422–425, 2009.

[64] C. Jin, E. C. Regan, A. Yan, M. I. B. Utama, D. Wang, S. Zhao, Y. Qin, S. Yang, Z. Zheng, S. Shi, et al. Observation of moiré excitons in WSe_2/WS_2 heterostructure superlattices. *Nature*, page 1, 2019.

[65] A. M. Jones, H. Yu, N. Ghimire, S. Wu, G. Aivazian, J. S. Ross, B. Zhao, J. Yan, D. Mandrus, and D. Xiao. Optical Generation of Excitonic Valley Coherence in Monolayer WSe_2. *Nat. Nano.*, 8:634, 2013.

[66] K. Kaasbjerg, K. S. Thygesen, and K. W. Jacobsen. Phonon-limited mobility in n-type single-layer MoS_2 from first principles. *Phys. Rev. B*, 85(11):115317, 2012.

[67] M. KaiáLee et al. Large-area few-layered graphene film determination by multispectral imaging microscopy. *Nanoscale*, 7(19):9033–9039, 2015.

[68] Y. Kashihara, A. Nishida, and H. Yoshioka. Upper and lower critical fields of $TaS_2(\text{Pyridine})_{1/2}$. *J. Phys. Soc. Jpn.*, 46(4):1112–1118, 1979.

[69] M. I. Katsnelson, K. S. Novoselov, and A. K. Geim. Chiral tunnelling and the Klein paradox in graphene. *Nat. Phys.*, 2(9):620–625, 2006.

[70] E. Khestanova, J. Birkbeck, M. Zhu, Y. Cao, G. Yu, D. Ghazaryan, J. Yin, H. Berger, L. Forró, T. Taniguchi, et al. Unusual suppression of the superconducting energy gap and critical temperature in atomically thin $NbSe_2$. *Nano Lett.*, 2018.

[71] T. Kiss, T. Yokoya, A. Chainani, S. Shin, T. Hanaguri, M. Nohara, and H. Takagi. Charge-order-maximized momentum-dependent superconductivity. *Nat. Phys.*, 3(10):720–725, 2007.

[72] D. R. Klein, D. MacNeill, J. L. Lado, D. Soriano, E. Navarro-Moratalla, K. Watanabe, T. Taniguchi, S. Manni, P. Canfield, J. Fernández-Rossier, et al. Probing magnetism in 2D van der Waals crystalline insulators via electron tunneling. *Science*, 360(6394):1218–1222, 2018.

[73] K. v. Klitzing, G. Dorda, and M. Pepper. New method for high-accuracy determination of the fine-structure constant based on quantized Hall resistance. *Phys. Rev. Lett.*, 45(6):494, 1980.

[74] J. M. Kosterlitz and D. J. Thouless. Ordering, metastability and phase transitions in two-dimensional systems. *J. Phys. C: Solid State Phys.*, 6(7):1181, 1973.

[75] G. Kresse and J. Furthmüller. Efficiency of ab-initio total energy calculations for metals and semiconductors using a plane-wave basis set. *Comput. Mater. Sci.*, 6(1):15–50, 1996.

[76] G. Kresse and J. Furthmüller. Efficient iterative schemes for ab initio total-energy calculations using a plane-wave basis set. *Phys. Rev. B*, 54(16):11169, 1996.

[77] W. Ku, T. Berlijn, and C.-C. Lee. Unfolding first-principles band structures. *Phys. Rev. Lett.*, 104:216401, May 2010.

[78] J. L. Lado and J. Fernández-Rossier. On the origin of magnetic anisotropy in two dimensional CrI_3. *2D Mater.*, 4(3):035002, 2017.

[79] C.-H. Lee, G.-H. Lee, A. M. Van Der Zande, W. Chen, Y. Li, M. Han, X. Cui, G. Arefe, C. Nuckolls, T. F. Heinz, et al. Atomically thin p-n junctions with van der Waals heterointerfaces. *Nat. Nano.*, 9(9):676, 2014.

[80] G.-H. Lee, Y.-J. Yu, C. Lee, C. Dean, K. L. Shepard, P. Kim, and J. Hone. Electron tunneling through atomically flat and ultrathin hexagonal boron nitride. *Appl. Phys. Lett.*, 99(24):243114, 2011.

[81] J. U. Lee, P. Gipp, and C. Heller. Carbon nanotube p-n junction diodes. *Appl. Phys. Lett.*, 85(1):145–147, 2004.

[82] H. Li, J. Wu, X. Huang, G. Lu, J. Yang, X. Lu, Q. Xiong, and H. Zhang. Rapid and reliable thickness identification of two-dimensional nanosheets using optical microscopy. *ACS Nano*, 7(11):10344–10353, 2013.

[83] L. Li, X. Deng, Z. Wang, Y. Liu, and M. Abeykoon. Superconducting order from disorder in 2H-$TaSe_{2-x}S_x$. *npj Quant. Mater.*, 2(1):11, 2017.

[84] W. Li, S. Moon, M. Wojcik, and K. Xu. Direct optical visualization of graphene and its nanoscale defects on transparent substrates. *Nano Lett.*, 16(8):5027–5031, 2016.

[85] X. Li, F. Zhang, and Q. Niu. Unconventional quantum hall effect and tunable spin hall effect in Dirac materials: application to an isolated MoS_2 trilayer. *Phys. Rev. Lett.*, 110(6):066803, 2013.

[86] Y. Li, J. Jiang, H. Yang, D. Prabhakaran, Z. Liu, L. Yang, and Y. Chen. Folded superstructure and degeneracy-enhanced band gap in the weak-coupling charge density wave system 2H-$TaSe_2$. *Phys. Rev. B*, 97(11):115118, 2018.

[87] C.-H. Lin, T. Berlijn, L. Wang, C.-C. Lee, W.-G. Yin, and W. Ku. One-fe versus two-fe brillouin zone of fe-based superconductors: Creation of the electron pockets by translational symmetry breaking. *Phys. Rev. Lett.*, 107:257001, Dec 2011.

[88] X. Lin, Z. Si, W. Fu, J. Yang, S. Guo, Y. Cao, J. Zhang, X. Wang, P. Liu, K. Jiang, et al. Intelligent identification of two-dimensional nanostructures by machine-learning optical microscopy. *Nano Research*, 11(12):6316–6324, 2018.

[89] W. Liu, J. Kang, D. Sarkar, Y. Khatami, D. Jena, and K. Banerjee. Role of Metal Contacts in Designing High-Performance Monolayer n-Type WSe_2 Field Effect Transistors. *Nano Lett.*, 13(5):1983–1990, May 2013.

[90] J. Long, E. Shelhamer, and T. Darrell. Fully convolutional networks for semantic segmentation. In *Proc. IEEE Comput. Soc. Conf. Comput. Vis. Pattern Recognit.*, pages 3431–3440, 2015.

[91] J. Lu, O. Zheliuk, I. Leermakers, N. F. Yuan, U. Zeitler, K. T. Law, and J. Ye. Evidence for two-dimensional ising superconductivity in gated MoS_2. *Science*, 350(6266):1353–1357, 2015.

[92] K. F. Mak, K. He, J. Shan, and T. F. Heinz. Control of valley polarization in monolayer MoS_2 by optical helicity. *Nat. Nano.*, 7(8):494–498, 2012.

[93] K. F. Mak, C. Lee, J. Hone, J. Shan, and T. F. Heinz. Atomically Thin MoS_2: A New Direct-Gap Semiconductor. *Phys. Rev. Lett.*, 105(13):136805, 2010.

[94] K. F. Mak, K. L. McGill, J. Park, and P. L. McEuen. The valley Hall effect in MoS_2 transistors. *Science*, 344(6191):1489–1492, 2014.

[95] N. Mao, J. Tang, L. Xie, J. Wu, B. Han, J. Lin, S. Deng, W. Ji, H. Xu, K. Liu, et al. Optical anisotropy of black phosphorus in the visible regime. *J. Am. Chem. Soc.*, 138(1):300–305, 2015.

[96] N. Marzari, A. A. Mostofi, J. R. Yates, I. Souza, and D. Vanderbilt. Maximally localized wannier functions: Theory and applications. *Rev. Mod. Phys.*, 84(4):1419, 2012.

[97] L. Mattheiss. Band structures of transition-metal-dichalcogenide layer compounds. *Phys. Rev. B*, 8(8):3719, 1973.

[98] A. S. Mayorov, R. V. Gorbachev, S. V. Morozov, L. Britnell, R. Jalil, L. A. Ponomarenko, P. Blake, K. S. Novoselov, K. Watanabe, and T. Taniguchi. Micrometer-scale ballistic transport in encapsulated graphene at room temperature. *Nano Lett.*, 11(6):2396–2399, 2011.

[99] M. A. McGuire, G. Clark, K. Santosh, W. M. Chance, G. E. Jellison Jr, V. R. Cooper, X. Xu, and B. C. Sales. Magnetic behavior and spin-lattice coupling in cleavable van der Waals layered $CrCl_3$ crystals. *Phys. Rev. Mater.*, 1(1):014001, 2017.

[100] W. McMillan. Transition temperature of strong-coupled superconductors. *Phys. Rev.*, 167(2):331, 1968.

[101] R. Misra, M. McCarthy, and A. F. Hebard. Electric field gating with ionic liquids. *Appl. Phys. Lett.*, 90(5):052905, 2007.

[102] H. C. Movva, B. Fallahazad, K. Kim, S. Larentis, T. Taniguchi, K. Watanabe, S. K. Banerjee, and E. Tutuc. Density-dependent quantum Hall states and Zeeman splitting in monolayer and bilayer WSe_2. *Phys. Rev. Lett.*, 118(24):247701, 2017.

[103] S. Nagata, T. Aochi, T. Abe, S. Ebisu, T. Hagino, Y. Seki, and K. Tsutsumi. Superconductivity in the layered compound 2H-TaS_2. *J. Phys. Chem. Solids*, 53(10):1259–1263, 1992.

[104] M. Naito and S. Tanaka. Electrical transport properties in 2H-NbS_2,-$NbSe_2$,-TaS_2 and-$TaSe_2$. *J. Phys. Soc. Jpn.*, 51(1):219–227, 1982.

[105] E. Navarro-Moratalla, J. O. Island, S. Mañas-Valero, E. Pinilla-Cienfuegos, A. Castellanos-Gomez, J. Quereda, G. Rubio-Bollinger, L. Chirolli, J. A. Silva-Guillén, N. Agraït, G. A. Steele, F. Guinea, H. S. J. van der Zant, and E. Coronado. Enhanced superconductivity in atomically thin TaS_2. *Nat. Commun.*, 7:11043, Mar. 2016.

[106] A. C. Neto. Charge density wave, superconductivity, and anomalous metallic behavior in 2D transition metal dichalcogenides. *Phys. Rev. Lett.*, 86(19):4382, 2001.

[107] A. C. Neto, F. Guinea, N. M. Peres, K. S. Novoselov, and A. K. Geim. The electronic properties of graphene. *Rev. Mod. Phys.*, 81(1):109, 2009.

[108] Z. Ni, H. Wang, J. Kasim, H. Fan, T. Yu, Y. Wu, Y. Feng, and Z. Shen. Graphene thickness determination using reflection and contrast spectroscopy. *Nano Lett.*, 7(9):2758–2763, 2007.

[109] K. Novoselov, A. Mishchenko, A. Carvalho, and A. C. Neto. 2D materials and van der Waals heterostructures. *Science*, 353(6298):aac9439, 2016.

[110] K. S. Novoselov, A. K. Geim, S. Morozov, D. Jiang, M. Katsnelson, I. Grigorieva, S. Dubonos, Firsov, and AA. Two-dimensional gas of massless dirac fermions in graphene. *Nature*, 438(7065):197, 2005.

[111] K. S. Novoselov, A. K. Geim, S. V. Morozov, D. Jiang, Y. Zhang, S. V. I. Dubonos, V. Grigorieva, and A. A. Firsov. Electric field effect in atomically thin carbon films. *Science*, 306(5696):666–669, 2004.

[112] H. Ohno. *Electrochemical Aspects of Ionic Liquids.* John Wiley & Sons, Mar. 2011.

[113] P. Olsson and P. Minnhagen. On the helicity modulus, the critical temperature and monte carlo simulations for the two-dimensional xy-model. *Physica Scripta*, 43(2):203, 1991.

[114] J. Pan, C. Guo, C. Song, X. Lai, H. Li, W. Zhao, H. Zhang, G. Mu, K. Bu, T. Lin, X. Xie, M. Chen, and F. Huang. Enhanced Superconductivity in Restacked TaS_2 Nanosheets. *J. Am. Chem. Soc.*, 139(13):4623–4626, Mar. 2017.

[115] M. J. Panzer, C. R. Newman, and C. D. Frisbie. Low-voltage operation of a pentacene field-effect transistor with a polymer electrolyte gate dielectric. *Appl. Phys. Lett.*, 86(10):103503, 2005.

[116] V. Podzorov, M. E. Gershenson, C. Kloc, R. Zeis, and E. Bucher. High-mobility field-effect transistors based on transition metal dichalcogenides. *Appl. Phys. Lett.*, 84(17):3301, 2004.

[117] L. Ponomarenko, R. Gorbachev, G. Yu, D. Elias, R. Jalil, A. Patel, A. Mishchenko, A. Mayorov, C. Woods, J. Wallbank, et al. Cloning of Dirac fermions in graphene superlattices. *Nature*, 497(7451):594, 2013.

[118] V. Popescu and A. Zunger. Extracting E versus k effective band structure from supercell calculations on alloys and impurities. *Phys. Rev. B*, 85(8):085201, 2012.

[119] B. Radisavljevic, A. Radenovic, J. Brivio, V. Giacometti, and A. Kis. Single-layer MoS_2 transistors. *Nat. Nano.*, 6(3):147–150, 2011.

[120] S. F. A. Rahman, A. M. Hashim, and S. Kasai. Identification of graphene layer numbers from color combination contrast image for wide-area characterization. *Jpn. J. Appl. Phys*, 51(6S):06FD09, 2012.

[121] O. Ronneberger, P. Fischer, and T. Brox. U-net: Convolutional networks for biomedical image segmentation. In *International Conference on Medical image computing and computer-assisted intervention*, pages 234–241. Springer, 2015.

[122] A. Rosch. Interplay of disorder and spin fluctuations in the resistivity near a quantum critical point. *Phys. Rev. Lett.*, 82(21):4280, 1999.

[123] O. Rubel, A. Bokhanchuk, S. J. Ahmed, and E. Assmann. Unfolding the band structure of disordered solids: From bound states to high-mobility kane fermions. *Phys. Rev. B*, 90:115202, Sep 2014.

[124] Y. Saito, Y. Nakamura, M. S. Bahramy, Y. Kohama, J. Ye, Y. Kasahara, Y. Nakagawa, M. Onga, M. Tokunaga, T. Nojima, et al. Superconductivity protected by spin-valley locking in ion-gated MoS_2. *Nat. Phys.*, 12(2):144–149, 2016.

[125] Y. Saito, T. Nojima, and Y. Iwasa. Highly crystalline 2D superconductors. *Nat. Rev. Mater.*, 2(1):16094, Dec. 2016.

[126] C. E. Sanders, M. Dendzik, A. S. Ngankeu, A. Eich, A. Bruix, M. Bianchi, J. A. Miwa, B. Hammer, A. A. Khajetoorians, and P. Hofmann. Crystalline and electronic structure of single-layer TaS_2. *Phys. Rev. B*, 94(8):081404, 2016.

[127] A. Schlicht, M. Schwenker, W. Biberacher, and A. Lerf. Superconducting Transition Temperature of 2H-TaS_2 Intercalation Compounds Determined by the Phonon Spectrum. *J. Phys. Chem. B*, 105(21):4867–4871, May 2001.

[128] K. L. Seyler, P. Rivera, H. Yu, N. P. Wilson, E. L. Ray, D. G. Mandrus, J. Yan, W. Yao, and X. Xu. Signatures of moiré-trapped valley excitons in $MoSe_2/WSe_2$ heterobilayers. *Nature*, 567(7746):66, 2019.

[129] H. Shimotani, G. Diguet, and Y. Iwasa. Direct comparison of field-effect and electrochemical doping in regioregular poly (3-hexylthiophene). *Appl. Phys. Lett.*, 86(2):022104, 2005.

[130] Y. Shkolnikov, E. De Poortere, E. Tutuc, and M. Shayegan. Valley splitting of AlAs two-dimensional electrons in a perpendicular magnetic field. *Phys. Rev. Lett.*, 89(22):226805, 2002.

[131] K. Simonyan and A. Zisserman. Very deep convolutional networks for large-scale image recognition. *arXiv preprint arXiv:1409.1556*, 2014.

[132] S. Sinn, C. H. Kim, B. H. Kim, K. D. Lee, C. J. Won, J. S. Oh, M. Han, Y. J. Chang, N. Hur, H. Sato, et al. Electronic structure of the Kitaev material α-$RuCl_3$ probed by photoemission and inverse photoemission spectroscopies. *Sci. Rep.*, 6:39544, 2016.

[133] T. Song, X. Cai, M. W.-Y. Tu, X. Zhang, B. Huang, N. P. Wilson, K. L. Seyler, L. Zhu, T. Taniguchi, K. Watanabe, et al. Giant tunneling magnetoresistance in spin-filter van der Waals heterostructures. *Science*, page eaar4851, 2018.

[134] T. Taychatanapat, K. Watanabe, T. Taniguchi, and P. Jarillo-Herrero. Electrically tunable transverse magnetic focusing in graphene. *Nat. Phys.*, 9(4):225–229, 2013.

[135] E. J. Telford, A. Benyamini, D. Rhodes, D. Wang, Y. Jung, A. Zangiabadi, K. Watanabe, T. Taniguchi, S. Jia, K. Barmak, et al. Via method for lithography free contact and preservation of 2D materials. *Nano Lett.*, 18(2):1416–1420, 2018.

[136] A. Thompson, F. Gamble, and R. Koehler Jr. Effects of intercalation on electron transport in tantalum disulfide. *Phys. Rev. B*, 5(8):2811, 1972.

[137] M. Tinkham. *Introduction to superconductivity.* Dover, New York, 2004.

[138] A. Togo and I. Tanaka. First principles phonon calculations in materials science. *Scripta Materialia*, 108:1 – 5, 2015.

[139] K. Tran, G. Moody, F. Wu, X. Lu, J. Choi, K. Kim, A. Rai, D. A. Sanchez, J. Quan, A. Singh, et al. Evidence for moiré excitons in van der Waals heterostructures. *Nature*, page 1, 2019.

[140] A. W. Tsen, B. Hunt, Y. D. Kim, Z. J. Yuan, S. Jia, R. J. Cava, J. Hone, P. Kim, C. R. Dean, and A. N. Pasupathy. Nature of the quantum metal in a two-dimensional crystalline superconductor. *Nat. Phys.*, 12(3):208–212, Dec. 2016.

[141] K. Ueno, S. Nakamura, H. Shimotani, A. Ohtomo, N. Kimura, T. Nojima, H. Aoki, Y. Iwasa, and M. Kawasaki. Electric-field-induced superconductivity in an insulator. *Nat. Mater.*, 7(11):855–858, 2008.

[142] M. M. Ugeda, A. J. Bradley, Y. Zhang, S. Onishi, Y. Chen, W. Ruan, C. Ojeda-Aristizabal, H. Ryu, M. T. Edmonds, H.-Z. Tsai, et al. Characterization of collective ground states in single-layer $NbSe_2$. *Nat. Phys.*, 12(1):92–97, 2016.

[143] N. Volkenshtein, V. Dyakina, and V. Startsev. Scattering mechanisms of conduction electrons in transition metals at low temperatures. *Physica Status Solidi (b)*, 57(1):9–42, 1973.

[144] K. E. Wagner, E. Morosan, Y. S. Hor, J. Tao, Y. Zhu, T. Sanders, T. M. McQueen, H. W. Zandbergen, A. J. Williams, D. V. West, and R. J. Cava. Tuning the charge density wave and superconductivity in Cu_xTaS_2. *Phys. Rev. B*, 78(1):104520, Sept. 2008.

[145] H. Wang, L. Yu, Y.-H. Lee, W. Fang, A. Hsu, P. Herring, M. Chin, M. Dubey, L.-J. Li, J. Kong, et al. Large-scale 2D electronics based on single-layer MoS_2 grown by chemical vapor deposition. In *Electron Devices Meeting (IEDM), 2012 IEEE International*, pages 4–6. IEEE, 2012.

[146] H. Wang, L. Yu, Y.-H. Lee, Y. Shi, A. Hsu, M. L. Chin, L.-J. Li, M. Dubey, J. Kong, and T. Palacios. Integrated Circuits Based on Bilayer MoS_2 Transistors. *Nano Lett.*, 12(9):4674–4680, Sep 2012.

[147] J. I.-J. Wang, Y. Yang, Y.-A. Chen, K. Watanabe, T. Taniguchi, H. O. Churchill, and P. Jarillo-Herrero. Electronic transport of encapsulated graphene and WSe_2 devices fabricated by pick-up of prepatterned hbn. *Nano Lett.*, 15(3):1898–1903, 2015.

[148] L. Wang, I. Meric, P. Huang, Q. Gao, Y. Gao, H. Tran, T. Taniguchi, K. Watanabe, L. Campos, D. Muller, et al. One-dimensional electrical contact to a two-dimensional material. *Science*, 342(6158):614–617, 2013.

[149] Q. H. Wang, K. Kalantar-Zadeh, A. Kis, and J. N. Coleman. Electronics and optoelectronics of two-dimensional transition metal dichalcogenides. *Nat. Nano.*, 7:699, 2012.

[150] Y. Wang and A. V. Chubukov. Enhancement of superconductivity at the onset of charge-density-wave order in a metal. *Phys. Rev. B*, 92(12):125108, 2015.

[151] Z. Wang, J. Shan, and K. F. Mak. Valley-and spin-polarized landau levels in monolayer WSe_2. *Nat. Nano.*, 12(2):144, 2017.

[152] J. Wilson and A. Yoffe. The transition metal dichalcogenides discussion and interpretation of the observed optical, electrical and structural properties. *Adv. in Phys.*, 18(73):193–335, 1969.

[153] J. A. Wilson, F. Di Salvo, and S. Mahajan. Charge-density waves and superlattices in the metallic layered transition metal dichalcogenides. *Adv. in Phys.*, 24(2):117–201, 1975.

[154] S. Wu, J. S. Ross, G.-B. Liu, G. Aivazian, A. Jones, Z. Fei, W. Zhu, D. Xiao, W. Yao, D. Cobden, et al. Electrical tuning of valley magnetic moment through symmetry control in bilayer MoS_2. *Nat. Phys.*, 9(3):149, 2013.

[155] Z. Wu, S. Xu, H. Lu, A. Khamoshi, G.-B. Liu, T. Han, Y. Wu, J. Lin, G. Long, Y. He, et al. Even-odd layer-dependent magnetotransport of high-mobility Q-valley electrons in transition metal disulfides. *Nat. Commun.*, 7:12955, 2016.

[156] X. Xi, Z. Wang, W. Zhao, J.-H. Park, K. T. Law, H. Berger, L. Forró, J. Shan, and K. F. Mak. Ising pairing in superconducting $NbSe_2$ atomic layers. *Nat. Phys.*, 12(2):139–143, 2016.

[157] X. Xi, L. Zhao, Z. Wang, H. Berger, L. Forró, J. Shan, and K. F. Mak. Strongly enhanced charge-density-wave order in monolayer $NbSe_2$. *Nat. Nano.*, 10(9):765–769, 2015.

[158] D. Xiao, G.-B. Liu, W. Feng, X. Xu, and W. Yao. Coupled spin and valley physics in monolayers of MoS_2 and other group-vi dichalcogenides. *Phys. Rev. Lett.*, 108(19):196802, 2012.

[159] H. Xiong, J. Sobota, S.-L. Yang, H. Soifer, A. Gauthier, M.-H. Lu, Y.-Y. Lv, S.-H. Yao, D. Lu, M. Hashimoto, et al. Three-dimensional nature of the band structure of $ZrTe_5$ measured by high-momentum-resolution photoemission spectroscopy. *Phys. Rev. B*, 95(19):195119, 2017.

[160] J.-P. Xu, M.-X. Wang, Z. L. Liu, J.-F. Ge, X. Yang, C. Liu, Z. A. Xu, D. Guan, C. L. Gao, D. Qian, et al. Experimental detection of a Majorana mode in the core of a magnetic vortex inside a topological insulator-superconductor $Bi_2Te_3/NbSe_2$ heterostructure. *Phys. Rev. Lett.*, 114(1):017001, 2015.

[161] N. Yabuki, R. Moriya, M. Arai, Y. Sata, S. Morikawa, S. Masubuchi, and T. Machida. Supercurrent in van der Waals Josephson junction. *Nat. Commun.*, 7:10616, 2016.

[162] Y. Yang, S. Fang, V. Fatemi, J. Ruhman, E. Navarro-Moratalla, K. Watanabe, T. Taniguchi, E. Kaxiras, and P. Jarillo-Herrero. Enhanced superconductivity upon weakening of charge density wave transport in 2H-TaS_2 in the two-dimensional limit. *Phys. Rev. B*, 98(3):035203, 2018.

[163] M. Yankowitz, J. Xue, D. Cormode, J. D. Sanchez-Yamagishi, K. Watanabe, T. Taniguchi, P. Jarillo-Herrero, P. Jacquod, and B. J. LeRoy. Emergence of superlattice Dirac points in graphene on hexagonal boron nitride. *Nat. Phys.*, 8(5):382, 2012.

[164] J. Ye, Y. Zhang, R. Akashi, M. Bahramy, R. Arita, and Y. Iwasa. Superconducting dome in a gate-tuned band insulator. *Science*, 338(6111):1193–1196, 2012.

[165] J. T. Ye, S. Inoue, K. Kobayashi, Y. Kasahara, H. T. Yuan, H. Shimotani, and Y. Iwasa. Liquid-gated interface superconductivity on an atomically flat film. *Nat. Mater.*, 9(2):125–128, 2010.

[166] M. Yoshida, R. Suzuki, Y. Zhang, M. Nakano, and Y. Iwasa. Memristive phase switching in two-dimensional 1T-TaS_2 crystals. *Sci. Adv.*, 1(9):e1500606, 2015.

[167] A. F. Young and P. Kim. Quantum interference and Klein tunnelling in graphene heterojunctions. *Nat. Phys.*, 5(3):222–226, 2009.

[168] A. F. Young, J. D. Sanchez-Yamagishi, B. Hunt, S. H. Choi, K. Watanabe, T. Taniguchi, R. C. Ashoori, and P. Jarillo-Herrero. Tunable symmetry breaking and helical edge transport in a graphene quantum spin Hall state. *Nature*, 505(7484):528–532, 2013.

[169] G. Yu, R. Gorbachev, J. Tu, A. Kretinin, Y. Cao, R. Jalil, F. Withers, L. Ponomarenko, B. Piot, M. Potemski, et al. Hierarchy of Hofstadter states and replica quantum Hall ferromagnetism in graphene superlattices. *Nat. Phys.*, 10(7):525, 2014.

[170] H. Yuan, H. Shimotani, A. Tsukazaki, A. Ohtomo, M. Kawasaki, and Y. Iwasa. Hydrogenation-induced surface polarity recognition and proton memory behavior at protic-ionic-liquid/oxide electric-double-layer interfaces. *J. Am. Chem. Soc.*, 132(19):6672–6678, 2010.

[171] H. Zeng, J. Dai, W. Yao, D. Xiao, and X. Cui. Valley polarization in MoS_2 monolayers by optical pumping. *Nat. Nano.*, 7(8):490, 2012.

[172] K. Zhang, F. L. Yap, K. Li, C. T. Ng, L. J. Li, and K. P. Loh. Large scale graphene/hexagonal boron nitride heterostructure for tunable plasmonics. *Adv. Funct. Mater.*, 24(6):731–738, 2014.

[173] Y. Zhang, Y.-W. Tan, H. L. Stormer, and P. Kim. Experimental observation of the quantum hall effect and Berry's phase in graphene. *Nature*, 438(7065):201–204, 2005.

[174] W. Zhao, Z. Ghorannevis, L. Chu, M. Toh, C. Kloc, P.-H. Tan, and G. Eda. Evolution of electronic structure in atomically thin sheets of WS_2 and WSe_2. *ACS Nano*, 7(1):791–797, 2012.

[175] J. Zhou, L. Shen, M. D. Costa, K. A. Persson, S. P. Ong, P. Huck, Y. Lu, X. Ma, and Y. P. Feng. 2dmatpedia: An open computational database of two-dimensional materials from top-down and bottom-up approaches. *arXiv preprint arXiv:1901.09487*, 2019.

[176] J. M. Ziman. *Electrons and phonons: the theory of transport phenomena in solids.* Oxford university press, 1960.